University of Wollongong

Research Online

2022

Electric and Magnetic Manipulation of Liquid Metals

Yahua He

Electric and Magnetic Manipulation of Liquid Metals

Yahua He

This thesis is presented as part of the requirement for the conferral of the degree:

Doctor of Philosophy

Supervisors: Distinguished Professor Xiaolin Wang

Co-Supervisors: Professor Shujun Zhang and Zhenxiang Cheng

University of Wollongong

School of Engineering and Information Science

May 2022

Abstract

Over the past decade, gallium-based liquid metals have attracted enormous attention, emerging as a new cutting-edge multi-functional material for reconfigurable electronics, soft robotics, microfluidics, and biomedical applications, based on utilizing the intrinsic advantages of liquid metal. These unique advantages that combine high electrical conductivity, thermal conductivity, biocompatibility, low mechanical compliance, and viscosity all-in-one make the liquid metal applicable for a tremendous number of applications. Moreover, the self-passivating oxide skin of the liquid metal in an ambient environment forms a unique core (oxide skin)-shell (liquid metal) structure and provides a new strategy for two-dimensional thin films with a thickness of a few nanometers. The reports on the liquid metal can be mainly divided into three categories: 1) liquid-metal-based composite structures; 2) the core-shell strategy for thin films; and 3) electrochemical manipulation of the liquid metal in electrolyte.

The liquid metal (LM) composites represent material systems in which LM alloys are either suspended as small droplets within a soft polymer matrix or mixed with metallic nanoparticles to form a biphasic composition, through which the electrical, dielectric, and thermal properties of composites can be controlled, thus enabling their applications in soft-matter sensing, actuation, and energy harvesting. Moreover, the fluidity and conductivity of the liquid metal make it suitable to be directly patterned (i.e., liquid metal ink) on various soft substrates (e.g., polydimethylsiloxane (PDMS) for ultra-stretchable electronics. Compared to the traditional electronics, which are typically composed of intrinsically rigid materials that have limited deformability, the liquid metal based soft electronics are highly flexible, stretchable, and conformable. Most importantly, they are capable of electrical self-healing, enabling their electrical functionality, even under severe damage. These properties and applications of liquid metal composites show great

potential for practical usage.

The core-shell strategy is the concept of using a liquid metal as a reaction environment for atomically thin metal oxides. Co-alloying suitable reactive metals can form co-alloyed metal oxides at the metal-air interface. In addition to various metal oxides achieved through the co-alloying process, another class of functional metallic compounds, such as the Group IV monochalcogenides (MX, M = Sn, Ge, Pb, etc. and X = S, Se), can be also synthesized on the surface of the liquid metal in designed atmospheres (e.g., H_2S). This strategy is also used for metal oxides of those metals with high melting points (e.g., Hf: 2500 ^oC and Gd: 1585 ^oC) by alloying them (~1 wt%) into Galinstan with the help of grinding amalgamation. Moreover, the post-processing for the exfoliated oxide thin film can further expand the application of this strategy, such as the thin film of $GaPO_4$ obtained with a following vapor phase reaction (300 – 350 ^oC, Ga_2O_3 film with H_3PO_4 in N_2 atmosphere). This strategy is novel and provides a programmable path to expand the synthesis of two-dimensional thin film.

The electrochemical manipulation of the liquid metal is based on the manipulation of the surface tension of the liquid metal, thus realizing the controllable motion/deformation of the liquid metal. That is, the pure liquid metal has high surface tension (~ 550 mN/m), while the oxide layer on the surface will significant lower the surface tension and limit the fluidity of the liquid metal. Meanwhile, the oxide layer (e.g., Ga_2O_3) can be removed with acid/base (HCl/NaOH) solutions, regaining the high surface tension and water-like fluidity of the liquid metal. The dissolution of the oxide layer will fill the surface of the LM with negative charges, while the outer layer is positively charged, forming an electrical double layer. The manipulation involves the concept of simultaneous formation and dissolution of the oxide layer by applying an electric field on liquid metal in NaOH/HCl solution, which leads to the directional motion and deformation of liquid

metal. By placing the liquid metal between the electrodes (without contact), the electric field will change the charge distribution, thereby leading to an imbalance of the surface tension, which finally pushes the liquid metal to move. When the anode is inserted into the liquid metal, an oxide layer is expected to form on the surface. A critical voltage (~0.8 V) is required for the formation of oxide layer, below which, the liquid metal adopts its equilibrium shape and forms an electric double layer. Once the oxide layer is formed, the surface tension of the droplet decreases significantly, leading to the deformation and spreading of the liquid metal. Through this, controllable motion is realized, and new phenomena are observed.

Most reports have been focused on the potential applications of the liquid metal, while fundamental research on the liquid metal, such as its new rheological properties, the underlying mechanism of the deformation (i.e., surface tension and oxidation), and other types of exploration for new manipulation capabilities (e.g., electromagnetic interaction), has long been underestimated.

Here, in this thesis, I found some new rheological properties and explored the non-contact electromagnetic manipulation of liquid metal. Moreover, I have tried to reveal the underlying mechanism behind the deformation of the liquid metal by taking the electric current generated through the liquid metal as a clue. A screening effect that prevented the further oxidation of liquid metals has been demonstrated. The screening effect is induced when a liquid metal droplet deforms and surrounds the cathode, yielding a huge inner electric field within the electrical-double-layer to counter the external electric field. An analogous contact inhibition behavior of multi-droplets triggered by the screening effect was observed. The droplets are arranged to arrive at the cathode at the same time (e.g., tilted substrate), and they come into contact each other without merging and stop their deformation. Once they are separated by moving the cathode, the deformation process is

restarted. Moreover, a controllable heartbeat effect of liquid metal was realized. In this work, the experimental setup was modified for easier implementation compared to previous report. The heartbeat effect of liquid metal droplets in different sizes, stimulated by a small voltage of 1.5 V with various electrode positions, has been demonstrated. A beating factor *k*, the ratio of height to the diameter of droplets, was defined to characterize the periodic process within the balance of gravity with interfacial tension. This work optimizes the heartbeat effect of liquid metal and provides a fundamental insight into the beating process, as well as enabling potential fluidic and bionic applications, such as liquid actuators/pumps and soft robots. I also discovered that the liquid metal streams could be formed with the help of electrochemical oxidation by overcoming the Rayleigh–Plateau instability. Moreover, a non-contact method of manipulation of free-falling cylindrical streams of liquid metals into unique shapes, such as levitated loops and squares, was explored. Such cylindrical streams can be made to form in aqueous media by electrochemically lowering the interfacial tension. The electrochemical reactions require an electrical current that flows through the streams, making them susceptible to Lorentz forces. Consequently, varying the position and shape of a magnetic field relative to the stream controls these forces. Moreover, the movement of the metal stream relative to the magnetic field induces significant forces arising from Lenz's law that cause the manipulated streams to levitate in unique shapes. The ability to control streams of liquid metals in a non-contact manner will enable new strategies for shaping electronically conductive fluids for advanced manufacturing and dynamic electronic structures.

Acknowledgments

I would like to express my thanks to my dear supervisor, Professor Xiaolin Wang, for his continues guidance, encouragement and financial support during my PHD period. Prof. Wang spent quite time helping me building innovative ways of thinking and offering me novel ideas.

I would also like to express my thanks to my co-supervisors, Prof Shujun Zhang and Zhengxiang Chen, for their help. And I would also thank Dr Khay See for his help in building the Labview platform and sharing the digital multimeters.

I would like to express my thanks to Dr Tania Silver for her help in editing papers for me.

I would also like to thank my collaborators and friends, Dr Zhenwei Yu, Dr Frank Fei Yun, Dr Zhi Li, Dr Zengji Yue, Dr David Cortie, Dr Jixing Liu, Weiyao Zhao, Lei Chen.

I would also like to express my thanks to the staff and administrators at the University of Wollongong, Australian Institute of Innovative Materials (AIIM), the Institute for Superconducting and Electronic Materials (ISEM): Prof Will Price, Prof Shixue Dou, Germanas Peleckis, Crystal Mahfouz, Naomi Davis, and Narelle Badger.

Finally, I would thank my parents and my partner Jing You for their continues support and encouragement.

Certification

I, Yahua He, declare that this thesis submitted in fulfilment of the requirements for the conferral of the degree Doctor of Philosophy, from the University of Wollongong, is wholly my own work unless otherwise referenced or acknowledged. This document has not been submitted for qualifications at any other academic institution.

_____

Yahua He

May 25, 2022

List of Names or Abbreviations

- **List of Abbreviations**

Abbreviation	Full name
LMs	Liquid metals
RTLMs	Room-temperature liquid metals
LMD	Liquid metal droplet
MP	Melting point
EGaIn	Eutectic gallium indium
Galinstan	Gallium indium tin alloy
PDMS	Polydimethylsiloxane
PMMA	Poly (methyl methacrylate)
PBMA	Poly (n-butyl methacrylate)
PVA	Polyvinyl alcohol
PEG	Polyethylene glycol
EDL	Electric double layer
2-D	2-dimensional
3-D	3-dimensional
LM-UF	LM-urea-formaldehyde
SEM	Scanning electron microscope
NdFeB	Neodymium–iron–boron
RMF	Rotating magnetic field
D	Distance
P_g	Gravitational pressure
P_L	Laplace pressure

P_E	Electrostatic pressure
P_L	Lorentz force induced pressure
CL	Compact layer
OL	Oxide layer
DL	Diffuse layer
R_O	Oxidation rate
R_D	Dissolution rate
P_A	Position of anode
LMW	Liquid metal wire
P_M	Position of magnet
VR	Volumetric flow rate
N pole	North pole
S pole	South pole
DMM	Digital multimeter

- **List of Symbols**

Symbol	Name	Unit
γ	Surface tention	mN/m
ρ	Density	10^3 kg m^{-3}
V	Voltage	V
P	Pressure	Pa
R	Radius	cm
F	Force	N
θ	Contact angle	°/degree

i/I	Electric current	Ampere
C	Capacitance	Farad
ε	Permittivity	Farad/m
m	Mass	kg
M	Molar mass	g/mol
z	Valence of ions	NA
n	Moles of ions	mol
A	Area size	m^2
c	Concentration	mol/m^3
T	Absolute temperature	K
φ	Potential	V
E	Electric field	V/m
f	Frequency	Hz
h	Height	m
k	Ratio of height and diameter	NA
B	Magnetic field intensity	T
L	length	m
a	Acceleration	m/s^2
v	Velocity	m/s
J	Current density	A/m^2
σ	Electrical conductivity	S/m

Table of Contents

List of Tables, Figures and Illustrations

- **List of Figures**

wave evolution of an LM bath. (c) Schematic view and snapshots of the directional orbital-chasing motion of the LM heterodimers and the definition of the regime parameters. (d) The LM morphologies observed as a function of potential, a highly stable LM stream formed in suitable potential and velocity ranges. (e) Optical microscope images of simultaneously solidified liquid metal streams.

Figure 2.3. Simple and popular ways to pattern LM. (a) Filling the LM within a silicone mold. (b) Patterning LM on a receiving substrate across a stencil. (c) Injecting LM into microchannels for high-resolution structures. (d) Inkjet printing of small colloidal suspensions of LM droplets. (e) surface-oxide-layer-assisted 3D printed structures of LM. (f) 2D direct writing of LM. (g) Laser-ablation-assisted pattern films of LM in elastomer.

Figure 2.4. (a) Fabrication process of a reversibly deformable dipole antenna that can be stretched and rolled, with the antenna self-healings in response to sharp cuts, such as those inflicted by a razor blade. (b) Non-contact magnetic self-healing method based on Fe-doped LM. (c) Electric field assisted self-healing. (d) Soft-matter composite for mechanically robust, electrically self-healing circuit interconnects, with photographs in the insets.

Figure 2.5. Various methods for controllable LM-polymer composites. (a) Schematic illustration of the preparation route for LM droplets produced via ultrasound. (b) Schematic illustration of the mechanism for producing LM nanoparticles by liquid-based nebulization. (c) (i) Two-step12-(2-bromoisobutyramido) dodecanoic acid (BiBADA) functionalized and surface-initiated ATRP of nanoparticles. (ii) Stepwise functionalization of LM or surface-initiated ATRP from *in*-situ functionalized LM

droplets. (d) Schematic illustration of the synthesis of "litchi"- and "passion fruit"-like EGaIn@ZIF-8 NPs, where ZIF-8 is zeolitic imidazolate framework-8 and NP stands for nanoparticle. Pre-synthesized EGaIn@PVP nanodroplets, where PVP is polyvinylpyrrolidone, are mixed with 2-methylimidazole (2-MI) and Zn^{2+} at different L/M ratios (2 and 1).

Figure 2.6. LM-based composites with non-metallic particles. (a) Schematic illustration of rolling a liquid metal droplet on a powder bed. (b) Schematic illustration of submerging a liquid metal droplet in a powder colloidal suspension. (c-h) SEM images of different powders that were coated on the surface of Galinstan by rolling on a powder bed: c) ZnO nanoparticles, d) In_2O_3 nanoparticles, e) Al_2O_3 powder, f) Teflon powder, g) TiO_2 nanoparticles, and h) single wall carbon nanotubes. (i) Schematic illustration of the experimental setup showing the forces influencing the motion of a Galinstan droplet with or without a nanoparticle coating.

Figure 2.7. Synthesis strategies, manipulated properties and motions of LM-metallic composites. (a) Appearances of gallium and Ni particles before and after stirring. (b) Schematic illustration of LM-X fabrication, where X stands for various metal particles. The metals are shear mixed with LM in a mortar and pestle, and the images show the paste-like morphology of LM-W and LM-Ag in the mortar. (c) A macro-sized Ga-alloy droplet is ultrasonically dispersed in an aqueous solution to form sub-micrometer LM droplets. (d) Methods to realize LM-Phagocytosis in different solutions. (e) Improved thermal conductivity when the LM is doped with different particles. (f) Self-fueled liquid metal motor running in a circular petri dish with schematic illustration of the forces affecting the velocity of the motor, and average velocity and displacement plots as

functions of time.

Figure 2.8. Strategy for the formation of LM based 2D materials, including the co-alloying and surface reactions of LM with other elements.

Figure 2.9. One-step synthetic strategy for metal compounds based on the core-shell structure of the LM. (a) Fundamental principles, synthetic approach based on the core-shell strategy, and deposition of film with nano-size thickness of HfO_2. (b) Schematic illustration and characterization of the 2D SnO/In_2O_3 heterostructure. (c) Schematic illustration of the synthetic approach to complex core-shell structures by the localized galvanic replacement reaction. (d) the synthetic approach for monolayer SnS. (e) High performance piezoelectric nanogenerators and broadband photodetectors fabricated based on the monolayer SnS.

Figure 2.10. Multi-step strategy for the formation of metal compound. (a) three-step formation of large-area two-dimensional semiconducting GaS. (b) two-step formation of $GaPO_4$. (c) Two-step process for centimeter scale oxide layer fabricated by utilizing squeeze-printing. (d) Water- and water-vapor-assisted formation of 2D sheets or 1D fibers of Al/Ga LM alloy.

Figure 2.11. The core-shell structure enables unique phenomena and properties of the LM. (a, b) The anisotropic surface phenomenon of LM alloy. (c) Unique surface patterns during solidification of EBiGa-based LM alloy. (d) LM electrocatalyst at the liquid metal/electrolyte interface, converting CO_2 to carbonaceous and graphitic products at room temperature.

Figure 2.12. (a) Magnetocaloric ferrofluid formed by suspending gadolinium nanoparticles in the LM. (b) Controllable locomotion of LM in complex microfluidic channels showing the ability to work as electrical switches. (c) Controllable motion of LM mobiles on a solid surface.

Figure 2.13. (a) Controllable direct patterning of LM on various substrates using magnetic field. (b) Enhanced mechanical properties, viscosity, and stiffness of the LM-based magnetoactive slurries. (c) Ferromagnetic LM material with transformable shape and reconfigurable polarity, which can used as flexible erasable magnetic recording paper. (d) Magnetic healing method based on Fe-doped LM conductive ink for flexible electronics.

Figure 2.14. Surface charges and induced motion under external electric field. (a) In a base solution. (b) In an acid solution. (c) The principle of motion. (d) A liquid metal enabled pump for driving a range of liquids. (e) Graphite induced surface charge alteration and a cathode-oriented motion in NaOH solution. (f) The bipolarization induced cathode-oriented motion in NaOH solution for a closed system. (g) A wheeled robot driven by a LM droplet.

Figure 2.15. Surface charges and induced motion via the surface electrochemical reaction. (a) LM-Al composite structure for altering the surface charge distribution. (b-e) Asymmetric surface wetting effect for motion control: (b) LM-Ag film, (c) Induced net force, (d) LM/Al-copper wire, (e) LM-porous copper.

Figure 2.16. Surface oxidation induced novel phenomena and applications of the LM. (a) Deformation of LM induced by surface oxide layer. (b) The LM deforms and moves to cathode in a confined channel. (c) Simultaneous deformation and solidification of the LM. (d) 'Recapillarity' effect of the LM under a reductive voltage. (e) Non-contact, maskless lithography method for the LM. (f) Voltage-stimulated heartbeat effect of the LMD.

Figure 2.17. (a) The electrical current of the LM droplet relative to the electric potential and concentration of the NaOH solution. (b) The current changes during the morphological transitions of the LM under different electric potentials. (c) Electrochemically manipulated gradients in interfacial tension to separate the LM droplets.

Figure 2.18. External electrical-current-assisted electromagnetic manipulation of LM. (a) Electromagnetic levitation of LM. (b) Jumping behavior of LM.

Figure 2.19. Rotating-magnetic-field assisted electromagnetic manipulation of LM. (a) Controllable locomotion of LM. (b) Non-coalescent phenomenon of LM droplet sustained on LM bath surface.

Figure 2.20. Electrochemical-reaction-assisted simultaneous deformation and electromagnetic manipulation of an LM. (a) Magnetic field boundary of an aluminum powered LM motor. (b) Rotation of the LM along the concentric ring channel with controllable speed and (c) with changing patterns.

Figure 3.1. The OCA-15EC contact angle instrument from DataPhysics, Germany. The

liquid metal is pumped from the needle, and the motion on the substrate on the stage is recorded by the CCD camera system.

Figure 3.2. Electrical measurement system includes two parts: (a) digital multimeter and (b) the Labview platform.

Figure 3.3. Me3D (Australia) 3D printer consists of a 3-axial stage and motor. The raw materials are driven by the motor which is controlled by a specially designed program on the computer.

Figure 4.1. Liquid metal morphologies under different electric potential, (a) Droplets, 0 V and (b) Wire, 1.5 V. (c) Current-carrying liquid metal wire rotated by the Lorentz force within a magnetic field. (d) Schematic illustration of experimental setup, a blue piece of paper covered one wall of the vessel to facilitate imaging. (e) Original images showing the LMW path resulting from different positions of the magnet with N pole outwards. The dotted lines indicate the location and the shape of the magnet. (f) False colored images of LM (white) showing four sequences of frames with a force diagram and motion analysis.

Figure 4.2. The magnetic field distribution and the corresponding Lorentz force on the LMW at $P_M = 0$ cm.

Figure 4.3. The time evolution of the trajectory of the LMW at $P_M = -3$ cm (a), the magnetic field distribution and the corresponding Lorentz force of the LMW at 0 s (b) and at 0.288 s (c).

Figure 4.4. Liquid Dynamics under Various Magnetic Fields and VRs. Sequence of photographs recording the motion of a liquid metal wire under different experimental conditions with the magnet center fixed at 0 cm, N pole outwards. (**a**) 2 μl/s, 0.1 T; (**b**) 4 μl/s, 0.1 T; (**c**) 2 μl/s, 0.2 T; (**d**) 4 μl/s, 0.2 T. The square-shaped magnet is with dimensions of $5 \times 5 \times 0.5$ cm^3. (**e**) The changes of average velocity and diameter of LMW. The fourth stage is excluded from (e) as LM wire fully stops at the edge of magnet.

Figure 4.5. Statistical Results for Elapsed Time and the Size of Path. (a) Elapsed time with circle angles. (b) the size of the path of LMW under different conditions, including height (H_{max}) and width (W_{max}). L_M stands for the length of the magnet (fixed at 5 cm).

Figure 4.6. the velocity change of the LMW during the acceleration outwards process. v_1 is the velocity of LM flowing along the LMW, v_2 is the Lorentz force accelerated radially velocity, v is the true velocity of the LMW (resultant velocity of v_1 and v_2)

Figure 4.7. Role of Velocity on LMW Trajectory. (a) The velocity of LM pumped from the needle at 2 μl/s without a magnet, with the inset showing snapshots of the trajectories. The green dotted line represents the needle outlet, above the green line is the needle, while under the green line is the LMW. (b-e) and the typical trajectories under 0.1 T magnetic field at different positions with the N pole outwards. The dotted lines indicate the location and the shape of the magnet.

Figure 4.8. The time evolution of the trajectory of the LMW at PM = -4 cm (a), the magnetic field distribution and the corresponding Lorentz force of the LMW at 0 s (b).

Figure 4.9. The magnetic field distribution and the corresponding Lorentz force of the LMW at P_M = -6 cm.

Figure 4.10. The liquid metal traces out the perimeter of the magnets, which are located behind the blue paper. The liquid metal can be configured into different shapes (a-d) and complicated magnetic field arrangements by using two circle magnets with diameters of 3.5 cm, (e-h) N/S poles placed side by side with a distance of 0.5 cm; (i-l) N/S poles arranged vertically with a distance of 0.5 cm. The yellow dotted lines indicate the location and the sahpe of the magnet.

Figure 4.11. Representative images of dynamic patterns of LMW as magnet moved horizontally at P_M = -6 cm with different speed, N pole outwards and 0.1 T. (a) 0.2 cm/s, (b) 1cm/s, (c) 3cm/s. The images on the far right are the superposition of the first four snapshots.

Figure 4.12. (a) The measured electrical current passing through the LMW and its comparison to the cases without the wire and with a copper wire under the same external voltage fixed at 1.5 V. (b) the diagram of electrons flow toward the nozzle. Here, I depict two oxidation reactions occurring at distinct positions, although in reality there are reactions occurring along the entire length. Consequently, the current increases along the length of the metal toward the direction of the nozzle due to the cumulative effect of oxidation along the length of the wire

Figure 4.13. (a) Current versus time of LMWs with different length. (b) Statistical mean value of the current with different lengths measured in R2, which can be linearly fitted by

equation y = 53.4 + 1.933x. The external voltage is fixed at 1.5 V for all cases.

Figure 4.14. Electrical current data of LMWs with magnet placed at different positions, (a-c) P_M = 0 cm, (d-f) P_M = -6 cm, (g-i) P_M = -9 cm. The current value is synchronized with the periodically formation/disintegration of LMW. The inset figures in (a, d, g) are the frequency data through FFT of current. (b, e, h) are the first three cycles, and (c, f, i) show the current drop in the first cycle induced by Lenz's law effect. The external voltage is fixed at 1.5 V for all cases.

Figure 4.15. Current versus time of LMWs when a magnet placed at P_M = 0 cm under different experimental conditions. (**a**) 2 μl/s, 0.1 T; (**b**) 4 μl/s, 0.1 T; (**c**) 2 μl/s, 0.2 T; (**d**) 4 μl/s, 0.2 T.

Figure 4.16. Current versus time of LMWs with a magnet placed at different positions. (a) P_M = -4 cm; (b) P_M = -5 cm; (c) P_M = -6 cm and (d) P_M = -9 cm.

Figure 4.17. Calculated ration of inertial force and Lorentz force (*He*) when (a) magnet is placed at different positions, and (b) LMW is formed under different conditions with magnet placing at P_M = 0 cm.

Figure 5.1. (a) The configuration of one droplet. *D* stands for distance between electrodes. Different deformations triggered by (b) voltages with fixed electric field of 1.5 V/cm, and (c) electric fields with fixed voltage of 5 V. (d) the deformation over time of one liquid metal droplet, under voltage of 5 V and electric field of 1.5 V/cm. (e) Illustrated motion and equivalent circuit of the droplet. (f) Changes of velocity, surface

area size, and (g) electrical current of the droplet over three stages.

Figure 5.2. (a) Surface charge distributions and motion analysis of the liquid metal droplet. (b) Equivalent circuit of the experimental setup: C_A and R_A are the electrical-double-layer capacitance and the charge transfer resistance between the liquid metal and the solution; C_C and R_C are the electrical-double-layer capacitance and charge transfer resistance between the copper electrode and the solution; R_E is the resistance of the electrolyte. The electrical-double-layer is divided into two subregions: the inner compact layer (CL) and the outer diffuse layer (DL). (c) Illustration of the charge distributions, and (d) the potential drop across the liquid metal and the copper electrode.

Figure 5.3. Quantitative characterization of the capacitance and potential drop at the anode. **(a)** oxidation rate and dissolution rate of liquid metal droplet as it moves toward the cathode. **(b)** The corresponding thickness change of the oxide layer, with the inset showings the thickness and corresponding linear fitted curve from 0 to 8.5 s. **(c)** The changes of capacitance and **(d)** potential within the layers in stages 1 and 2.

Figure 5.4. The measured electrical currents under different conditions. (a) fixed external voltage of 5 V. (b) Fixed electric field of 1.5 V/cm.

Figure 5.5. (a) Statistical data and (b) calculated curves for the slopes of the electrical current changes at each stage under different experimental conditions.

Figure 5.6. (a) The configuration of the two droplets. (b) Photographs show the deformation of the two liquid metal droplets. (c) Equivalent circuit of two droplets system

22

for the measurement of electrical current. (d) The electrical current and (e) the changes in surface areas of the two liquid metal droplets.

Figure 5.7. (a) The configuration when the right side of the petri dish is titled. (b) The images show that the two droplets arrive at the static cathode at almost the same time with different deformation behavior. (c) The two droplets are manipulated (contact/separated) by the moving cathode.

Figure 6.1. Working mechanism of the periodic beating effect of liquid metal. (a) Schematic diagram of the experimental setup. (b) Schematic illustration of interfacial-tension-induced beating process. (c) Front and (d) top-view real-time images of THE beating effect of liquid metal.

Figure 6.2. Statistical data for displacement (a) and diameter change (b) of the periodic beating of liquid metal with size of 14 mm at the position of 0 mm, the confinement ring 16 mm in size, inset photographs show the heart-beating phenomenon. The blue and purple dashed lines delineate the specific parts of displacement and diameter waveform shown in **c** and **d**, respectively. (**c, d**) The waveform is well fitted by the sine function with frequency of about 6 Hz.

Figure 6.3. Periodic beating effect for LMDs with different diameters from 8.5 to 14 mm with (a) different displacements and (b) various diameter changes. (c) The displacement and diameter changes, as well as (d) the frequency changes.

Figure 6.4. Periodic beating effect with different anode positions. (a) Schematic diagram

of the anode-position-dependent beating process, with a negative value indicating that the anode moves downward. Corresponding displacement (b) and diameter (c) of LMDs at different position.

Figure 6.5. (a) Displacement and (b) frequency of LMDs of different sizes with different anode positions. Modes I, II, and III stand for different beating shapes of LMDs, which are circular/elliptical, elliptical/triangular, and hybrid shapes, respectively.

Figure 6.6. Height-diameter ratio of a static LMD in the equilibrium state due to the balance between gravitational pressure and Laplace pressure induced by interfacial tension.

Figure 6.7. Statistical value of k for LMDs with different size beating at different anode position (P_A). The blue curve represents the k value change of static state droplets without external voltage, while the new static state is achieved by the balance between gravity and reduced interfacial tension. The heartbeat region between the two static states is divided into three modes based on beating amplitude and frequency.

oxides.

Table 2.4. Melting points of pure metals, and eutectic binary and ternary alloys.

Chapter 1. Introduction

1.1 General Background

Liquid metals (LMs) and alloys are special materials which possess simultaneous fluidic and metallic properties. Compared to conventional rigid metals, LMs are non-crystalline and lack grains, so their atoms are typically arranged in naturally ordered patterns. In recent years, LMs usually refer to those room-temperature LMs (RTLMs) with melting points (MP) around 30 ºC. Up to now, there are five RTLM elements including mercury (Hg), gallium (Ga), rubidium (Rb), cesium (Cs), and francium (Fr),[1] as shown in **Figure 1.1** Mercury is the most well-known LM, which is usually used in thermometers, barometers, and electrodes. Its high toxicity, however, limits the applications of mercury, especially with respect to the health of human body. Meanwhile, rubidium, cesium, and francium (radioactive with very few amounts on earth) are highly active alkali metals. In addition, the alkali metals alloy of eutectic NaK is also liquid at room temperature, it has been used as a strong reductant in synthetic chemistry. However, the alkali metals and alloys may spontaneously ignite in air/water, which limits their practical use. In contrast, the low-toxicity gallium-based LMs and alloys, such as EGaIn (eutectic gallium indium) and Galinstan (gallium indium tin alloy), exhibit better biocompatibility. Recently they have received significant attention due to their promise as soft and stretchable metallic conductors, with low melting points, and simultaneous fluidity and metallic properties at room temperature.[2-11] In the rest of this thesis, the abbreviation 'LM' for liquid metal refers to the gallium-based LM alloys unless otherwise stated.
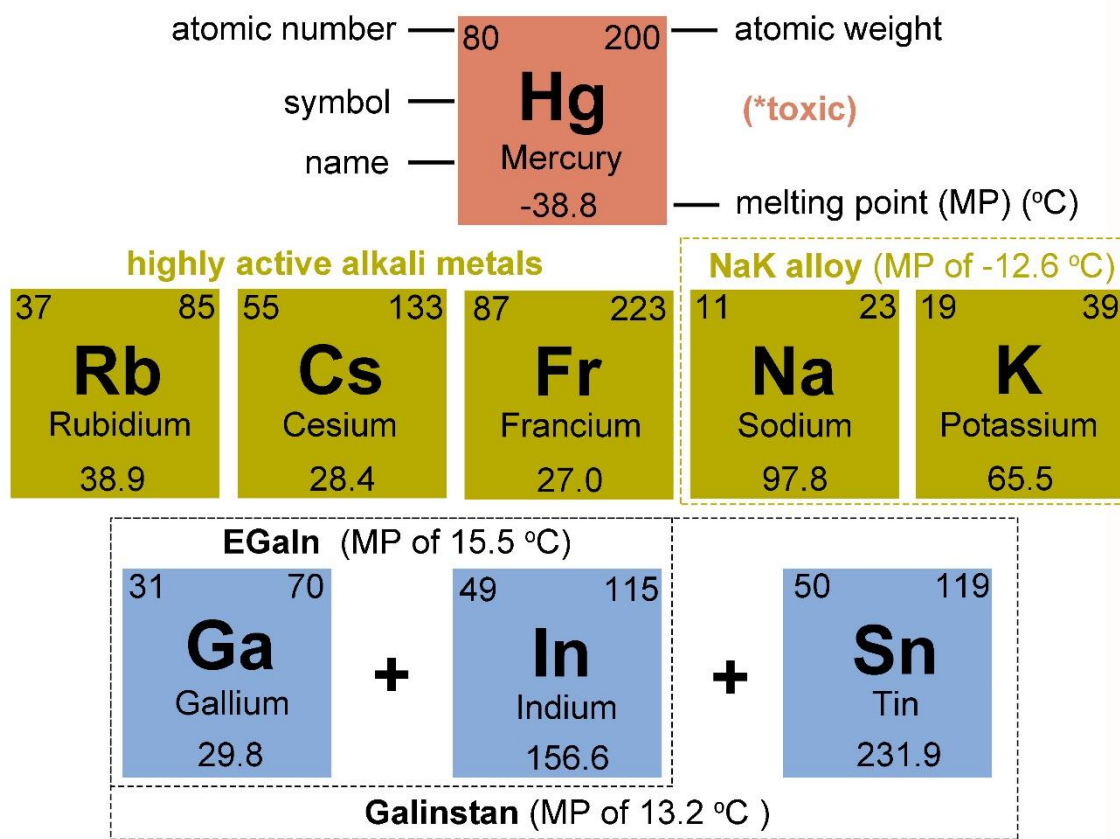
Figure 1.1. Common liquid metals and alloy strategies for gallium based liquid metals.

As illustrated in **Figure 1.2**, these properties make LMs applicable for various types of practical usage. As fluids, the LMs demonstrate unique rheological properties, such as the LM streams formed by overcoming Rayleigh–Plateau instabilities.[11] The water-like fluidity of the LM also enables composite structures with soft organic materials (i.e., PDMS)[12] as well as printable electronics.[13] Moreover, an oxide layer (with thickness of a few nanometers) would be formed on the surface of a liquid metal droplet (LMD) exposed to an oxygen environment, forming a core-shell structure.[14] This unique core-shell structure provides a promising path for various 2-dimensional (2-D) thin films.[15-20] The core-shell structure also makes it possible to form LM/multifunctional particle structures, with these particles either suspended on the surface or within the LM.[21-23] Therefore, magnetic actuation could be realized by the formation of LMD/magnetic particle

27

hybrids.[24] The oxide layer significantly lowers the surface tension of the LMD from 500 mN/m to near zero.[10] Meanwhile, the oxide shell of the LMD is dissolvable in base/acid (i.e., NaOH/HCl) solutions,[8, 10, 25-26] regaining its water-like fluidity and high surface tension. The dissolution of the oxide layer will fill the surface with charges, thereby forming an electric double layer (EDL).[27-29] When an external voltage is present (electrochemical manipulation), the oxide layer reform on the surface with anode inserted into the LMD.[10, 25] That is, there is simultaneous formation and dissolution of the oxide layer on the surface, leading to the deformation and spreading of the LMD. During this process, an electrical current will be generated from the oxidation: $Ga \rightarrow Ga^{3+} + 3e^-$.[11] The value of the current depends on the degree of deformation. Moreover, this current could be used to manipulate the motion of LM stream/LMD with a magnetic field via electromagnetic interaction.[30] This is different from the conventional magnetic actuation for LM/magnetic particle hybrids. This manipulation has been underestimated for a long time without systematic research and exploration.
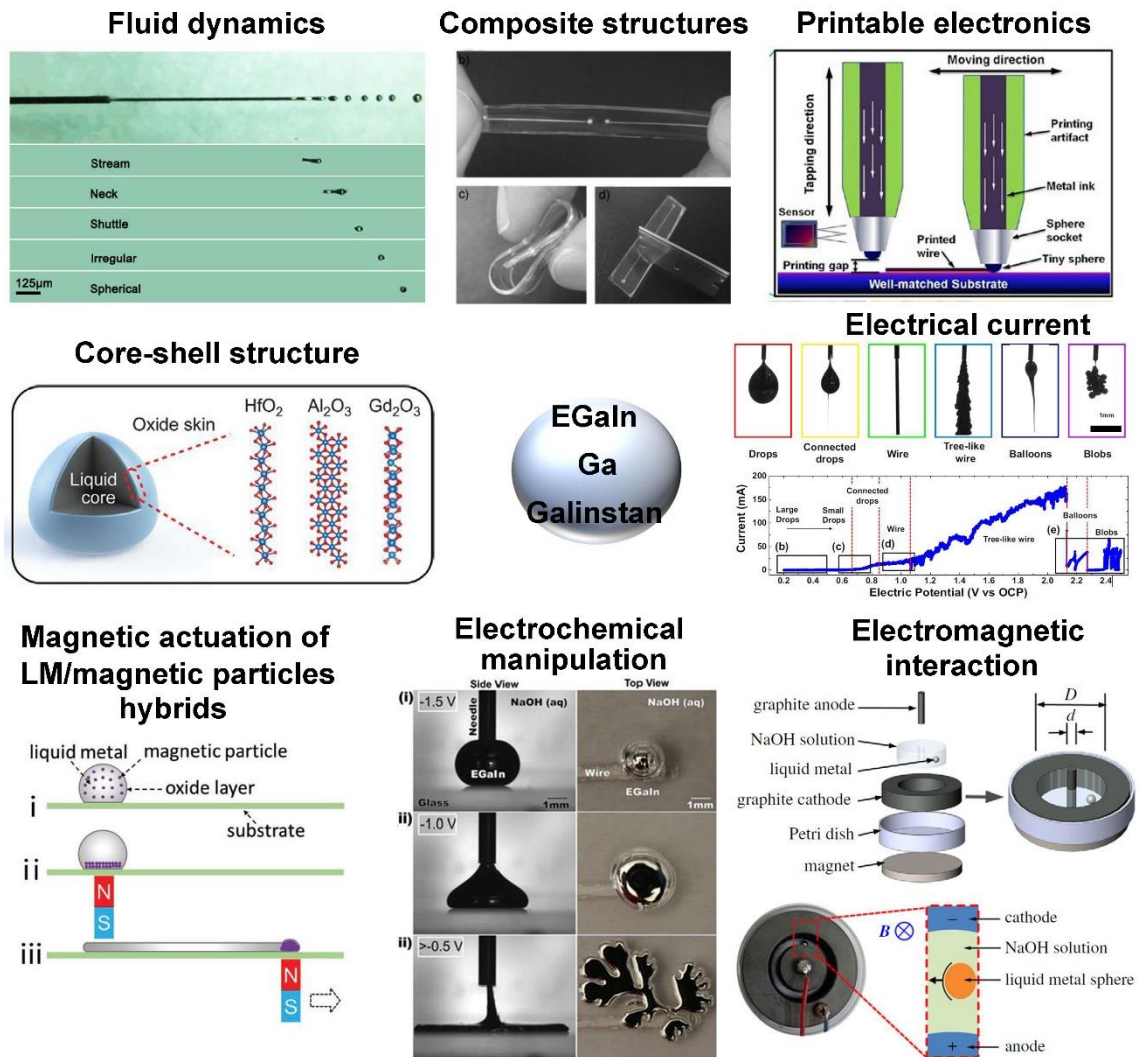
Figure 1.2. Research and potential applications based on different properties of liquid metals.

1.2 Purpose of work

The composite structures and core-shell structures of the LM have been drawn major attention with systematic research on the LMs. The underlying mechanism of electrochemical manipulation, the exploration of electromagnetic manipulation, and together with the rheological properties of the LM, however, has long been ignored. This work aims to take advantage of the electric current, that arises from the electrochemical manipulation, as a clue to explore a quantitative expression for the

relationship between the electric current and surface tension, thereby revealing the underlying mechanism of the electrochemical manipulation. Moreover, this work also tries to develop new strategies for the electromagnetic manipulation of the LM in practical usage (such as for patterning of useful metallic shapes) and explore new rheological phenomena of the LM.

1.3 Thesis Structure

In this thesis, the chapters are arranged in the following manner:

➢ Chapter 1 introduces the general background, major applications of liquid metals, and the research interests in electrical/magnetic manipulation of liquid metals.

➢ Chapter 2 provides a detailed literature review of liquid metals based on their unique properties and various applications, including fluid dynamics, soft electronics, core-shell structures, magnetic actuation, electrochemical manipulation, electrical currents, and electromagnetic interaction.

➢ Chapter 3 presents the experimental details including the experimental setup, instruments, and all kinds of measurement and analysis.

➢ Chapter 4 realizes non-contact manipulation of free-flowing liquid metal wire by the interaction between electrical current and magnetism.

➢ Chapter 5 shows a screening effect of liquid metal during its deformation under external voltage, which is analogous to the 'Faraday cage' effect in liquids.

➢ Chapter 6 demonstrates the optimized controllable heartbeat effect of liquid metal with insight into the underlying mechanism.

➢ Chapter 7 summarizes the main conclusions of all my work and provides a perspective on the potential work and applications of liquid metal in interdisciplinary research.

Chapter 2. Literature Review

2.1 Fluid dynamics of liquid metal (LM)

LM is a room-temperature fluid with the high surface tension (~ 550 mN/m).[10, 31-32] The excellent fluidity of LM largely arises from its low bulk viscosity, about 2×10^{-3} Pa s (two times the viscosity of water).[33-34] The kinematic viscosity of LM is about 3×10^{-7} m^2/s, while the kinematic viscosity for water is 10^{-6} m^2/s.[34] Thus, the mobility of LM is comparable to that of water, enabling it to flow like a liquid at room temperature. **Table 2.1** shows the physical properties of gallium-based LM alloys and water, including their melting points (MP).[27, 34] It should be noted that a thin oxide layer will be formed when the LM is in an oxygen environment (i.e., ambient conditions),[14, 35] which will limit the fluidity of the LM. This oxide layer can be removed with base (i.e., NaOH solution) and acid (i.e., HCl solution) solutions,[8, 10, 25-26] to regain the water-like fluidity of the LM. Moreover, various applications based on the fluidity of LM have been explored, especially in biomedical,[36-37] 3-D printing,[13, 38] and microfluid areas.[39-45]

Table 2.1 Physical properties of gallium-based LM alloy and water.[27, 34]

	MP [^{o}C]	Surface tension [mN/m]	Viscosity [10^{-3} Pa s]	Density [10^3 kg m^{-3}]	Kinematic viscosity [10^{-7} m^2/s]
Ga	29.8	720	1.37	6.08	2.25
Ga$_{75.5}$In$_{24.5}$	15.5	624	1.99	6.28	3.17
Ga$_{68.5}$In$_{21.5}$Sn$_{10}$	13.2	533	2.4	6.36	3.77
Water	0	72	1.0	1.0	10

Due to the fluidity and low-toxicity properties of the LM, biomedical application of the LMs is promising and attractive. Sun et al. proposed the concept of injectable LMs to substitute for surgical operations by injecting the LM into intestinal neoplasms and linking the LM with external power,[36] as in **Figure 2.1a**. Afterwards Chechetka et al. realized biomedical theranostics by fabricating transformable LM nano-capsules and injecting these capsules into microvascular obstructions.[37]

Moreover, the fluidity empowers the potential for the LM to work as a printable ink. Boley et al. proposed a directing writing method for the LM ink, and this method was achieved by passing flowing LM through a blunt syringe needle in close proximity to a moving substrate.[38] Zheng et al. then optimized this method onto a highly cost-effective and automatic printing method by using the LM based ink.[13] **Figure 2.1b** shows how the fluidity of the LM enables the direct printing of conductive patterns.

In particular, the fluidity of the LM is introduced into microfluidic research focusing on fabrication of the LM droplets, which has been intensively studied recently. Thelen et al. described an experimental study of the production of micro-scale droplets of an LM using a microfluidic flow-focusing device.[39] The device was filled with an aqueous glycerol solution, and the addition of polyvinyl alcohol (PVA) stabilized the monodisperse microspheres of the LM. Hutter et al. then even obtained non-spherical droplets with a device filled with oxygenated silicone oil due to the instantaneous formation of the oxide layers.[40] It should be noted that with the solutions used in these reports (**Figure 2.1.1c**), such as glycerol, PVA, polyethylene glycol (PEG), and oxygenated and deoxygenated silicone oil, even the surface oxide layer played the role of surfactant to stabilize the liquid metal droplets (LMDs) (preventing these droplets from merging). Yu et al. developed a low-cost and technically simple way for quickly preparing metal particles on a large scale by taking advantage of high surface tension of the LM.[41]

The LM was jetted from a syringe, and the surface tension forced the stream jet to naturally break into five stages of shapes including stream, neck appearing, shuttle shape, irregular shape, and spherical droplet, as shown **in Figure 2.1d**. Moreover, Fang et al. imposed a small-voltage direct current electric field on an LM in sodium hydroxide solution.[42] As in **Figure 2.1e**, this voltage would induce ejection of liquid metal inside the capillary tube and form discrete droplets. The droplet size was controlled by the aperture diameter of the capillary nozzle. Wang et al. improved this voltage-assisted method by shooting the LM stream onto an electrode plate.[43] **Figure 2.1f** shows that non-uniform droplets with sizes in the range from several micrometers to hundreds of nanometers were obtained through this method. To develop a more convenient method for controllable droplet size, Yang et al. demonstrated a novel method for controlling the size of liquid-metal microdroplets produced in a microfluidic flow-focusing system by using only voltage to control the surface tension of the metal.[44] **Figure 2.1g** indicates that the size and flow rate are controlled by the external voltage.
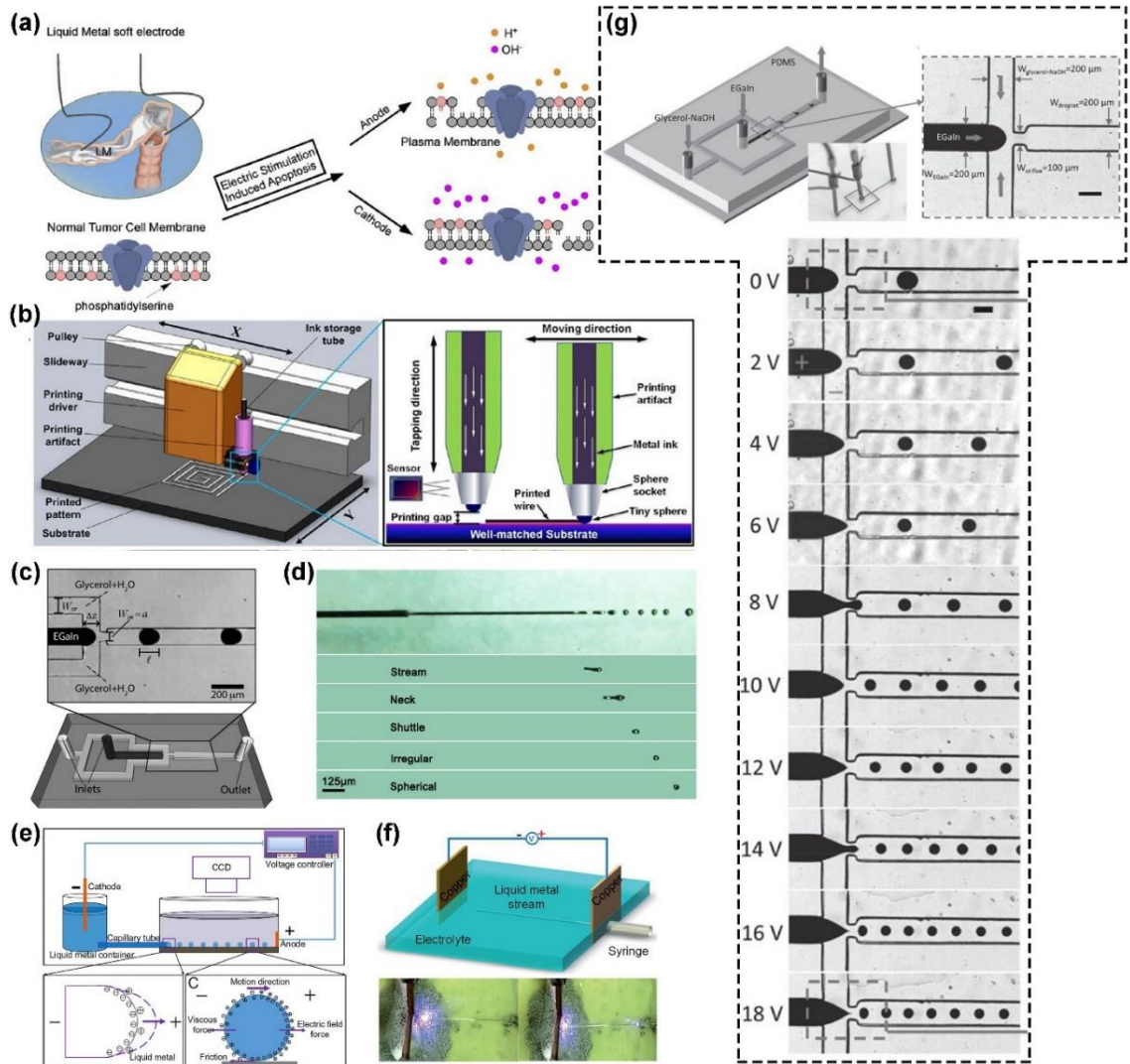
Figure 2.1. (a) Schematic illustration of the conceptual application and the mechanism induced by injectable LM soft electronics in the biomedical area.[36] (b) 3D diagram of the LM based printer to illustrate the tapping mode for adhering the liquid metal ink to the substrate.[13] (c) The model and micrograph of the flow-focusing device.[40] (d) Surface tension forced breaking of an LM stream jet for the formation of LM droplets.[41] (e) Schematic diagram of the experimental setup for voltage assisted formation of LM droplets, where the LM injection and droplet motion are driven by the electrohydrodynamic force.[42] (f) The LM droplets formed by shooting the LM stream to an electrode plate.[43] (g) Schematic diagram of the experimental setup for forming liquid

metal microdroplets, microscopic image of the flow-focusing section of the microfluidic chip, and the voltage-controlled flow rate and size of LM droplets.[44]

The novel fluidic phenomena of the LM are also investigated compared to traditional fluids (i.e., water and oil). For example, the non-coalescence phenomenon (liquid droplets on the same liquid bath) was observed in traditional liquids.[46] This phenomenon was further explored by coating droplets with hydrophobic powders,[47] using thermocapillary convection to drive thin films of a lubricating, surrounding gas on the bath surface,[48] using a flowing bath,[49-50] or heating the bath,[51] and causing the droplets to bounce and even float on the same liquid bath with vertical oscillation.[52] In the case of the LM based non-coalescence phenomenon, Zhao et al. reported that when applying an electric field gradient across the LM/electrolyte interface, a droplet can persistently surf on the interface without coalescence,[53] as shown in **Figure 2.2a**. They also introduced this phenomenon into the Faraday system, where, besides the bouncing effects of droplets, they also observed different wave evolution of the LM bath compared to oil,[54] as in **Figure 2.2b**. Tang et al. demonstrated an integrated pilot-wave field to control the droplet trajectories on the bath, via amplified bath capillarity, in which the local wave field generated by droplet bouncing was superposed on the global wave field induced by bath meniscus oscillation.[55] **Figure 2.2c** shows the orbital-chasing motion of LM droplets.

Moreover, the LM showed unique properties related to the formation of stream jets. Traditional jets (cylindrical streams of water and oil) can form transiently at higher fluid velocities, yet interfacial tension rapidly drives the jet to break up into droplets via the Rayleigh–Plateau instability. Song et al. reported the formation of long and stable LM streams, however, by overcoming the Rayleigh–Plateau instability, as shown in **Figure 2.2d**. The length of the LM stream could reach up to 64 cm.[11] And Han et al. also realized

the simultaneously solidification of the LM stream by using an automated stage,[56] as in

Figure 2.2e.
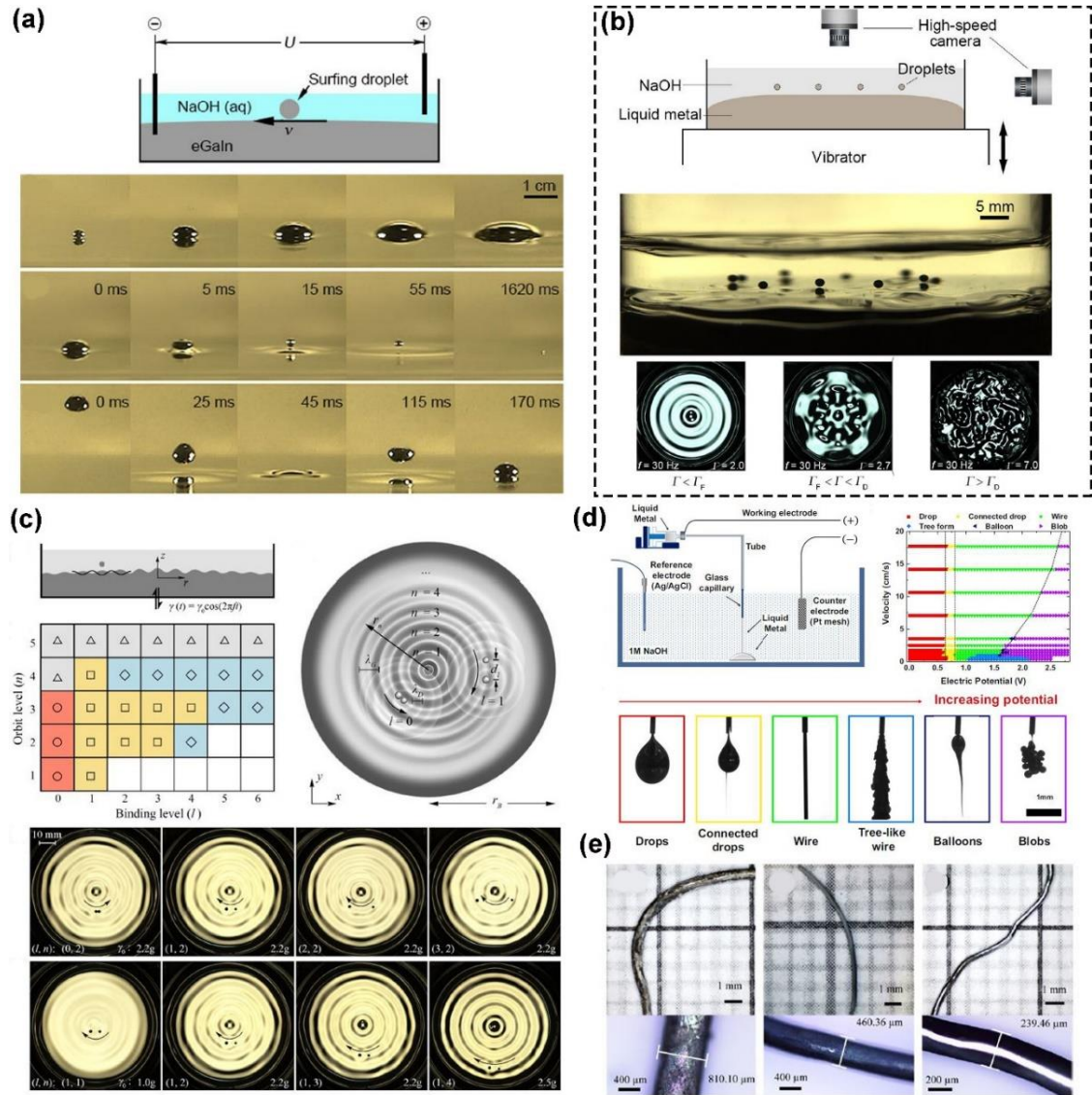
Figure 2.2. Novel fluidic phenomena of liquid metal. (a) Surfing liquid metal droplet on the same metal bath, schematic drawing of the experimental setup (first row), surfing droplets with various sizes (second row), a droplet merges with the LM bulk immediately as the applied voltage is switched off (third row), and an impacting non-coalescent LMD drops from 5 cm height (fourth row).[53] (b) The bouncing effects on droplets and different wave evolution of an LM bath.[54] (c) Schematic view and snapshots of the directional

orbital-chasing motion of the LM heterodimers and the definition of the regime parameters.[55] (d) The LM morphologies observed as a function of potential, a highly stable LM stream formed in suitable potential and velocity ranges.[11] (e) Optical microscope images of simultaneously solidified liquid metal streams.[56]

The conclusion was obtained from aforementioned research that the fluidity and low-toxicity properties of the LM enables applications in biomedical area and printable ink for direct patterning, which has great potential for practical usage. Moreover, the LM also shows attractive potential in microfluidic applications, in which the LMs could be used as flowing electrodes, liquid pumps or sensors, et al. The novel rheological phenomena of the LM compared to conventional liquids deserve more attention for systematic exploration and discovery.

2.2 Liquid metal as soft conductor

As excellent liquid conductors, the LMs combine conductivity and deformability. These unique properties have attracted intense attention for LM-based electronics,[2, 57] circuit interconnects,[7, 58-61] composite structures,[45] and other applications. Most relevant work has been mainly focused on the patterning methods for fabricating electronic devices (such as 3D printing[7, 62]), and the unique properties (such as self-healing[12, 63-65] and enhanced mechanical properties[63]) of composite structures.

2.2.1   Printed electronics based on liquid metal

For electronic devices and circuit interconnections, the LMs need to be patterned on different substrates. Thus, various methods to pattern liquid metals have been explored.[66] Zheng et al. were the first to develop a direct printing method to pattern liquid metal via

a tapping mode composite fluid delivery mechanism,[13] and they expanded this printing method to any substrate by developing another liquid metal printer based on the atomized spray printing method.[67-69] Moreover, the reconfigurable LM could further extend the 3D printing techniques to the manufacture of functional metal objects. Ladd et al. reported a method to direct-write three-dimensional liquid metal micro-components at room temperature with the help of the native oxide formed on the surface of LM.[7] Wang et al. also developed a compatible hybrid 3D printing method to simultaneously pattern metal and nonmetal (silicone rubber) inks together.[62] So far, these methods could be divided into four categories: I) lithography-enabled,[70-72] II) injection,[73-75] III) additive,[7, 76-77] and IV) subtractive,[8, 78-79] as shown in **Figure 2.3**.
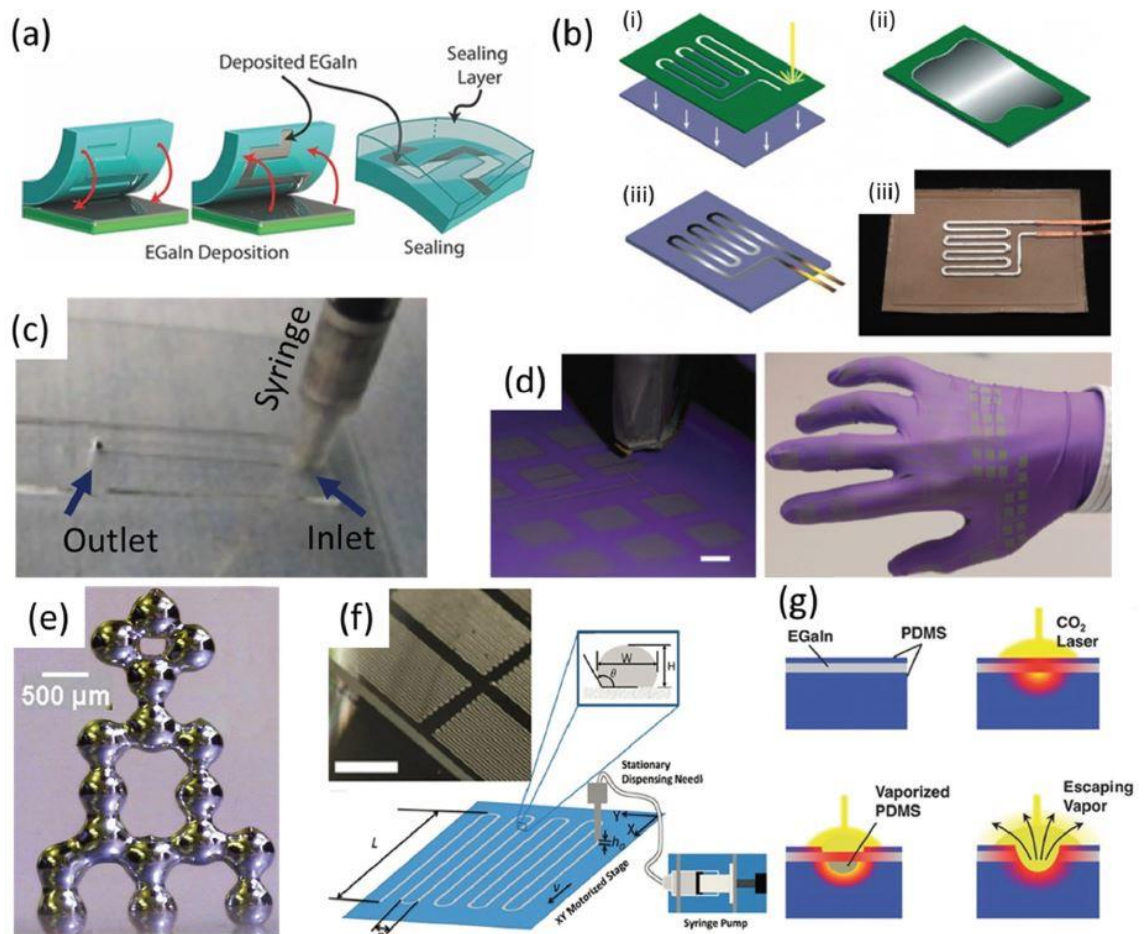
Figure 2.3. Simple and popular ways to pattern LM. (a) Filling the LM within a silicone mold. (b) Patterning LM on a receiving substrate across a stencil. (c) Injecting LM into microchannels for high-resolution structures. (d) Inkjet printing of small colloidal suspensions of LM droplets. (e) surface-oxide-layer-assisted 3D printed structures of LM. (f) 2D direct writing of LM. (g) Laser-ablation-assisted pattern films of LM in elastomer.[2]

2.2.2   Self-healing of stretchable liquid metal

Compared to the traditional electronic devices, which are typically composed of intrinsically rigid materials that have limited deformability, LM-based soft materials are highly flexible, stretchable, and conformable. Most importantly, they are capable of electrical self-healing, enabling their electrical functionality even under severe damage.[12, 61, 63-65, 80-85] So et al. proposed the concept of creating stretchable wire by filling a stretchable tube with the LM, realizing reversible deformation and self-healings,[12] as shown in **Figure 2.4a**. Later, Zhu et al. reported that these stretchable wires showed enhanced mechanical properties.[63] Then, Palleau[64] and Li[65] studied the self-healing of LM, and they revealed that the metal oxidizes so quickly when it is cut that it neither leaks from nor retreats into its microchannel. Bringing the cut interfaces together allows the metal to self-heal electrically. Guo et al. developed a non-contact magnetic self-healing method based on an Fe-doped LM (**Figure 2.4b**),[82] and Krisnadi introduced electric field for assisting self-healing (**Figure 2.4c**).[83] Markvicka et al. introduced soft-matter composite for mechanically robust, electrically self-healing circuit interconnects for power and data transmission that could instantaneously repair themselves under extreme mechanical damage,[61] as shown in **Figure 2.4d.**
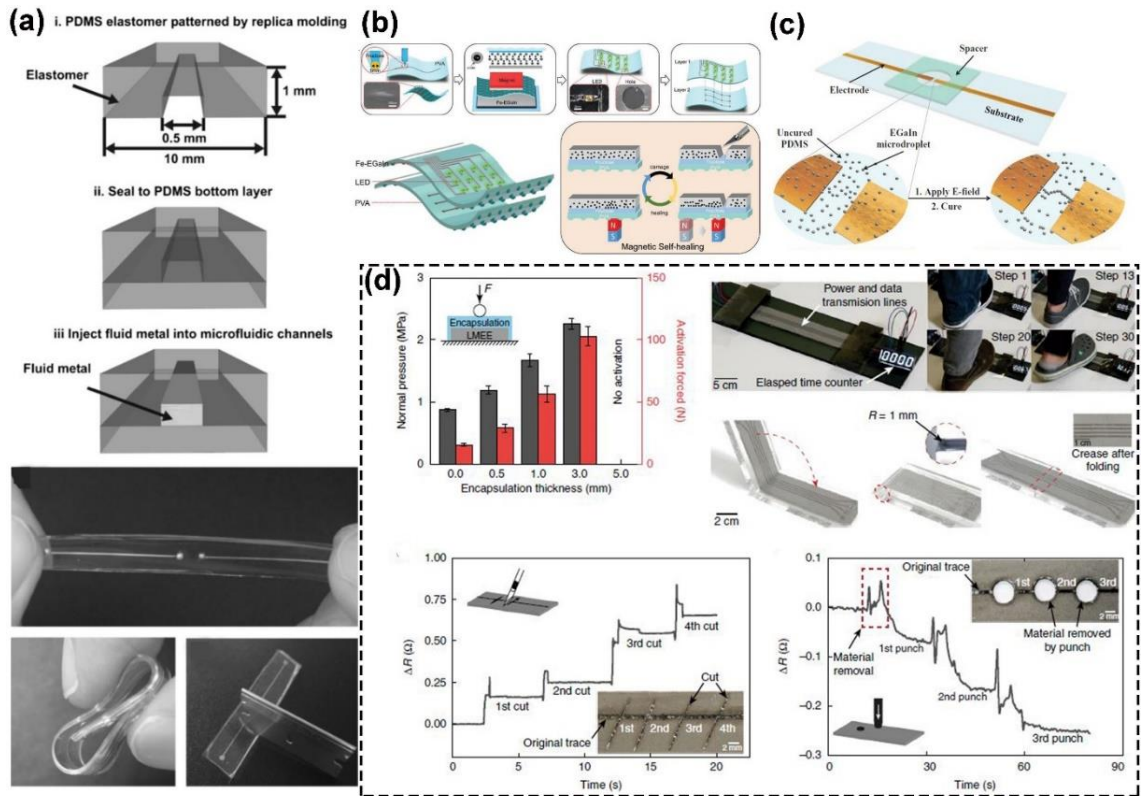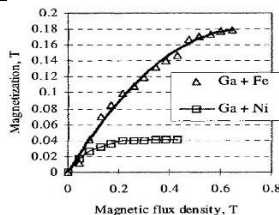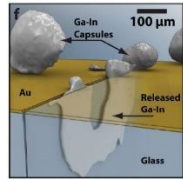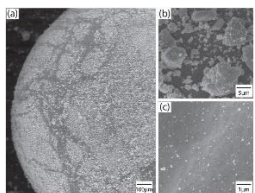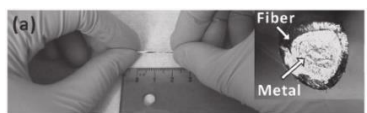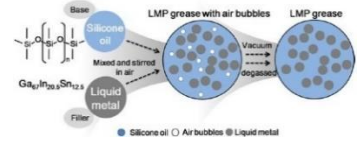
Figure 2.4. (a) Fabrication process of a reversibly deformable dipole antenna that can be stretched and rolled, with the antenna self-healings in response to sharp cuts, such as those inflicted by a razor blade.[12] (b) Non-contact magnetic self-healing method based on Fe-doped LM.[82] (c) Electric field assisted self-healing.[83] (d) Soft-matter composite for mechanically robust, electrically self-healing circuit interconnects, with photographs in the insets.[61]
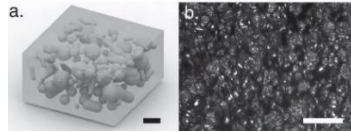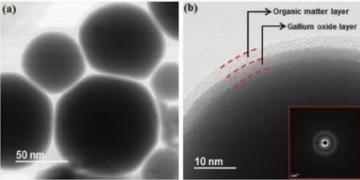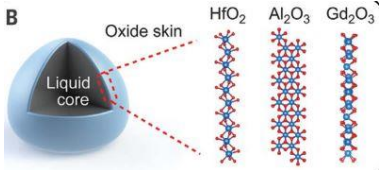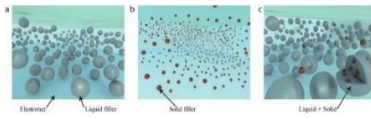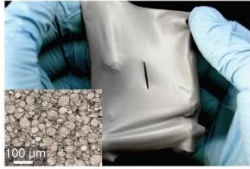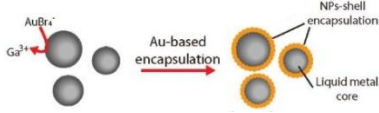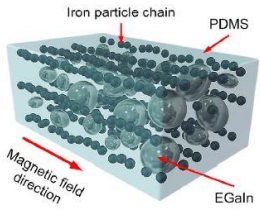
2.2.3 Composite structures of liquid metal
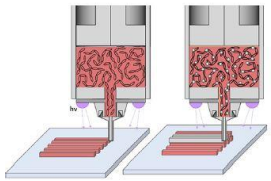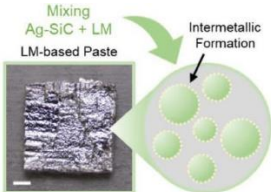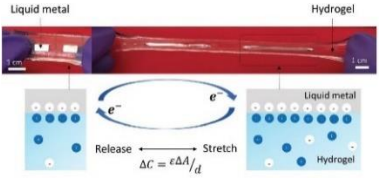
LM composites represent material systems in which LM alloys are either suspended as small droplets within a soft polymer matrix or mixed with metallic nanoparticles to form a biphasic composition. Through these, the electrical, dielectric, and thermal properties of composites can be controlled, thus enabling their applications in soft-matter sensing, actuation, and energy harvesting. Ito et al. was the first to use LM as a carrier for magnetic particles to create magnetic fluids in 2005.[86] This was followed by intensive

exploration for LM-based composite structures,[21-23, 63, 87-100] as shown in **Table 2.2**. And this research could be mainly divided into two categories: LM-polymer and LM-particles composites.

Table 2.2. Timeline of landmark academic works about LM composites.

Year	Materials	Composite structures	Representative images	Ref
2005	LM-Fe/Ni	Magneto-rheological fluid		86
2007	LM-CNTs/Au/Ag/Cu	Functional LM fluid		87-89
2012	LM-urea-formaldehyde (LM-UF)	Self-healing circuit		90
2013	LM-Teflon/silica/WO$_3$/ TiO$_2$/MoO$_3$/In$_2$O$_3$/ Carbon nanotubes	LM marble-based sensor		21-22
	LM (core)- triblock copolymer (shell)	LM based stretchable fiber		63
2014	LM-methyl silicone oil	LM poly greases		91

Year	Material	Application		Ref.
2015	LM-PDMS	Conductive polymer		92
2016	LM-oxide layer-organic surface	LM droplets based stretchable circuits		96
2017	LM-Hf/Al/Gd	Multi-functional surface oxide layer		14
2018	LM/metal microparticle-silicon elastomer	Multi-phase composites		94
	LM-silicone	Extreme tough elastomer		93
2019	LM- alkaline KAuBr$_4$	Au-LM Frameworks with enhanced mechanical stability		23
2020	LM- carbonyl Fe ferromagnetic microparticles-PDMS	LM based piezoelectric composites		97

	LM-liquid crystal elastomer	Printable composites		99
2021	LM-SiC/Ag	LM multiphase composites with thermal conductivity enhanced		100
	LM-hydrogel	Soft electric-double-layer energy harvester		98

For the LM-polymer composites, LM droplets are suspended in various polymers such as methyl silicone oil, poly (methyl methacrylate) (PMMA), poly (n-butyl methacrylate) (PBMA), and polydimethylsiloxane (PDMS). The main challenge for these composites is to controllably obtain different sizes of LM-droplets (LMDs), due to the enormous dominant surface tension of LM. To overcome this challenge, various methods have been explored for controllable LM-polymer composites,[96, 101-104] such as ultrasound sonication,[96, 101] atom-transfer radical polymerization,[102] *in*-situ etching,[104] and LM-based nebulization,[105] as shown in **Figure 2.5**. Ultrasound sonication was utilized to first prepare LM nanodroplets, which were subsequently dispersed in uncured polymer.[101] The dispersion of LM through the ultrasonication method, however, is always accompanied by reaggregation of the LM, and efforts have been made to improve this method.[102, 106-107] Yan et al. introduced surface-initiated atom-transfer radical polymerization (ATRP) as a versatile synthesis method for LM-polymer nanocomposites,[102] resulting in the LM

droplets that are uniformly dispersed throughout the composites. Most importantly, this method enabled the fabrication of nanocomposites by direct assembly of polymer-modified LM nanodroplets.
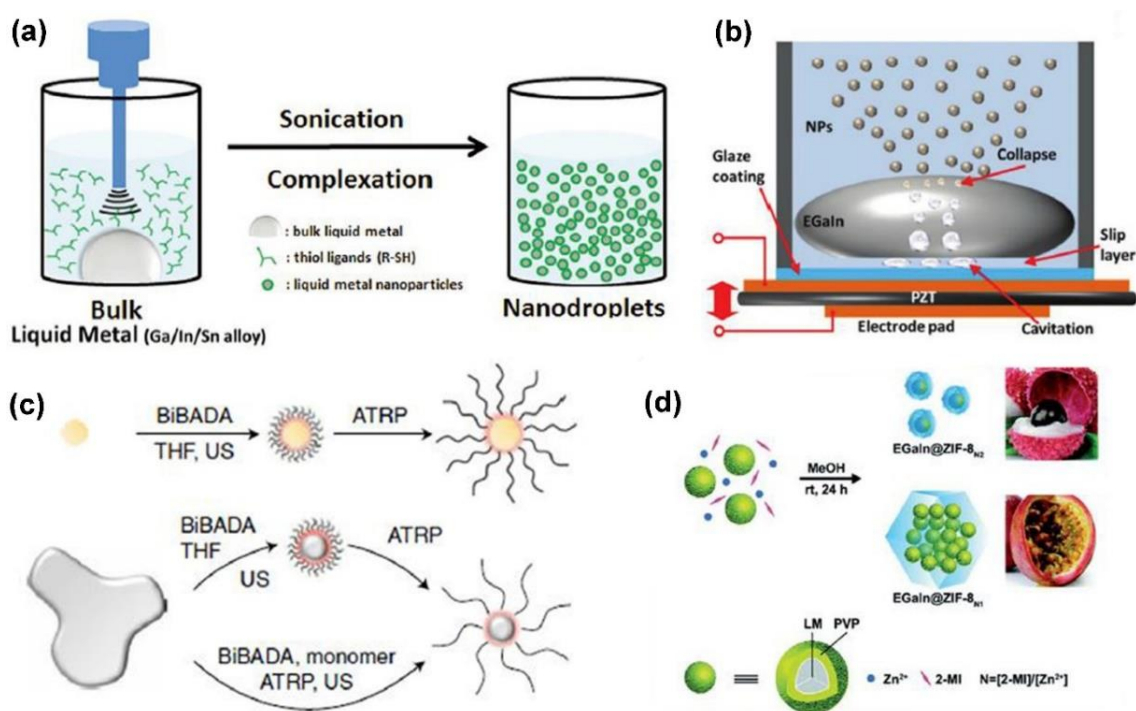
Figure 2.5. Various methods for controllable LM-polymer composites. (a) Schematic illustration of the preparation route for LM droplets produced via ultrasound.[96] (b) Schematic illustration of the mechanism for producing LM nanoparticles by liquid-based nebulization.[105] (c) (i) Two-step12-(2-bromoisobutyramido)dodecanoic acid (BiBADA) functionalized and surface-initiated ATRP of nanoparticles. (ii) Stepwise functionalization of LM or surface-initiated ATRP from *in*-situ functionalized LM droplets.[102] (d) Schematic illustration of the synthesis of "litchi"- and "passion fruit"-like EGaIn@ZIF-8 NPs, where ZIF-8 is zeolitic imidazolate framework-8 and NP stands for nanoparticle. Pre-synthesized EGaIn@PVP nanodroplets, where PVP is polyvinylpyrrolidone, are mixed with 2-methylimidazole (2-MI) and Zn^{2+} at different L/M ratios (2 and 1).[104]

The LM-particle composites are realized by doping non-metallic and metallic elements into the oxide shell or the liquid core of LM droplets, enabling LM-based composites with new functionalities and enhanced properties.[21-23, 29, 45, 87-88, 108-124]

For non-metallic particles, the oxide shell coating is realized by the strong cohesive forces between the particles and the LM.[22, 29, 108-112] Sivan et al. developed various composites by coating LM droplets with insulators (Teflon and silica) and semiconductors (metal oxide and carbon nanotubes).[21] These composites demonstrated the potential for controllable motion through electrochemical and photochemical reactions as well as magnetic field.[29, 110-111] Tang et al. found that the movement of the composite (LM coated with tungsten oxide) in aqueous media could be controlled by using an electrical current.[29] The coating methods as well as the manipulation of motion are shown in **Figure 2.6**.
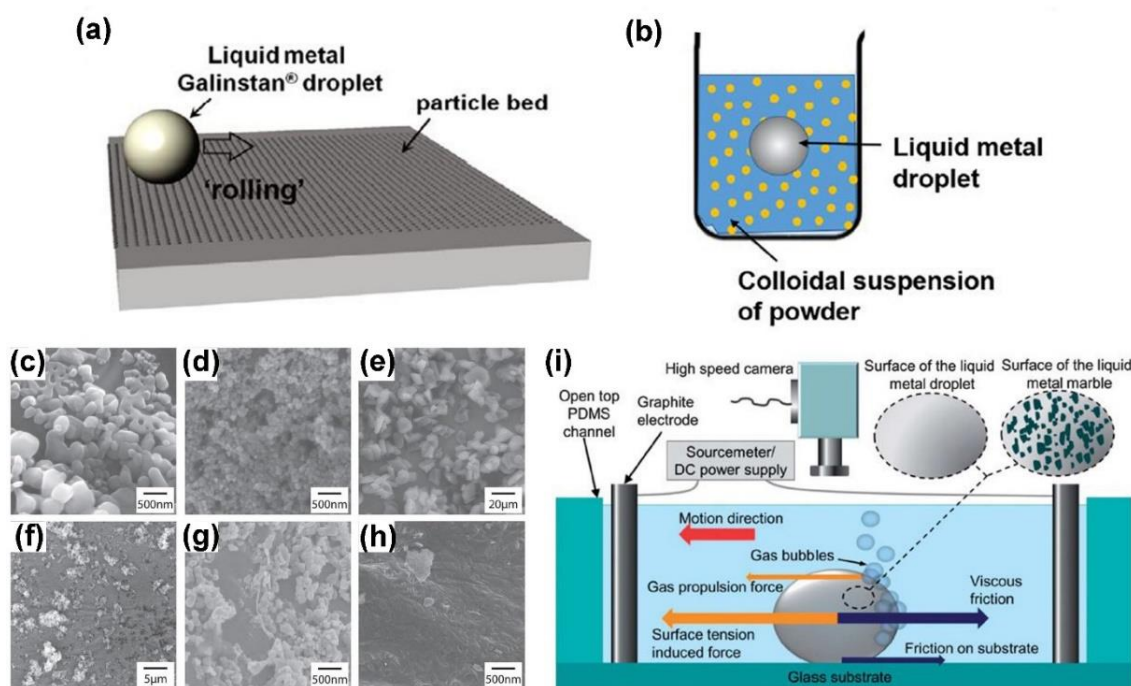
Figure 2.6. LM-based composites with non-metallic particles. (a) Schematic illustration

of rolling a liquid metal droplet on a powder bed.[112] (b) Schematic illustration of submerging a liquid metal droplet in a powder colloidal suspension.[45] (c-h) SEM images of different powders that were coated on the surface of Galinstan by rolling on a powder bed: c) ZnO nanoparticles, d) In_2O_3 nanoparticles, e) Al_2O_3 powder, f) Teflon powder, g) TiO_2 nanoparticles, and h) single wall carbon nanotubes.[21] (i) Schematic illustration of the experimental setup showing the forces influencing the motion of a Galinstan droplet with or without a nanoparticle coating.[29]

And so far, most LM-particle composites are focused on LM-metallic particles to form a biphasic LM-based composite. LM droplets are usually mixed with metallic particles such as Au, Ag, Cu, Fe, Ni, and W for enhanced thermal conductivity, electrical and mechanical properties, magnetic properties, and manipulation of their motion,[23, 88, 113-122] as shown in **Figure 2.7**. The LM-metallic particle composites are usually formed with the aid of mechanical mixing,[116, 123] electrochemical reaction,[88, 124] or ultrasonic agitation.[23] For example, David et al. introduced a controllable process for the synthesis of Au-coated LM droplets through ultrasonic agitation, and the droplets showed enhanced mechanical stability due to the thin layer of Au or the bimetallic AuGa2 on the surface.[23]
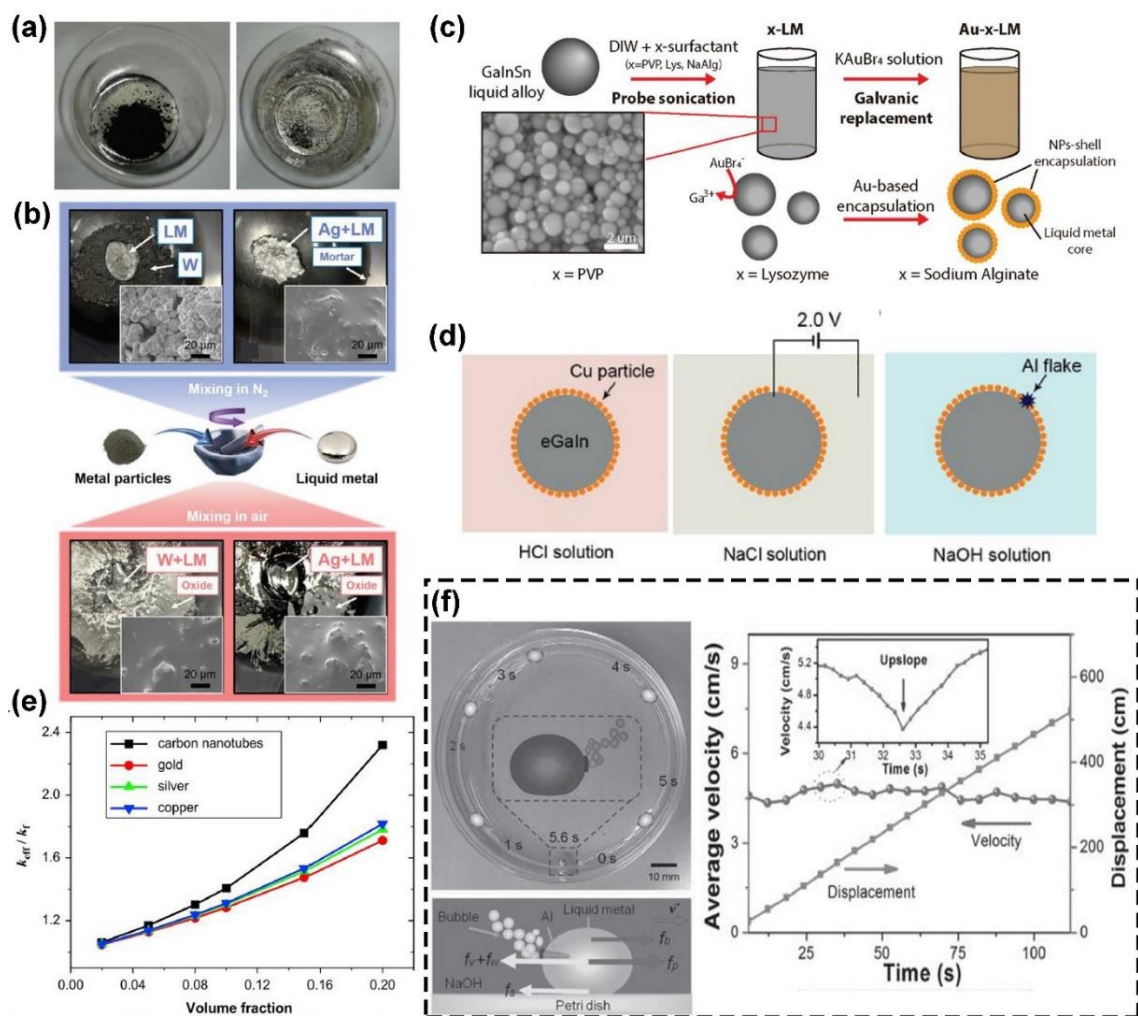
Figure 2.7. Synthesis strategies, manipulated properties and motions of LM-metallic composites. (a) Appearances of gallium and Ni particles before and after stirring.[123] (b) Schematic illustration of LM-X fabrication, where X stands for various metal particles. The metals are shear mixed with LM in a mortar and pestle, and the images show the paste-like morphology of LM-W and LM-Ag in the mortar.[120] (c) A macro-sized Ga-alloy droplet is ultrasonically dispersed in an aqueous solution to form sub-micrometer LM droplets.[23] (d) Methods to realize LM-phagocytosis in different solutions.[88] (e) Improved thermal conductivity when the LM is doped with different particles.[87] (f) Self-fueled liquid metal motor running in a circular petri dish with schematic illustration of the forces affecting the velocity of the motor, and average velocity and displacement plots as functions of time.[119]

At the initial stage for research on LM-metallic particle composites, which could be as far back as 2007, Liu's team proposed the concept of nano LM for enhanced thermal conductivity.[87] Tang et al. further developed another method for LM-copper (Cu) particles composites in acidic solution (HCl), neutral solution (NaCl), or alkaline solution (NaOH) by electrochemical reaction, resulting in enhanced electrical, thermal and mechanical properties for the composites.[88] Kong et al. synthesized LM-tungsten (W) composites with both enhanced wettability and thermal conductivity, proving that tungsten particles could be successfully mixed with LM in oxygen-rich environments despite the resistance of tungsten to forming alloys at room temperature.[120]

Moreover, integration of magnetic particles such as Fe,[118] gadolinium (Gd)[117] and Ni into liquid metals has untapped new functions for LM-based systems, among which LM-Ni composites are the most well studied system. Zhang et al. demonstrated an electroplating process for coating Ni layers on the surface of LM droplets with the help of external voltage.[124] Xiong et al. fabricated a desirable magnetic fluid by mechanically mixing the Ni particles with LM, so that the stirring could contribute to improving the wettability and compatibility of the LM with various materials due to oxidization.[123] Following reports showed the potential of LM-Ni particles composites for direct-writing of flexible electronics due to the superior wettability and strong adhesion of the composites.[114-116]

In addition to these enhanced properties, the LM-metallic particle composites also play an important role in LM soft machines. Zhang et al. first proposed synthetic self-fueled motors based on LM-Al composites, and such a motor with a diameter of milli-/centimeters could swim at a high velocity (~ centimeters per second) under the driving force generated from the unbalanced bipolar electrochemical reaction.[119] Later, Liu's

team expanded this concept of motor to high-frequency self-powered oscillation[121] and electric-field-controlled LM motors.[122]

In summary, the LMs combine conductivity and deformability to act as soft conductors. Ultra-stretchable electronic devices/circuit interconnects are realized by pattering the LMs on different organic substrates. These devices show unique properties, such as self-healing and enhanced mechanical properties. Moreover, multi-functional LMDs are obtained with enhanced electrical/thermal/mechanical properties and wettability by forming composites of the LMDs with other particles that are either non-metallic (i.e., Teflon, silica) or metallic (i.e., Au, Ag, Fe). These composite structures have drawn most of the attention in the research on LM with systematic exploration. There is still plenty space, however, for expanding the composite structures to more functional materials fields (e.g., energy harvesting).

2.3 Core-shell structure of liquid metal

As mentioned above, a thin oxide layer will be formed when LM is in an oxygen environment (i.e., ambient conditions) at the metal-air interface,[14, 35] and this unique core (LM)-shell (surface oxide layer) structure endows the LM with multifunctional properties. For example, the oxide layers limit the fluidity of LM, thereby enabling the LM to assume a designed shape.[125] The oxide layers also enhance the wettability of LM, contributing to the formation of composite structures of LM.[7, 125-126] Most importantly, the atomically thin surface oxide is considered a naturally occurring two-dimensional (2D) material, which could be deposited onto appropriate substrates via the van der Waals exfoliation technique.[14] Moreover, the oxide layer also enables various phenomena and properties of the LM alloy, such as unique surface patterns,[127] room temperature CO_2 reduction,[128] and catalysis.[129]

2.3.1 2-D metallic compound synthesized on the surface of the LM

Based on this core-shell structure, Zavabeti et al proposed the concept of using an LM as a reaction environment for atomically thin metal oxides,[14] since co-alloying with suitable reactive metals can form co-alloyed metal oxides at the metal-air interface. The synthesis of different metal oxides is on the basis of thermodynamic considerations, and the oxide resulting in the greatest reduction in the Gibbs free energy will dominate the surface.[14] In addition to various metal oxides produced through the co-alloying process, other types of functional metallic compound, such as the Group IV monochalcogenides (MX, M = Sn, Ge, Pb, etc. and X = S, Se), can be also synthesized on the surface of the LM.[130] To concretize this concept for the synthesis of 2D materials, **Figure 2.8** summarizes basic information on the low melting point metal, including all the LMs, the elements soluble in LMs, and the elements reacting with LMs.[3]

Figure 2.8. Strategy for the formation of LM based 2-D materials, including the co-alloying and surface reactions of LM with other elements.[3]

To obtain the desired 2-D functional thin film on the LM surface, different LM/LM alloy should be prepared before exposing them to a designed atmosphere (O_2, H_2S, etc.) based on the reduction of Gibbs free energy. **Table 2.3** tabulates the reduction of Gibbs free energy of single element oxides, and it indicates that most metal oxides can be synthesized based on Ga/In/Sn metal or metal alloy.[14, 131-132] Moreover, among these LM forming elements in **Figure 2.8**, the melting point of Ga is 29.8 °C, while the melting point of In and Sn is 156.6 °C and 231.9 °C, respectively. Thus, alloying with Ga/In/Sn can significantly reduce the melting point of metallic alloys. **Table 2.4** summarizes the compositions and melting points of low melting point metals and eutectic binary/ternary alloys. Based on the reduction of Gibbs free energy in **Table 2.3**, desired metal oxides on the surface are available with suitable LM alloy, as shown in **Table 2.4**.

Table 2.3. LM/LM alloy strategy and tabulated reduction of Gibbs free energy of oxides.[14, 131-132]

LM as Solvent	Oxides on the surface	ΔG (kJ mol^{-1})
	Nb_2O_5	-1766
	Gd_2O_3	-1732.3
	Ce_2O_3	-1706.2
	Al_2O_3	-1582.3
Ga/In/Sn/Bi	Ti_2O_3	-1434.2
	V_2O_5	-1419.5
	HfO_2	-1088.2
	Cr_2O_3	-1058.1
	ZrO_2	-1042.8

	CeO$_2$	-1024.6
	Fe$_3$O$_4$	-1015.4
	Ga$_2$O$_3$	-998.3
In/Sn/Bi	TiO$_2$	-888.8
	In$_2$O$_3$	-830.7
	Sb$_2$O$_5$	-829.2
	Co$_3$O$_4$	-774
	MoO$_3$	-668
Sn/Bi	Pb$_3$O$_4$	-601.2
	MgO	-569.3
	SnO$_2$	-515.8
Bi	Bi$_2$O$_3$	-493.7

Table 2.4. Melting points of pure metals, and eutectic binary and ternary alloys.[3]

Alloyed elements	Element A (at%)	Element B (at%)	Element C (at%)	MP (°C)
Ga	100			29.8
In	100			156.6
Sn	100			231.9
Bi	100			271.4
Pb	100			327.5
Zn	100			419.5
Ga/In	85.8	14.2		15.4
Ga/Sn	91.7	8.3		21.0
Ga/Bi	38.3	61.7		222.0

Ga/Al	97.6	2.4		25.9
Ga/Zn	96.1	3.9		24.7
In/Sn	52.7	47.3		116.9
In/Bi	79.2	20.8		72.5
In/Zn	96.2	3.8		143.7
Sn/Bi	60.9	39.1		138.3
Sn/Pb	74.9	25.1		185.1
Sn/Zn	85.2	14.8		199.0
Ga/In/Sn	78.3	14.9	6.8	13.2
In/Sn/Bi	60.1	18.8	21.1	62.0
Bi/Pb/Sn	40.7	16.4	42.9	98.0

For those metals with high melting points (Hf: 2500 °C and Gd: 1585 °C), however, it is not suitable to form the eutectic binary/ternary alloys with low melting points. Hence, considering that the thickness of the 2-D film on the LM surface is nanoscale (~3 nm),[14] very small amounts of metal elements are needed for a desirable film. Thus, a suitable alloy in **Table 2.4** (eutectic Ga/In/Sn alloy: Galinstan) can be used as the base LM, and other elements can be co-alloyed into it. Zavabeti et al. alloyed ~1 wt % of elemental Hf, Al, and Gd (powders with average particle in micron size) into Galinstan with the help of grinding amalgamation. The corresponding metal oxides (i.e., HfO_2, Al_2O_3, and Gd_2O_3) had a thickness of ~ 3 nm, as shown in **Figure 2.9a.** They employed LM to synthesize 2D nano films of metal oxides based on the core-shell structure of the LM, which expands the world of 2D materials. Based on this strategy, Daeneke et al. reported a method that allows harvesting monolayer of semiconducting stannous oxide nanosheets (SnO) from the interfacial oxide layer of liquid tin.[18] Moreover, Alsaif et al synthesized *p*-type tin

oxide and *n*-type indium oxide from the surface of molten tin and indium, respectively.[15] A large area heterostructure was constructed, as shown in **Figure 2.9b**. Messalea et al. obtained a Bi_2O_3 monolayer from molten bismuth, and ultraviolet photodetectors were developed by using this *n*-type monolayer.[19] Afterwards, Ghasemian et al. developed 2D PbO thin films when they exposed the molten Pb to ambient atmospheric conditions.[133]

To expand the application of the core-shell strategy, Ghasemian et al. developed a method for galvanic growth of MnO_2 monolayers by exposing the bulk LM and LMDs produced by ultrasonic agitation to aqueous solutions of $KMnO_4$. Galvanic replacement occurs at the interface of the LM and solution, where the surface of the LM serves as the sacrificial substrate for the formation of hydrated MnO_2 sheets.[134] Moreover, Ren et al. explored a new programmable preparation of complex core–shell structures of LM droplets by a localized galvanic replacement reaction in one ultrasonication,[135] and high-level compositional diversity of both the core and the shell layers was achieved, such as $Ga@MoO_x$–Cu, $GaInSn@MoO_x$, $InSn@MoO_x$, $InSn@MnO_x$, $InSn@MoO_x$–VO_x, and Ga@Ni, as shown in **Figure 2.9c**. Similarly, Wang et al synthesized 2D molybdenum sulfides on the LM surface in an aqueous solution of ammonium tetrathiomolybdate $((NH4)_2MoS_4)$,[136] and a cupric oxide sheet was formed on the LM surface in an aqueous solution of $CuSO_4$ and NH_4OH.[137] Moreover, bismuth telluride topological insulator for NO_2 selective sensing was synthesized by Mousavi et al by using LMDs covered with a solution of Bi^{3+} - $HTeO_2^+$.[138]

Transition metal chalcogenides were also explored based on the LM core-shell strategy. Khan et al. reported large-area monolayer SnS synthesis using the core-shell strategy by exposing molten droplets of Sn to a sulfur source (50 ppm H_2S gas in N_2 background) at 350 °C,[139] as shown in **Figure 2.9d**. This monolayer SnS also showed great potential for application in multi-functional devices, **Figure 2.9e** shows high performance

piezoelectric nanogenerators and broadband photodetectors fabricated based on the monolayer SnS.[130, 139]
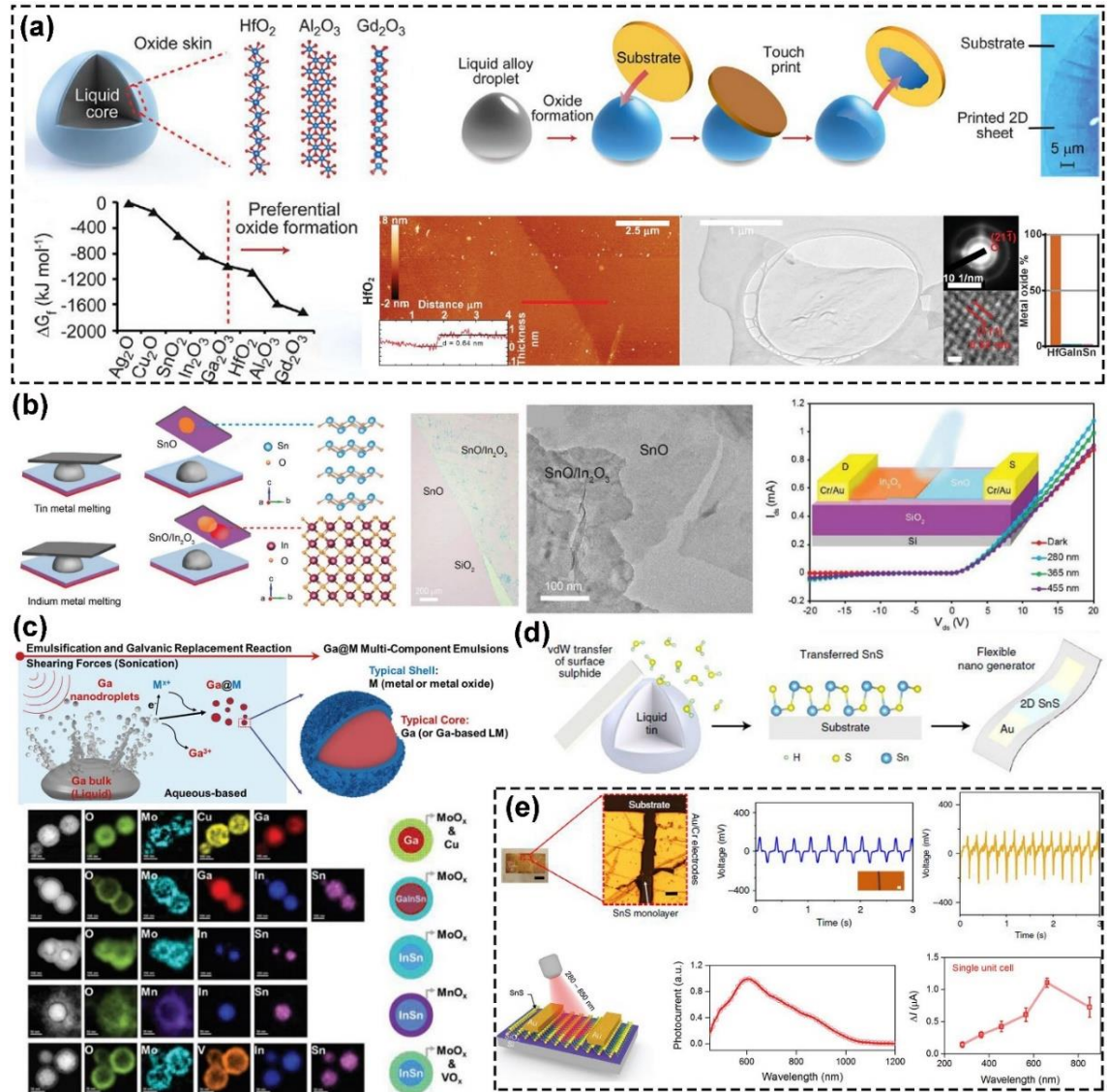
Figure 2.9. One-step synthetic strategy for metal compounds based on the core-shell structure of the LM. (a) Fundamental principles, synthetic approach based on the core-shell strategy, and deposition of film with nano-size thickness of HfO_2.[14] (b) Schematic illustration and characterization of 2D SnO/In_2O_3 heterostructure.[15] (c) Schematic illustration of the synthetic approach to complex core-shell structures by the localized galvanic replacement reaction.[135] (d) The synthetic approach for monolayer SnS.[139] (e)

High performance piezoelectric nanogenerators and broadband photodetectors fabricated based on the monolayer SnS.[130, 139]

These above-mentioned core-shell strategies involve one-step formation of the metal compounds (metal oxides and chalcogenides), and more multi-step syntheses for other metal compounds have also been developed. Carey et al. produced a three-step method for formation of large area two-dimensional semiconducting GaS with unit cell thickness (~1.5 nm).[17] As shown in **Figure 2.10a**, the oxide layer was first formed on the surface of the LM, attached to a substrate (SiO_2/Si), and then a hydrochloric acid (HCl) vapor treatment was used as an intermediate step to transform the gallium oxide layer into $CaCl_3$. Finally, the $CaCl_3$ layer was sulfurized via a relatively low temperature process (~300 ^oC), while traditional direct sulfurization of gallium oxide requires a high temperature (~600 ^oC with sulfur powder).[140] This multi-step strategy can also be applied to the formation of those materials which cannot be synthesized via conventional methods. For example, gallium phosphate ($GaPO_4$) is an archetypal piezoelectric material, which does not naturally crystallize in a stratified structure. Thus, Syed et al. reported a multi-step strategy for the formation of $GaPO_4$ by exfoliating the interfacial oxide layer of the LM, and following this by a vapor phase reaction [300 – 350 ^oC with H_3PO_4 in N_2 atmosphere,[141] as shown in **Figure 2.10b**. Considering the size limit for attaching the oxide layer to the substrate (millimeter scale), this team developed a two-step process for a centimeter-scale oxide layer by utilizing squeeze-printing of the LM and then converting the oxide layer into GaN using ammonolysis in a tubular furnace,[20] as show in **Figure 2.10c**. Moreover, Zavabeti et al developed a method that involved adding aluminum to a room temperature alloy of gallium and then exposing the LM to either liquid water or water vapor, which allowed the growth of either 2D sheets or one-

dimensional (1D) fibers, respectively.[142] **Figure 2.10d** shows the method and the growth

mechanism with liquid water (bubble-assisted exfoliation process) and water vapor

(vapor-nucleation-assisted fibrous structure).
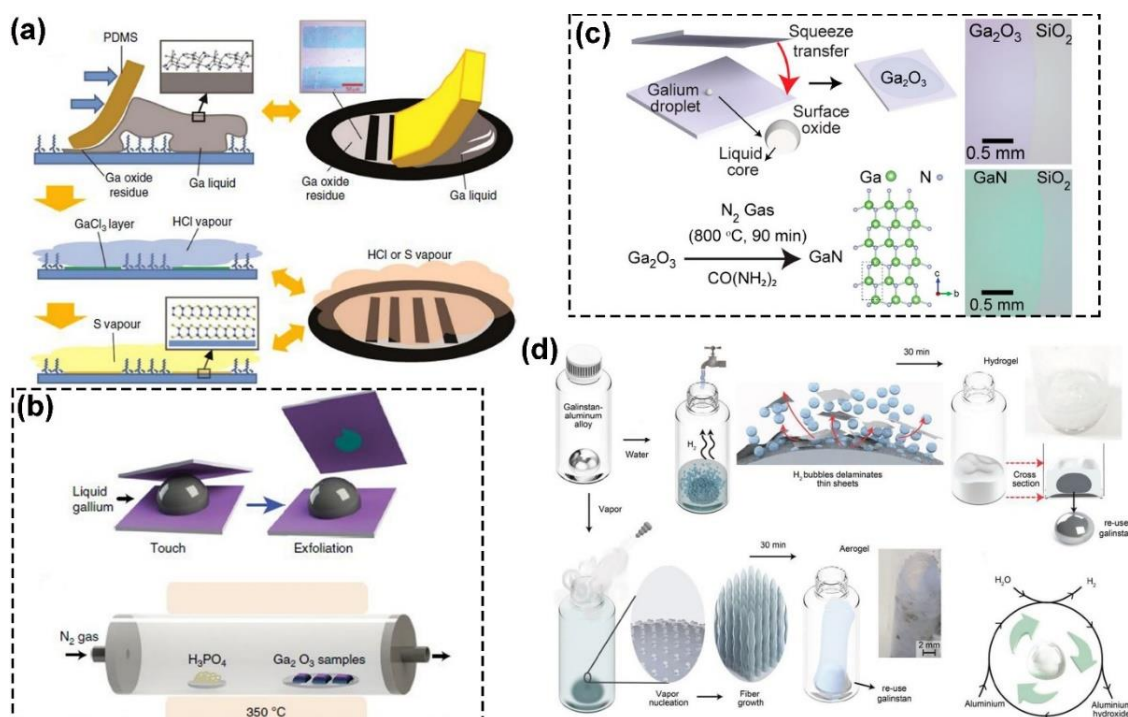
Figure 2.10. Multi-step strategy for the formation of metal compound. (a) three-step

formation of large-area two-dimensional semiconducting GaS.[17] (b) Two-step formation

of GaPO$_4$.[141] (c) Two-step process for centimeter scale oxide layer fabricated by utilizing

squeeze-printing.[20] (d) Water- and water-vapor-assisted formation of 2D sheets or 1D

fibers of Al/Ga LM alloy.[142]

2.3.2   Core-shell structure enabled unique properties of LM alloy

As mentioned above, for the core-shell structure, the oxide resulting in the greatest

reduction of Gibbs free energy will dominate the surface.[14] That is, for eutectic

gallium−indium based LM (EGaIn), the surface oxides should always be gallium oxides

(i.e., Ga$_2$O$_3$). Cutinho et al., however, discovered an autonomous thermal-oxidative

57

composition inversion method and texture tuning of the EGaIn.[143] The LM was under heat treatment from ambient to high temperature. The LM exhibited a smooth texture on the surface, but an anisotropic surface with different oxide thickness was observed at 400 °C. At this temperature, the surface oxides are rich in Ga (mainly Ga_2O_3). Significant changes in texture on the surface appeared from 500 °C, however, and this tier was composed of the indium oxide (In_2O_3), as shown in **Figure 2.11a**. This composition inversion and texture tuning indicates an uneven distribution of metallic elements as well as unusual movements of the metallic elements driven by the reformation of LM alloy. Such an anisotropic surface was also observed for the eutectic bismuth-tin ($EBi_{57}Sn_{43}$) based LM alloy,[144] as in **Figure 2.11b**. Based on this anisotropic surface phenomenon, Tang et al. developed unique surface patterns during solidification of eutectic bismuth-gallium (EBiGa) based LM alloy.[127] **Figure 2.11c** shows the highly ordered surface patterns, which involve an atomic Bi layer under a self-limiting few-nanometer Ga_2O_3 layer. The gallium oxide layer prevents the Bi layer underneath from being oxidized. They revealed that the internal Bi atoms diffused towards the surface Bi island, this directional mobility of Bi atoms and confinement by the surface Ga_2O_3 layer enabled these patterns. Besides these unique phenomena, the core-shell structure also endows the LM with multi-functional properties. For example, LM catalysts are attracting significant attention, owing to their unique properties and their exceptional ability to support homogeneous and heterogeneous catalysis.[129] Esrafilzadeh et al. created an LM electrocatalyst at the liquid metal/electrolyte interface.[128] Instead of depositing the surface oxide layer on a substrate, their LM with cerium oxide (Ce_2O_3) could be directly utilized as an electrocatalytic system, successfully converting CO_2 to carbonaceous and graphitic products at room temperature, as shown in **Figure 2.11d**.
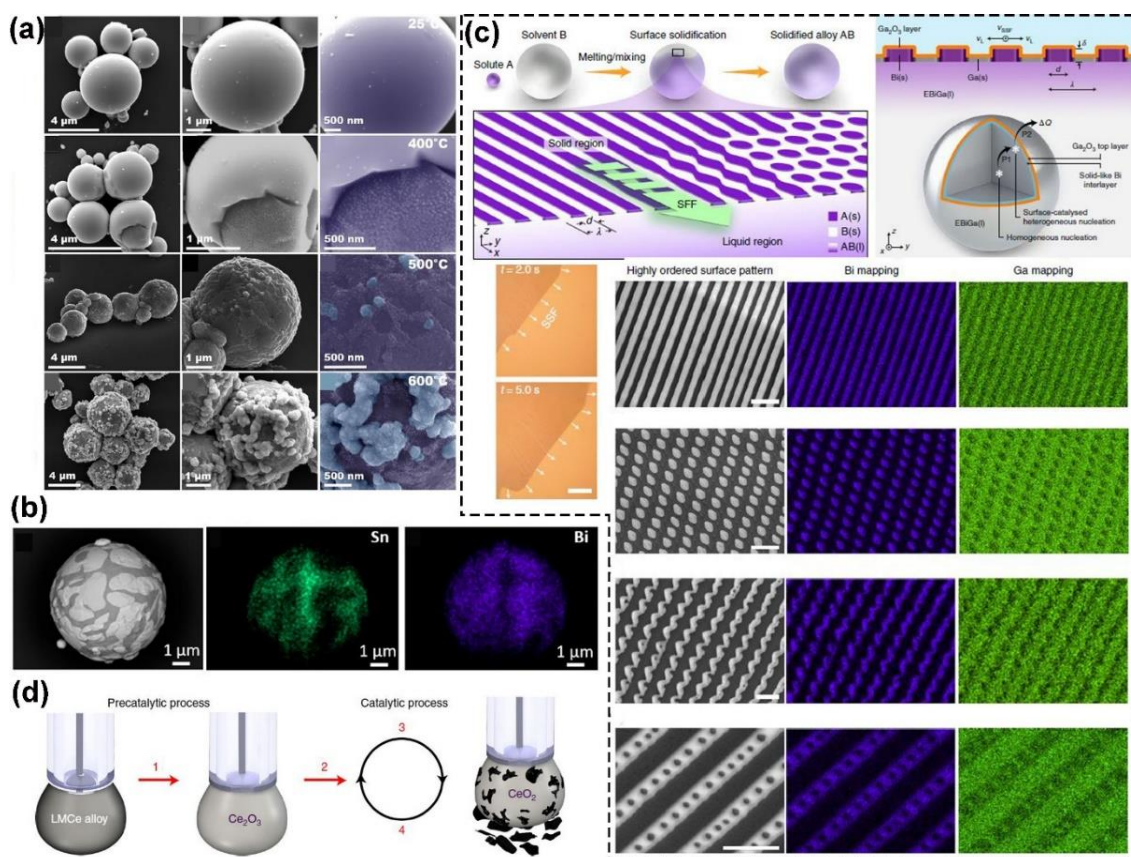
Figure 2.11. The core-shell structure enables unique phenomena and properties of the LM. (a, b) The anisotropic surface phenomenon of LM alloy.[143-144] (c) Unique surface patterns during solidification of EBiGa-based LM alloy.[127] (d) LM electrocatalyst at the liquid metal/electrolyte interface, converting CO_2 to carbonaceous and graphitic products at room temperature.[128]

This unique core-shell structure of the LM expands the synthesis possibilities for 2D thin films, which could be deposited on designed substrates to assemble functional devices or used as *in-situ* catalysts/sensors. And it also provides new strategies for surface patterning. Most importantly, the core-shell structure of the LM has enormous potential in multidisciplinary interaction (e.g., energy harvesting).

2.4 Magnetic actuation of liquid metal/magnetic particle hybrids

As aforementioned, the core-shell structure of the LM enables LM composite structure with other functional particles. It has been reported that magnetic actuation can be used for LM manipulation by dispersing magnetic particles into or coating them onto LM. The LM based ferrofluid is formed by dispersing magnetic particles into LM.[89, 117] Castro et al. demonstrated a magnetocaloric ferrofluid by suspending gadolinium nanoparticles into an LM,[117] as shown in **Figure 2.12a**. This LM/Gd ferrofluid exhibited spontaneous magnetization and featured a large magnetocaloric effect, thereby showing the potential for magnetocaloric cooling as well as fluidic magnetocaloric devices. Moreover, a magnetic field could be applied to control the motion of the LM hybrid with magnetic particles.[112, 145-148] Kim et al first proposed a magnetic-field-driven LM (coated with iron particles) in microfluidic channels filled with a base or acid solution.[112, 145] The LM moved in channels with different angles and cross-linked channels in any direction corresponding to the position of an external magnet, and was capable of working as an electrical switching in the channel for turning on/off light emitting diodes as designed,[145] as shown in **Figure 2.12b**. Afterwards, Li et al. and Hu et al. expanded this manipulation to the interaction of both electric and magnetic field simultaneously by suspending iron nanoparticles in the LM.[146-147] Liu et al. further developed LM "mobiles" based on magnetic beads and LMDs.[148] These LM mobiles could move on a solid surface or in a water environment under the control of a magnet, as shown in **Figure 2.12c**. The micro-sized steel beads were controlled by a magnet to move towards an LMD on a sheet of paper, and suspended in the droplet once the beads reached the droplet boundary. Then, the LM droplet started to move subject to the magnetic field.
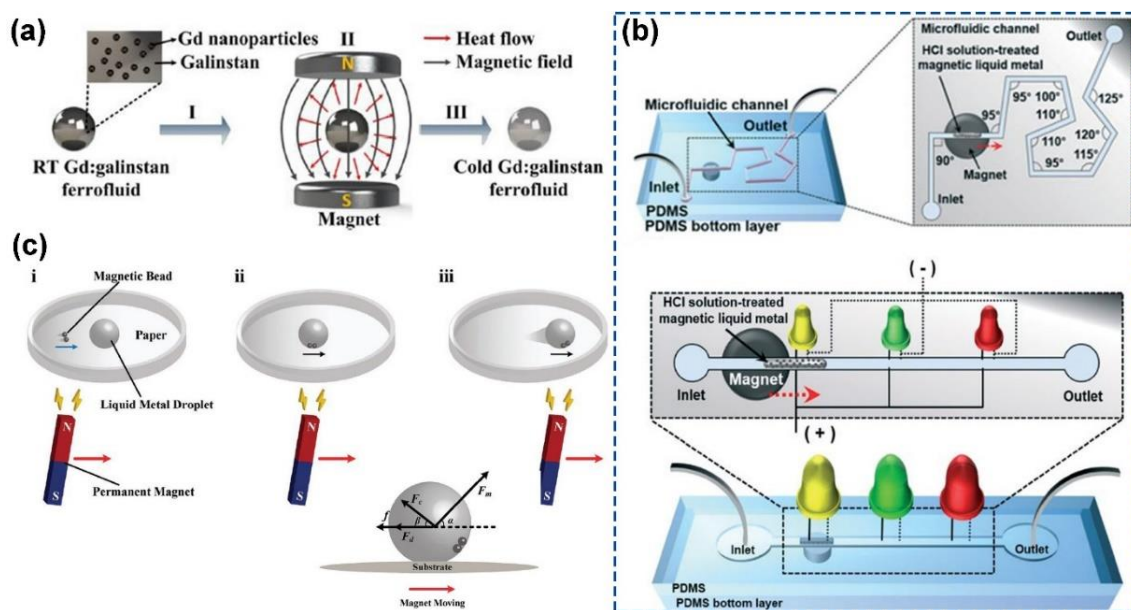
Figure 2.12. (a) Magnetocaloric ferrofluid formed by suspending gadolinium nanoparticles in the LM.[117] (b) Controllable locomotion of LM in complex microfluidic channels showing the ability to work as electrical switches.[145] (c) Controllable motion of LM mobiles on a solid surface.[148]

Moreover, the controllable motion under an external magnet enables various applications (e.g., in patterning or electronics) with modified properties (e.g., enhanced mechanical properties) for the magnetic LM.[24, 116, 118, 149-150] Ma et al. reported a simple, versatile, and equipment-free approach to direct patterning of an LM on various substrates using magnetic field. Ni microparticles were dispersed in the LM, forming a magnetic composite structure, through which the LM could directly write different patterns on various substrates.[24] Figure **2.13a** shows the directly patterning of LM on paper, PDMS, hydrogel, egg shell, and even on a glass vial. Ren et al. reported LM-based magnetoactive slurries formed by dispersing magnetic iron particles in LM matrix.[118] The mechanical properties, viscosity, and stiffness of such materials rapidly responded to the stimulus of an applied magnetic field. As shown in **Figure 2.13b**, a cylindrical slurry could support a weight of at least 50 g under an external magnet. When the magnet was moved, the

slurry fell and lost its enhanced stiffness. The mechanical properties of the slurry were attributed to the particle arrangement. The particles were initial formed random orientation, and then changed to chain or column structures, finally rigid chains. Then, Cao et al reported a novel ferromagnetic LM material with transformable shape and reconfigurable polarity by mixing neodymium–iron–boron (NdFeB) microparticles into an LM.[149] Unlike other magnetic composites, which would quickly lose the induced magnetization once the external magnetic field was removed, the LM/NdFeB composite could retain its induced magnetization. Moreover, the magnetic polarity of the composite was reconfigured, that is, the magnetic polarity could be reversibly disordered and rearranged for demagnetization and magnetization, which made the composite suitable for flexible erasable magnetic recording paper, as shown in **Figure 2.13c**. Furthermore, the magnetic LM was also used for electronics with soft substrates.[116, 150] Guo et al. developed a magnetic healing method based on Fe-doped LM conductive ink for flexible electronics, which included three parts of LM, degradable PVA substrate and adhesive fructose,[116] as shown in **Figure 2.13d**.
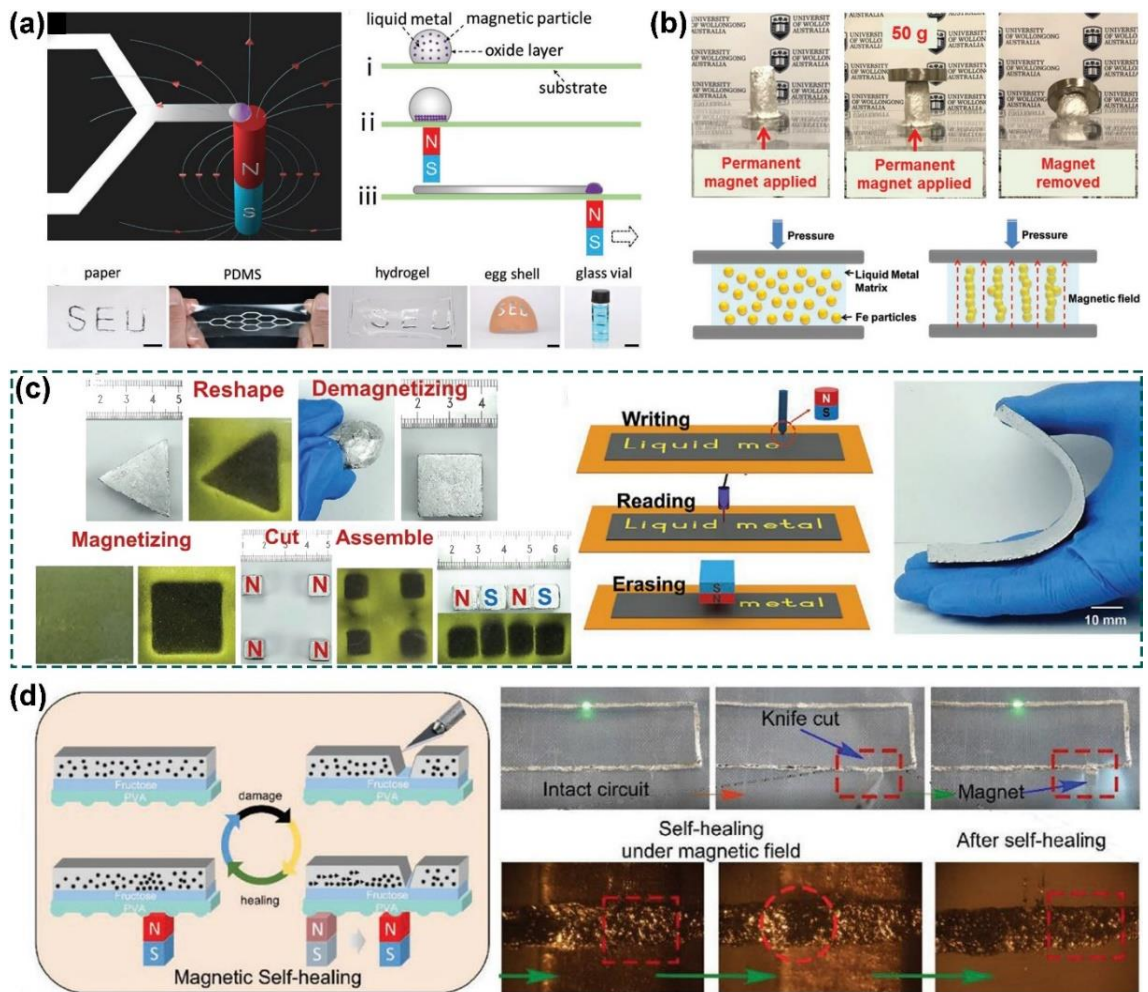
Figure 2.13. (a) Controllable direct patterning of LM on various substrates using magnetic field.[24] (b) Enhanced mechanical properties, viscosity, and stiffness of the LM-based magnetoactive slurries.[118] (c) Ferromagnetic LM material with transformable shape and reconfigurable polarity, which can used as flexible erasable magnetic recording paper.[149] (d) Magnetic healing method based on Fe-doped LM conductive ink for flexible electronics.[116]

In summary, research on the magnetic actuation of the LM/magnetic particle hybrids has mainly focus on two aspects: controllable movement and non-contact patterning. So far, the related research is attractive and shows great potential for practical usage. Some issues remain to be resolved, however, such as the precision for controllable movement

and patterning efficiency. Moreover, other magnetic related particles (i.e., paramagnetic or diamagnetic particles) hybrid with the LM for different magnetic actuation could be also explored.

2.5 Surface electrochemical manipulation of liquid metal

As mentioned above, a thin oxide layer will be formed when LM is exposed to an oxygen environment (i.e., ambient conditions).[14] This oxide layer can be removed with base (i.e., NaOH solution) and acid (i.e., HCl solution) solutions.[10] Moreover, Tang et al. found that the gallium dissolves slowly in NaOH solution and produce gallates $[Ga(OH)_4]^-$, and this $[Ga(OH)_4]^-$ layer will fill the surface of the LM with negatively charges while the outer layer is positivly charged, forming an electric double layer (EDL),[27-29] as shown in **Figure 2.14a**. In HCl electrolyte, however, the surface of the LM is positively charged (mainly Ga^{3+}) while the outer layer is negatively charged, also forming an EDL (opposite charge distribution in base and acid solution),[28-29] as shown in **Figure 2.14b**. The surface charge density of the EDL formed in acid solution is relatively low and Ga^{3+} is only generated at pH lower than 1.[151] Handschuh-Wang et al. introduced KI into an acidified solution to enhance the surface charge density of the EDL.[28] Based on the charge distribution of the EDL, when an electric field is applied, the LM droplets will move in the opposite direction depending on the electrolyte. The LM droplet moves towards the anode in NaOH solution, while it moves towards cathode in HCl solution, as in **Figure 2.14a&b**. The principle of motion can be attributed to the interfacial tension of the LM, which is influenced by surface charge distribution. The interface can be modelled as a parallel-plate capacitor, and the surface tension (γ) of the LM under applied voltage (V) can be described by the integrated Lippmann's equation as follows:

$$\gamma = \gamma_0 - \frac{c}{2}V^2 \tag{2-1}$$

where γ_0 is the maximum value of surface tension when $V = 0$, and C is the capacitance per unit area. The pressure difference (P) at the interface (LM-electrolyte) can be expressed by the Young-Laplace equation as follows:

$$P = \frac{2\gamma}{R}$$

(2-2)

Where R is the radius of the LM droplet. From **Figure 2.14a&b**, the charge will be redistributed under applied voltage, but the voltage drop across the EDL at the two sides of the LM droplet is different. This difference leads to the imbalance of surface tension, further resulting in a pressure difference (ΔP) between two sides, which is given as follows:

$$\Delta P = P_R - P_L = (\gamma_R - \gamma_L)\frac{2}{R} = \frac{C}{2}(V_L{}^2 - V_R{}^2)$$

(2-3)

Where P_R and P_L are the pressure difference, and V_R and V_L are the voltage drop across the EDL between the LM-electrolyte interface at the two sides. When the LM droplet is placed in NaOH solution (**Figure 2.14a**), the redistributed charge density is higher on the anode side, at which the voltage drop is higher ($V_R > V_L$). Thus, the pressure difference reaches its maximum on the left side end and is reduced towards the right side of the droplet. The pressure difference between the droplet and the medium produces counteracting forces of F_L and F_R on the droplet,[152] as shown in **Figure 2.14c**. F_L is larger due to the higher pressure generated at left side. As a result, the droplet is pushed towards the anode.[29, 152-153] Based on this hypothesis, Tang et al developed a liquid metal enabled pump for driving a range of liquids without mechanical moving parts with the application of a modest electric field,[152] as in **Figure 2.14d**. Afterwards, Zavabeti et al. developed another pump based on the ionic imbalance induced self-propulsion of the LMD induced by the ionic imbalance.[154] The LMD was placed in a spherical recess located in between two different flowing electrolytes of acidic and basic nature, and the ionic imbalance between the two hemispheres triggered the motion.

When the LM droplet is placed on a graphite surface in NaOH, however, the surface charge is altered from positive to negative,[26, 155-156] leading to a decrease in the surface tension and cathode-oriented motion, as shown in **Figure 2.14e**. Moreover, the opposite cathode-oriented motion is also observed when the LM droplet is placed in a closed system (i.e., a confined channel).[157-158] That is, the droplet moves to the cathode in NaOH solution, but such a cathode-oriented motion is different to the motion controlled by the graphite induced surface charge alteration. The motion in a closed system is probably due to the bipolarization of a droplet with a non-spherical shape (e.g., worm or elliptical shape). As in **Figure 2.14f**, the head of the elliptical-shaped droplet is the anodic pole (closer to the cathode), on which the oxide layer would be formed and decrease the surface tension at the head. Thus, according to the Marangoni effect, the surface oxide skin of the droplet will flow from the head to the tail (closer to the anode), while the inner liquid part flows towards the head, pushing the LM droplet to move to the cathode. Based on this effect, Wu et al. fabricated a wheeled robot driven by a LM droplet,[158] as shown in **Figure 2.14g**. The droplet moves to the cathode and it thus pulls the wheeled robot to move forward.
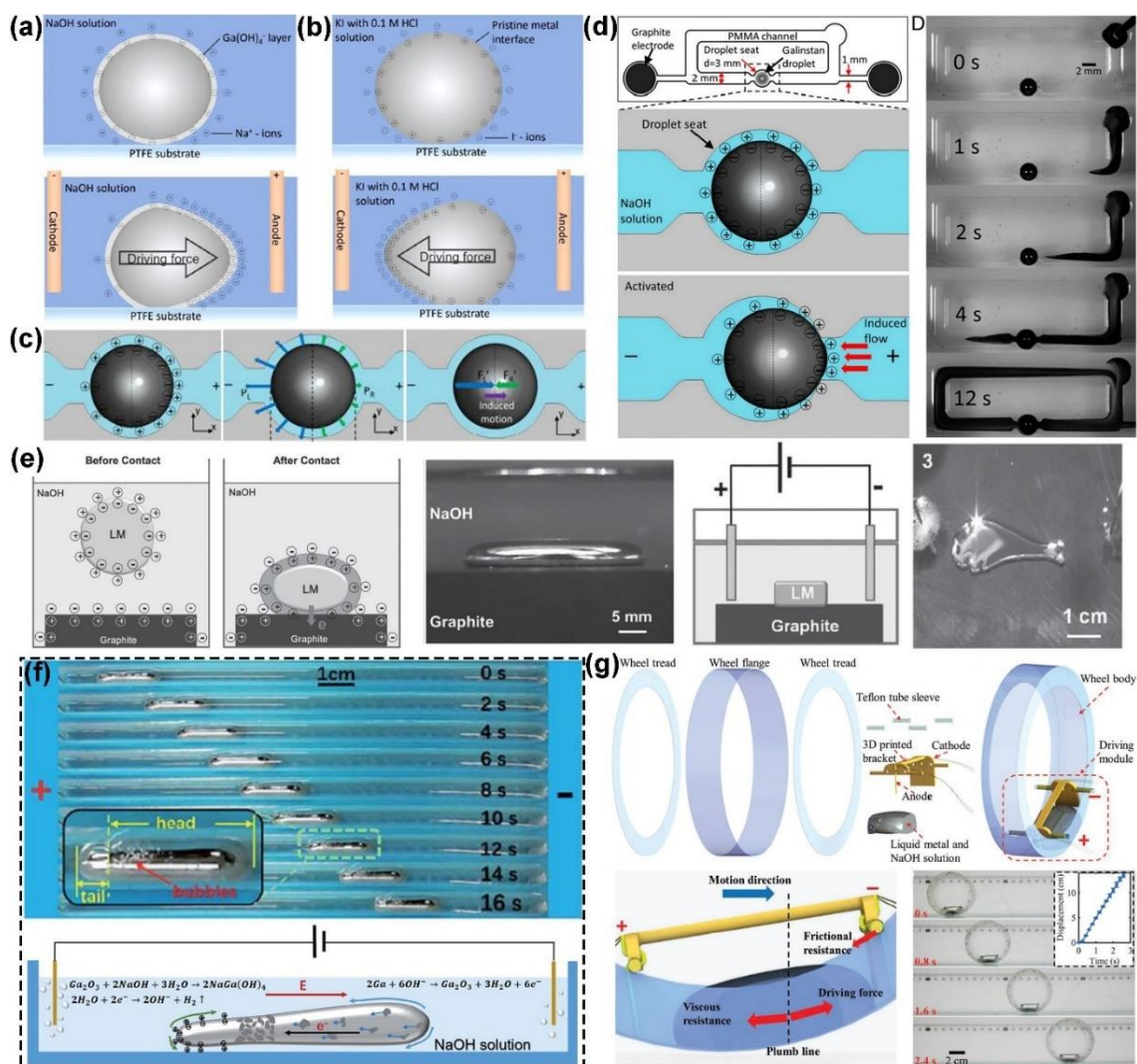
Figure 2.14. Surface charges and induced motion under external electric field. (a) In a base solution.[28] (b) In an acid solution.[28] (c) The principle of motion.[152] (d) A liquid metal enabled pump for driving a range of liquids.[152] (e) Graphite induced surface charge alteration and a cathode-oriented motion in NaOH solution.[26] (f) The bipolarization induced cathode-oriented motion in NaOH solution for a closed system.[157] (g) A wheeled robot driven by an LM droplet.[158]

Besides the electric-field-controlled surface electrochemical manipulation of the surface charge distribution, by which the motion of the LM droplet is controllable in the presence of an electric field, other methods have also been investigated to change the

surface state and control the motion of the LM droplet in the absence of the electric field. Zhang et al. found that some metal-LM composite structures are also capable of altering the surface charge distribution, as well as the electron migration. As mentioned above (composite structures of LM), they proposed synthetic self-fueled motors based on LM-Al composites, the driving force of which is generated from unbalanced bipolar electrochemical reaction.[119] As shown in **Figure 2.15a**, the Al-LM system forms a galvanic cell, in which Al is the cathode and LM acts as the anode. When Al is dissolved in NaOH solution, the electrons flow internally from Al to LM, which alters the distribution of surface charges, thus leading to the imbalance of the surface tension. Finally, the imbalanced state induces a pressure difference at the two ends, pushing the motor to move towards the LM end. Sheng et al. expanded this LM-motor to construct a transient state machine enabled by the colliding and coalescence of LM-Al motors.[159] Moreover, asymmetric surface wetting was also employed for controllable motion of the LM droplet. Mohammed et al. has described a method to spontaneously accelerate LMDs by placing the droplet along predefined metallic paths.[160] As shown in **Figure 2.15b**, the LM-Ag film works as a bipolar electrode, where oxidation of gallium occurs on the surface of the LM (cathode) and reduction of water occurs on the surface of the Ag (anode). Thus, the electrons migrate from the LM to the Ag film. This electrochemical reaction induced an imbalance at the two ends of the droplet, pushing the droplet to move forward. Moreover, based on the theory of asymmetric surface wetting, that is, the different contact angles on the two sides of the droplet, the difference between the forward and the backward force generates a net force as follows:

$$F_{net} = F_F - F_B \sim \gamma(cos\theta_F - cos\theta_B) \qquad (2\text{-}4)$$

where F_F and F_B are the forward and backward forces, and θ_F and θ_B are the corresponding contact angles, respectively. For the LM droplet on glass substrate, the

contact angles on both sides of the droplet were the same (no wetting). Although the Ag film in contact with the droplet on the forward side does contribute to the net force (**Figure 2.15c**). Based on this concept, Yuan et al developed an LM-machine-triggered violin-like wire oscillator.[161] A copper wire inserted inside the LM droplet (containing Al granules) oscillates horizontally from side to side. The underlying mechanism is the asymmetric surface wetting induced by the different contact angles at the two sides of the droplet, which provides the driving force, as in **Figure 2.15d**. Ma et al. also realized reactive wetting, coating, and spreading of the LM within porous copper.[162] The LM even spread toward the cathode in NaOH solution due to the asymmetric surface wetting effect, as shown in **Figure 2.15e**.

Figure 2.15. Surface charges and induced motion via the surface electrochemical reaction. (a) LM-Al composite structure for altering the surface charge distribution.[119] (b-e) Asymmetric surface wetting effect for motion control: (b) LM-Ag film,[160] (c) induced

net force,[160] (d) LM/Al-copper wire,[161] (e) LM-porous copper.[162]

Moreover, Dickey's team found that when the LM droplet was connected to electrodes, unexpected novel phenomena were observed.[10, 25] As shown in **Figure 2.16a**, the anode is inserted into a LM droplet, and the droplet spreads dramatically in NaOH solution under modest voltages, which should be attributed to the formation of the oxide layer on the surface of the LMD over a critical voltage.[10] Below this critical voltage, the droplet adopts equilibrium shapes, forming the EDL on the surface. Once the oxide layer is formed, the surface tension of the droplet decreases significantly (**Figure 2.16a**), leading to the deformation and spreading of the LMD. This oxide surface also enables a new class of fingering instabilities with a measured fractal dimension value of 1.3 ± 0.05.[163] Moreover, the LMD could deform and move towards the cathode simultaneously in a confined space, as shown in **Figure 2.16b**. Yu et al. realized the simultaneous deformation and solidification of the LM by inserting a gallium wetted anode into the LM,[164] which offers a new approach to controlled patterning structures, as shown in **Figure 2.16c**. Moreover, applying a reductive potential to the metal removes the oxide layer in the presence of electrolyte, which will induce capillary behavior ('recapillarity'),[8, 10] as shown in **Figure 2.16d**. By taking advantage of the surface oxide layer, Yu et al. proposed a non-contact, maskless lithography method for LM,[165] and various patterns can be simply and rapidly fabricated via this method, as shown in **Figure 2.16e**. They also discovered a voltage-stimulated heartbeat effect of the LMD by taking advantage of the imbalance between the surface tension and gravity of the LM,[166] as shown in **Figure 2.16f**. A novel circular graphite electrode was inclined at an angle (0.5°), creating a decreasing trend for LM. While the oxide layer was formed (decreasing the surface tension) when the LM came into contact with the graphite electrode, it dissolved in NaOH electrolyte (increasing the

surface tension) when the LM was disconnected with the electrode. Altering surface tension and the gravitational force triggers the heartbeat effect. To date, this oxidation strongly depends on the value of the external voltage and the concentration of the electrolyte. That is, in the presence of acidic/basic electrolyte, the formation and dissolution of the oxide layer is dynamic. Larger voltages increase the oxidation rate, while a higher concentration electrolyte accelerates the dissolve rate. An appropriate dynamic process for the oxidation and dissolution of oxide layer can also cause the LM to flow as a fiber as it is extruded from a syringe,[11, 56] but coalesces or separates into LMDs when the voltages is altered.[167]
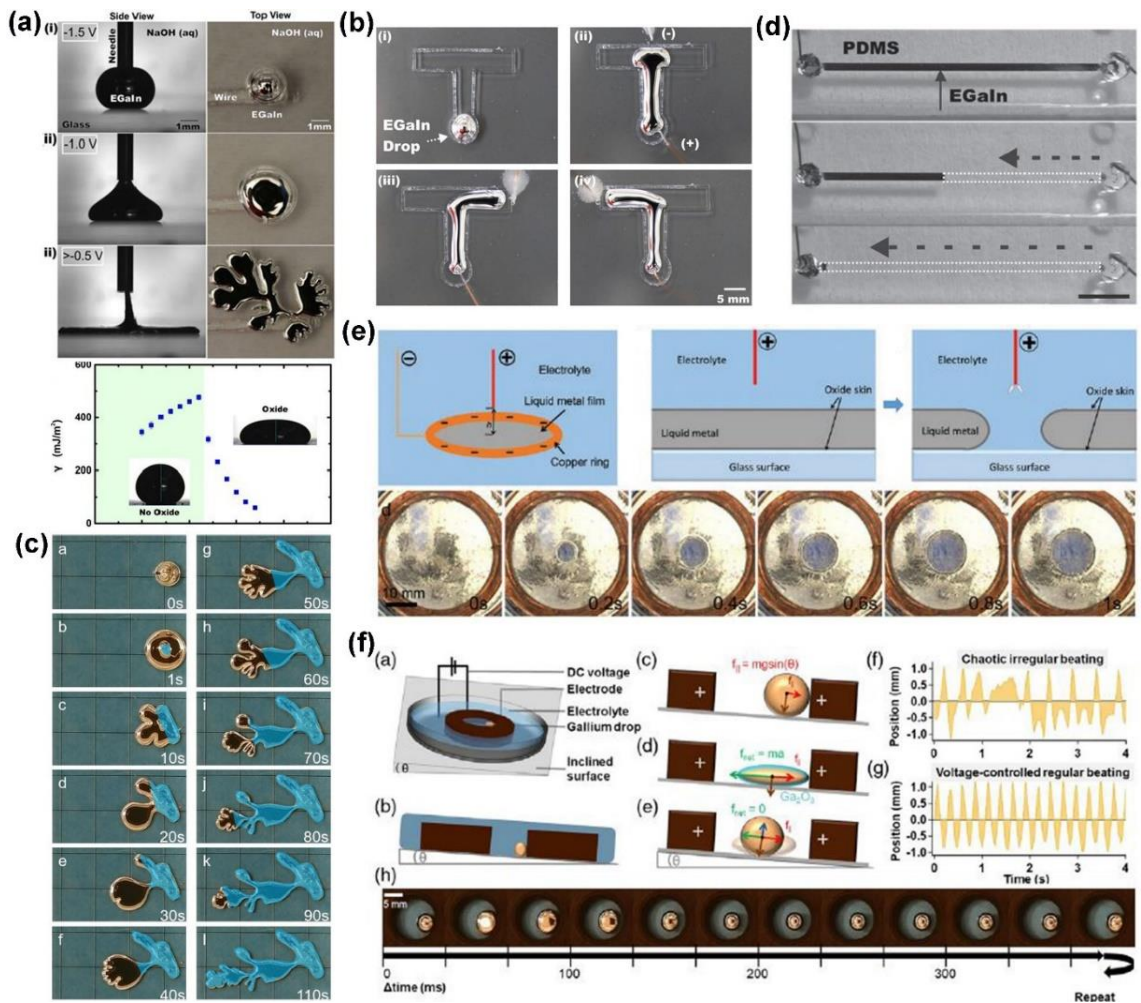
Figure 2.16. Surface oxidation induced novel phenomena and applications of the LM. (a)

Deformation of LM induced by surface oxide layer.[10] (b) The LM deforms and moves to the cathode in a confined channel.[10] (c) Simultaneous deformation and solidification of the LM.[164] (d) 'Recapillarity' effect of the LM under a reductive voltage.[8] (e) Non-contact, maskless lithography method for the LM.[165] (f) Voltage-stimulated heartbeat effect of the LMD.[166]

It can be concluded that the electrochemical manipulation of the LM is controlled by the charge distribution of the surface of the LM, which is realized by applying an electric field or adding some metallic particles onto the LM. Then, the surface tension becomes different at the two ends of the LM, leading its controllable motion of the LM. Although various efforts have been made to control this manipulation, there is still much that remains unsolved, such as the underlying mechanism of deformation, and there needs to be new exploration for novel phenomena and applications.

2.6 Electrical current of electrochemically manipulated liquid metal

As aforementioned, the electrochemical oxidation of the surface of the LM metal in basic/ acid solution lowers the effective surface tension of the LM to extremely low values (~ 10^{-5} mN/m),[10] and an electric current will be generated from the electrochemical oxidation at the same time: $Ga \rightarrow Ga^{3+} + 3e^-$. Few reports, however, have systematical measured the currents of LMs with different morphologies, nor related the change in current to oxidation/dissolution of LM, as well as to the change in interfacial tension.

Zhang et al. studied the controllable large-scale reversible deformation of an LM. They measured the current relative to the electric potential and concentration of the NaOH solution. A larger electric potential and higher concentration of the NaOH solution both increase the current of the deformed LM,[25] as shown in **Figure 2.17a**. Zhang et al.,

however, focused on the deformation phenomena by reporting the influence of the electric potential and concentration of the NaOH solution on the deformation size of the LM, instead of connecting the electrical current to the surface state of the LM. Then, Song et al. reported the current change during the morphological transitions of the LM under different electric potentials.[11] The LM transformed from drops to connected drops and finally to wires as the electric potential increased from 0.2 to 2 V. The corresponding current of the LM increased from near-zero to a significant value (~ 150 mA), as shown in **Figure 2.17b**. They linked the electrical current to surface oxidation and showed that the surface oxidation lowered the interfacial tension and formed various morphologies. Moreover, Wissman et al. demonstrated a novel approach to coalesce and separate droplets by modifying the interfacial tension under electrochemical manipulation.[167] As in **Figure 2.17c**, they applied a current across the LM droplet from two outer electrodes. Thus, oxidation and reduction occurred on the anodic and cathodic poles of the droplets, respectively. The interfacial tension decreased due to the surface oxidation at the anodic side while the interfacial tension remained at its maximum value due to the surface reduction on the cathodic side, leading to gradients in interfacial tension. The gradients finally separated the two droplets once the applied current was over a critical value. They took advantage of the current to alter the interfacial tension of the LM droplets and realized a field-controlled electrical switch with the LM. Yet, the underlying mechanism and quantitative expression between the electrical current and the oxide surface remained unknown.
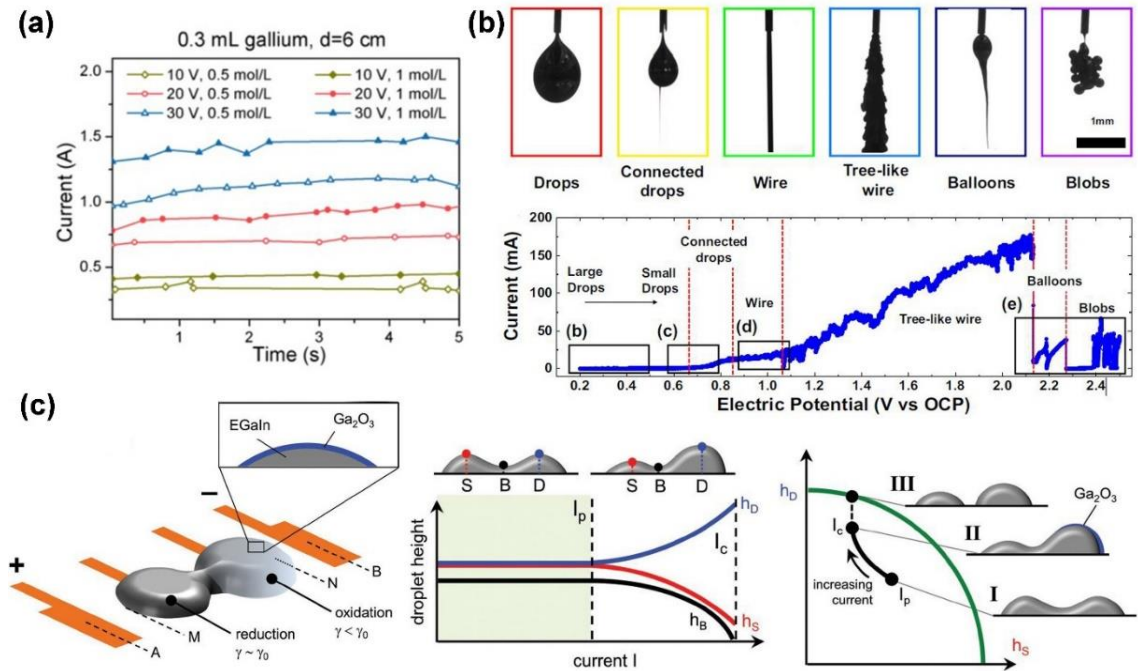
Figure 2.17. (a) The electrical current of the LM droplet relative to the electric potential and concentration of the NaOH solution.[25] (b) The current changes during the morphological transitions of the LM under different electric potentials.[11] (c) Electrochemically manipulated gradients in interfacial tension to separate the LM droplets.[167]

2.7 Electromagnetic interaction of liquid metal

The concept of electromagnetic interaction of an LM was first realized with an external electric current in/around the LM. Lohöfer et al. proposed a new device for the inductive measurement of electrical resistivity and the density of LMs and semiconductors, based on two electromagnetic levitation facilities operating under microgravity.[168] As shown in **Figure 2.18a**, electromagnetic levitation uses a high frequency alternating magnetic field $\mathbf{B}(t) = \mathbf{B}_0 \sin(wt)$ generated by an alternating current carrying coil windings for the containerless lifting and heating of metallic melts. The magnetic field induces eddy currents in the LMD, generating a Lorentz force perpendicular to both the current and the field, and the Lorentz force lifts the LMD. Moreover, Fisher et al. realized a hydraulic

74

jump for liquid metal in channel flow under the Lorentz force, giving insight into the hydraulic jump behavior in the presence of magnetic fields and electrical currents.[169] **Figure 2.18b** shows that the Lorentz force may be generated to control the liquid metal jump behavior by using externally injected electrical currents (up to 140 A) and a magnetic field. This hydraulic jump is repeatable and predictable, so that it can be used for liquid metal control within next-generation fusion reactors. This external electrical-current-assisted electromagnetic manipulation of LM has many limitations, however, such as severe exothermic phenomena due to the large current (so that cooling system is always needed).
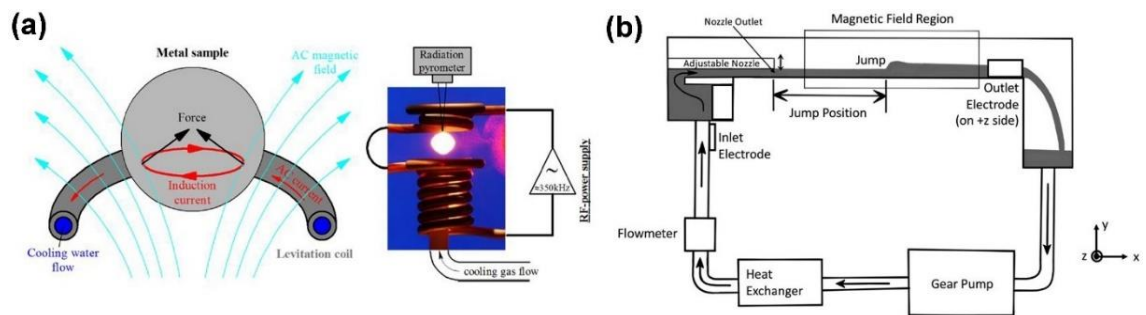
Figure 2.18. External electrical-current-assisted electromagnetic manipulation of LM. (a) Electromagnetic levitation of LM.[168] (b) Jumping behavior of LM.[169]

Moreover, rotating magnetic fields (RMFs) are also applied to induce current within the LM, thereby realizing its electromagnetic manipulation. Shu et al. introduced an innovative method for controlling the motion of liquid metal droplets using the Lorentz force induced by magnetic fields.[170] **Figure 2.19a** shows the mechanism and behavior of the actuation of a liquid metal droplet. An eddy current will be induced within the liquid metal in the rotating magnetic field, and this current generates a horizontal Lorentz force to drive the motion of the liquid metal droplet. Afterwards, Zhao et al. reported a non-coalescent phenomenon of an LM droplet sustained on an LM bath surface, with a RMF

exerted on the LM bath.[171] As shown in **Figure 2.19b**. The magnetic field induces a current in the LM bath, generating a Lorentz force driving the LM to flow in the direction of the RMF. Then, an LM droplet was placed on the LM bath surface, and the LM droplet could move on the surface for a certain time before coalescence.
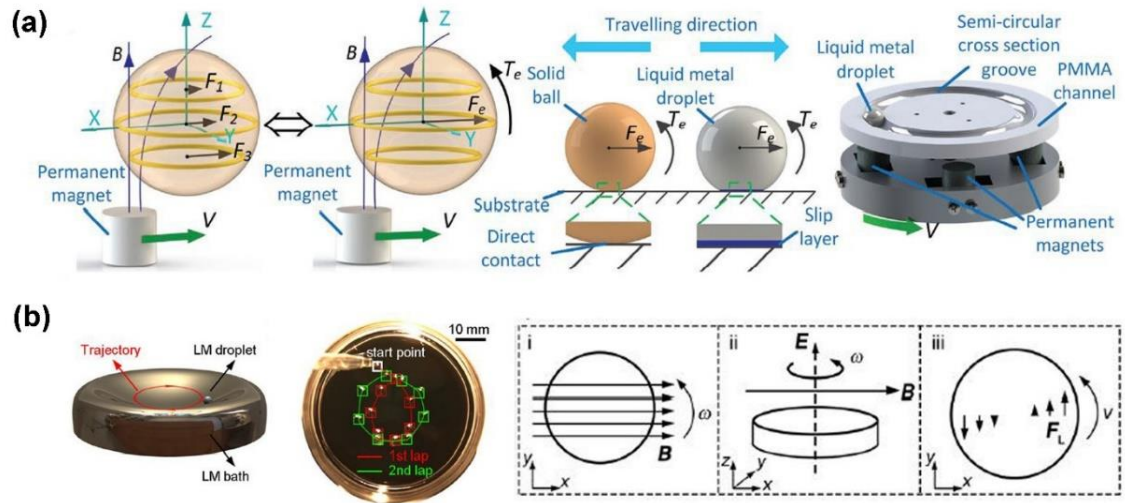
Figure 2.19. Rotating-magnetic-field assisted electromagnetic manipulation of LM. (a) Controllable locomotion of LM.[170] (b) Non-coalescent phenomenon of LM droplet sustained on LM bath surface.[171]

As mentioned above, an electric current will be generated from the electrochemical reaction (surface oxidation of the LM in electrolyte with a modest external voltage). Although normally an LM is not responsive to magnetic fields, a current passing through the LM to drive the electrochemical reactions makes it susceptible to magnetic forces *via* the Lorentz force. The displacement of the LM relative to the magnet field will induce a secondary force according to Lenz's law (i.e., a drag force that opposes the motion at the periphery of the magnet), through which the simultaneous deformation and electromagnetic manipulation of the LM could be realized, enabling new strategies for shaping electronically conductive fluids for advanced manufacturing and dynamic

electronic structures. These potential applications are underestimated, however, and there are only few papers that have reported this novel electromagnetic interaction phenomenon. Tan et al. reported a phenomenon in which the magnetic field can make up a boundary to restrict motion of an aluminum-powered liquid metal motor.[172] An electrical current was generated in the LM droplet due to the electrochemical reaction, and this induced the Lorentz force in the presence of a magnetic field. Owing to the Lorentz force, a high magnetic field would break up the directional running of the motor. **Figure 2.20a** shows that the numbers of motors in different regions vary with time. Most motors just gather near the boundary of the magnet. Based on this manipulation, Wang et al. realized electromagnetic rotation of the LM by using a pair of concentric-ring graphite electrodes and a magnetic field,[30] as in **Figure 2.20b**. The LM could move along the concentric ring channel with controllable speed. Moreover, they found that symmetrical folding patterns were induced on the LM surface when the LM filled the channel.[173] In the presence of the magnetic field, the LM rotated around the inner electrode with changing patterns. And these patterns of axisymmetric morphology appeared randomly, as shown in **Figure 2.20c**.
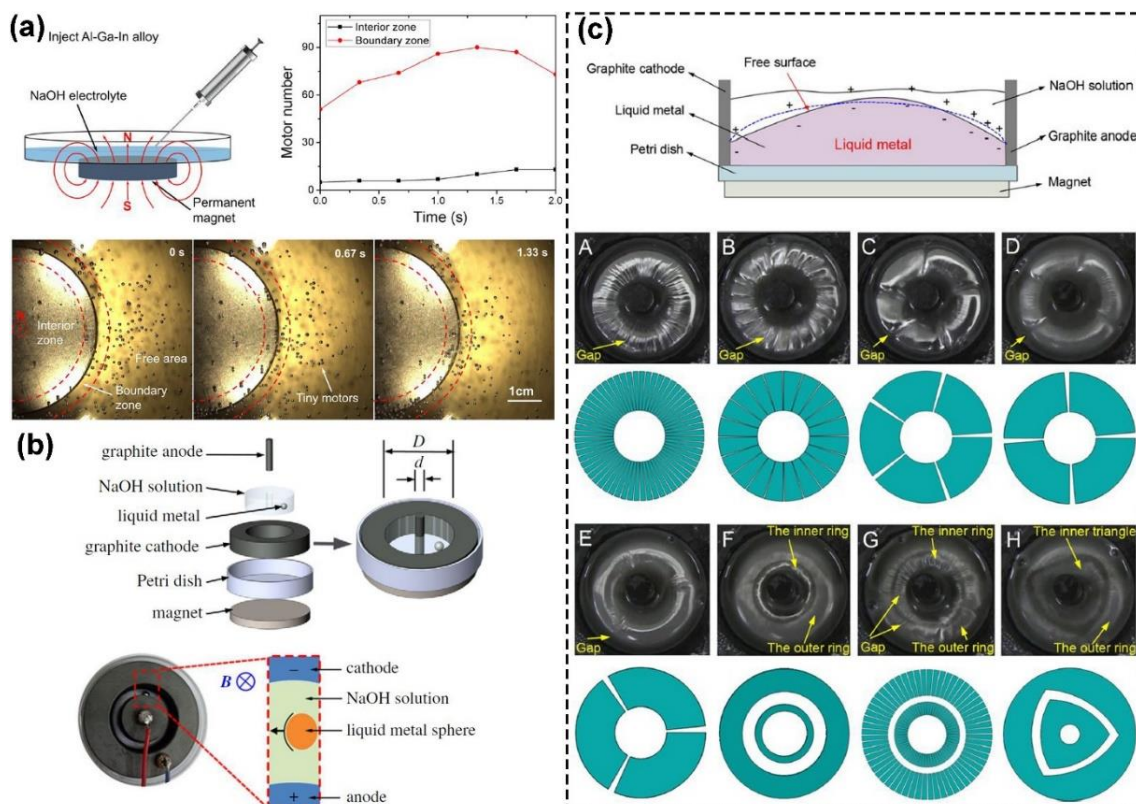
Figure 2.20. Electrochemical-reaction-assisted simultaneous deformation and electromagnetic manipulation of an LM. (a) Magnetic field boundary of an aluminum powered LM motor.[172] (b) Rotation of the LM along a concentric ring channel with controllable speed[30] and (c) with changing patterns.[173]

In summary, there are three ways to realize the electromagnetic manipulation of an LM: 1) a large external current (up to 140 A) with magnetic field, 2) a moving magnetic field (e.g., a rotating magnet), and 3) electrochemical oxidation (a modest voltage about few volts) with magnetic field. Considering the diverse deformation (e.g., directional motion and heart beating effects) of the LM under a modest voltage, the electromagnetic manipulation for case 3 has enormous potential for applications, such as patterning metallic shapes, which may reveal some unexpected phenomena at the same time.

Chapter 3. Experiments

3.1 Introduction

This chapter describes the experimental details of this doctoral thesis, which includes experimental preparation for each work and experimental instruments used in data collection. The experimental instruments shown here were only for observation, measurement, and data collection/transport/export of research. Some facilities for common data analysis methods (such as graphic drawing software) are not included.

3.2 Experimental preparation

3.2.1 Experimental setup for screening effect of liquid metal droplets

The LMDs are immersed in NaOH solution in a horizontal petri dish with anode attached. The experiments were conducted by using one LMD 1 cm in size. Different distances between the LMD and the cathode, as well as various external voltages are applied to investigate the deformation of LMD under different voltages and electric fields. The experiments are conducted under relatively low voltage from 3 to 10.5 V, with the distance varying from 2 to 7 cm.

3.2.2 Experimental setup for heart beating effect of liquid metal droplet

The LMD is immersed in NaOH solution in a horizontal petri dish, confined by an insulator. The anode is attached to the top of the LMD, while the cathode is placed in NaOH solution with a distance of 5 cm between the electrodes. Periodic beating of the LMD is observed under external voltage of 1.5 V. When the anode touches with the LMD, the LMD moves downward and leaves the anode instead of merging the anode. Then, the LMD moves back to its initial position and comes into contact the anode, creating the periodic beating. The initial diameter of the LMDs varies from 8 to 14 mm, and the anode

is placed at different positions downward from 0 to -3.5 mm with fixed position of the LMD.

3.2.3 Experimental setup for non-contact manipulation of liquid metal wire

The LM is first immersed in 1 mol/L NaOH solution to dissolve any oxide species. The LM is aspirated into a syringe (diameter of 0.26 mm) and pumped at a volumetric flow rate controlled by a syringe pump. Electrodes attached to the syringe needle applied 1.5 V to the metal relative to a negative graphite electrode. This potential was empirically chosen because it results in the formation of wires as the liquid metal exits the syringe needle. These fluidic streams are regarded as LM wires that offer metallic conductivity, and have narrow diameters (100 ~ 200 μm). The experiments proceeded in a 1 mol/L NaOH solution inside a plastic vessel. The syringe remained immersed in the solution close to the vessel wall to be in proximity to an external magnet flush with the exterior wall. The vertical position (P_M) of the magnet was defined relative to the fixed position of the needle orifice. That is, when $P_M = 0$, the center of the magnet is at the same vertical height as the orifice.

3.3 Experimental equipment

3.3.1 Contact angle stage

The contact angle stage is an ideal platform for observation of liquid motion, as well as the detailed state at the interface for multi-liquids. As shown in **Figure 3.1**, the video-based optical contact angle measurement instrument (OCA-15EC) consists of a linear stage, charged coupled device (CCD) video camera, and the electronic dosing system (pump and needle base). During the experiments, the liquid metal is pumped from the needle, and the motion on the substrate on the stage is recorded by the CCD camera
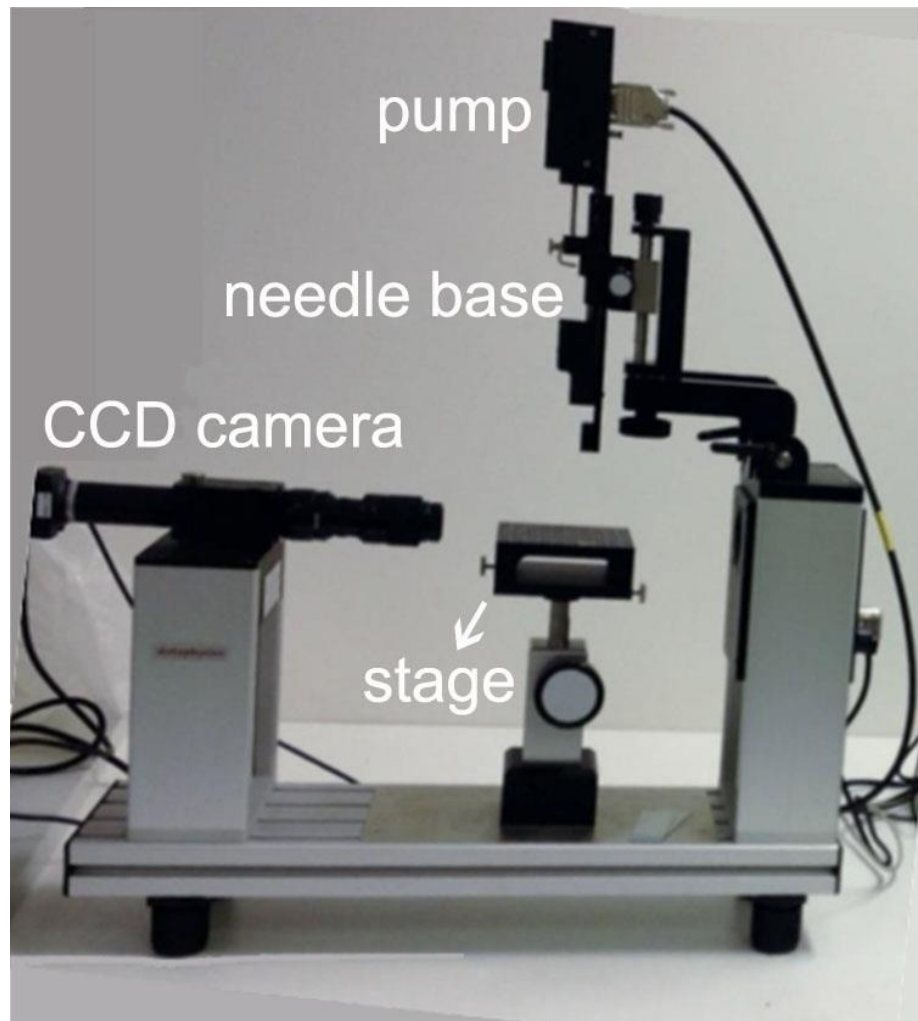
system.

Figure 3.1. The OCA-15EC contact angle instrument from DataPhysics, Germany. The liquid metal is pumped from the needle, and the motion on the substrate on the stage is recorded by the CCD camera system.

3.3.2 Electrical measurement system

The electrical measurements system includes two parts, a digital multimeter (DMM) and the Labview platform, as shown in **Figure 3.2**. Two DMMs (Keithley 2002 and 6514) are used to collect electrical data, including the voltage, resistance, and electrical current. Then, the collected data is transported to a programmed Labview

platform for visual graphics and data export.
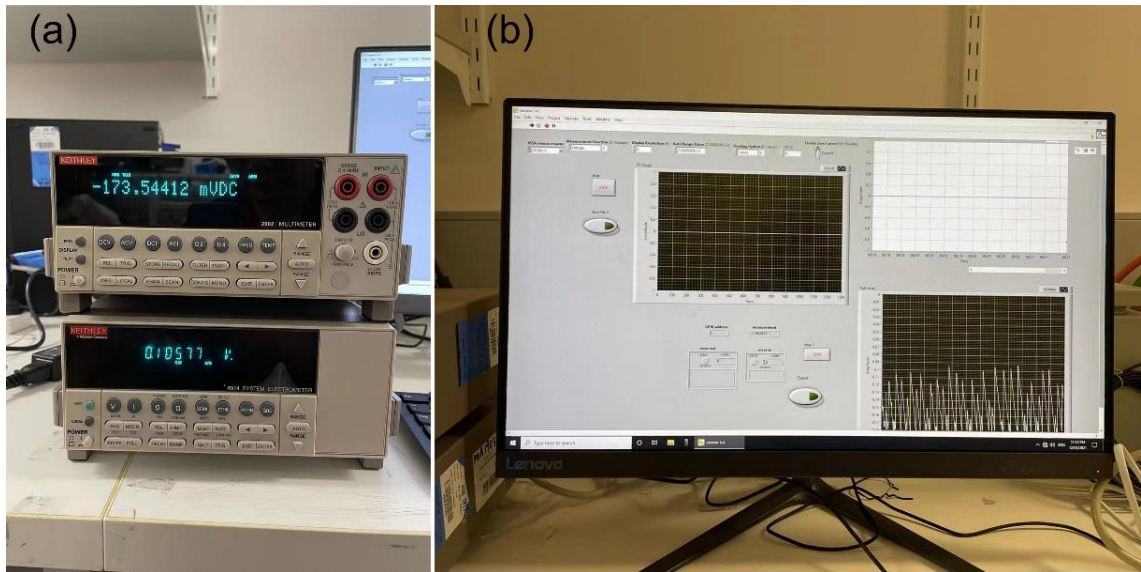
Figure 3.2. Electrical measurement system includes two parts: (a) digital multimeter and (b) the Labview platform.

3.3.3 3D printer

3D Printing is the process of continuously adding layers of material with a computer-controlled device to create a three-dimensional object. The simple equipped 3D printer used in this work consists of a 3-axial stage and a motor. The raw materials are driven by the motor, which is controlled by a specially designed program on the computer. In this thesis, some plastic parts were fabricated using this printer, as shown in **Figure 3.3**.
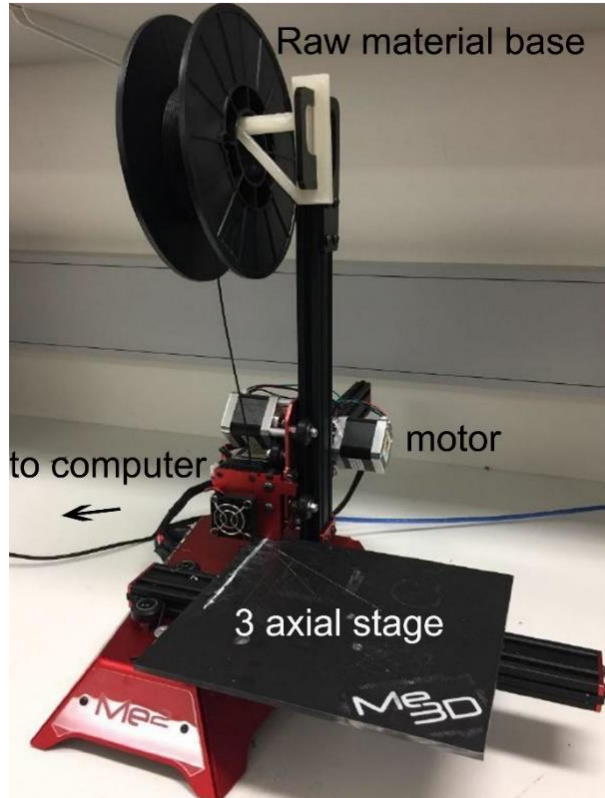
Figure 3.3. Me3D (Australia) 3D printer consists of a 3-axial stage and motor. The raw materials are driven by the motor which is controlled by a specially designed program on the computer.

Chapter 4. Non-Contact Rotation, Levitation, and

Acceleration of Flowing Liquid Metal Wires

4.1 Abstract

This work reports the non-contact manipulation of freefalling cylindrical streams of liquid metals into unique shapes such as levitated loops and squares, it is published in the journal of Proceedings of the National Academy of Sciences of the United States of America (*PNAS*). Such cylindrical streams form in aqueous media by electrochemically lowering the interfacial tension. The electrochemical reactions require an electrical current that flows through the streams, making them susceptible to Lorentz forces. Consequently, varying the position and shape of a magnetic field relative to the stream controls these forces. Moreover, the movement of the metal stream relative to the magnetic field, induces significant forces arising from Lenz's law that causes the manipulated streams to levitate in unique shapes. The ability to control streams of liquid metals in a non-contact manner will enable new strategies for shaping electronically conductive fluids for advanced manufacturing and dynamic electronic structures.

4.2 Importance and Implementation of Non-contact Manipulation

Non-contact methods of manufacturing and manipulation can minimize disturbing objects of interest. Objects can be manipulated in a non-contact manner by magnetic methods (levitation and tweezers),[174-175] acoustic manipulation,[176-177] optical tweezers,[178] and other techniques.[179-180] However to date, free-flowing liquid streams have been particularly difficult to manipulate in a non-contact manner. Realizing highly controlled changes in directionality or complex shaping of liquids, especially without disrupting the cross-sectional shape of the stream, is a challenge. Here, the non-contact manipulation of free-flowing streams of liquid metals (LMs) was explored. Gallium-based liquid metals

(Galinstan, the eutectic alloy of gallium indium and tin used in this work) have recently received significant attention due to their promises as soft and stretchable metallic conductors, low melting points, simultaneous fluidity and metallic properties at room temperature, as well as the low toxicity.[2-4, 6-9]

Liquid metal alloys are seemingly unlikely candidates to form stable fluid streams due to their enormous surface tension and water-like viscosity, which favor the formation of droplets (see **Figure 6.1a**). However, electrochemical oxidation of the surface of the LM metal in basic solution lowers the effective tension of the LM to extremely low values.[10-11] This electrochemical manipulation of interfacial tension enables various fascinating phenomena, such as reversible deformation,[164] patterning,[165] heartbeat effects,[166] 'superfluid-like' penetration through porous media,[181] and other electrochemical effects.[14, 127, 163, 182] Most importantly, the presence of oxide species on the LM also enables long, stable wire-like streams of metal to form as it exits a nozzle into the solution (see **Figure 6.1b**). Because of their cylindrical cross-section and metallic conductivity, these fluidic streams are called as LM wires (LMWs), which form narrow diameters (100 ~ 200 μm). Although normally LM is not responsive to magnetic fields, the current passing through the wire to drive the electrochemical reactions makes it susceptible to magnetic forces *via* the Lorentz force (see **Figure 6.1c**). That is, a magnetic field applied normal to electrical current generates a force normal to both the current and magnetic field.

In this work, the displacement of free falling LMWs at room temperature is controlled by using the Lorentz force. Because LM is soft, it provides almost no resistance to manipulation *via* the Lorentz force and therefore accelerates radially. The displacement of the LMWs relative to the magnet also induces a secondary force according to Lenz's law (i.e., a drag force that opposes the motion at the periphery of the magnet). Thus, the

combination effects of the Lorentz force and Lenz's law drive the metal into shapes that mirror the circumference of the magnet while levitating the metal. As shown here, the behavior depends on the location of the magnet relative to the liquid metal wire. The unique ability to manipulate LM streams in a non-contact manner by using only a relatively low applied voltage and a common magnet is demonstrated and characterized.

4.3 Results and Discussion of Underlying Mechanism

The LM was firstly immersed in 1 mol/L NaOH solution to dissolve any oxide species. The LM was aspirated into a syringe (diameter of 0.26 mm) and pumped it at a volumetric flow rate (VR) controlled by a syringe pump. Electrodes attached to the syringe needle applied 1.5 V to the metal relative to a negative graphite electrode. This potential is empirically chosen because it resulted in the formation of wires as the liquid metal exits the syringe needle. These fluidic streams are regarded as LM wires (LMW) that offer metallic conductivity, and narrow diameters (100 ~ 200 μm). The experiments proceeded in a 1 mol/L NaOH solution inside a plastic vessel, as illustrated in **Figure 4.1d**. The syringe remained immersed in the solution close to the vessel wall to be in proximity to an external magnet flush with the exterior wall. The vertical position (P_M) of the magnet was defined relative to the fixed position of the needle orifice. That is, when $P_M = 0$, the center of the magnet is at the same vertical height as the orifice. To vary the Lorentz force, the magnet is moved by P_M from +3 to -3 cm (positive values indicate the magnet is in an elevated position relative to the orifice). The N pole of the magnet (0.1 T) faced the needle of the syringe. **Figure 4.1e** shows the results of the LMWs' motion at a flow rate of 2 μl/s when the P_M was changed from +3 to -3 cm with an interval of 1 cm. The dotted square box represents the location and shape of the magnet.

A video camera recorded the trajectories of the LMWs as a function of magnet position. When the magnet is centered with the needle outlet ($P_M = 0$), the LM experiences approximately uniform magnetic field lines. Consequently, the metal stream moves in a circular pattern driven by the Lorentz force. However, for high P_M (+3 and +2 cm) or low P_M (-2 cm or -3 cm), the LM stream experiences 'fringe' (i.e., diverging) field lines from the off-centered magnet. Consequently, the LMWs move in a spiral shape. The circular motion of the LMWs occurred for the P_M between +1 and -1 cm, while the spiral motions occurred for other positions.

A force analysis helps to explain these trajectories. The Lorentz force on the LMW at $P_M = 0$ cm is taken as an example to illustrate how the Lorentz force governs the motion of the LMW together with Lenz's law force. The metal wire, which would normally travel in a straight downward path due to gravity, instead spirals radially outward due to the presence of the magnet. **Figure 4.1f** shows four typical sequences of frames of the temporal evolution of the spiral. The LMWs should be subjected to three primary forces: gravity (G), Lorentz force (F_L), and Lenz's law force (F_{Lenz}). Viscous drag is neglected as it only dissipates energy, resulting from the motion of the LMW and does not dictate the path of the metal electromagnetically. Interfacial tension is also neglected since it is near-zero and presumably uniform along the wire. G accelerates the LMW downward. F_{Lenz} is the drag force induced by changes in the magnetic flux as the metal wire moves away from (or towards) the magnet. The Lorentz force, defined by the formula: $F_L = B \cdot I \cdot L$ (B is magnetic field intensity, I current and L the length of LMW), is the only force that causes the liquid metal stream to deviate from its straight, downward path as it exits the nozzle. The direction of the Lorentz force is normal to both the direction of current through the wire and the magnetic field from the magnet. In other words, it directs the liquid metal stream outwards in a clockwise pattern.
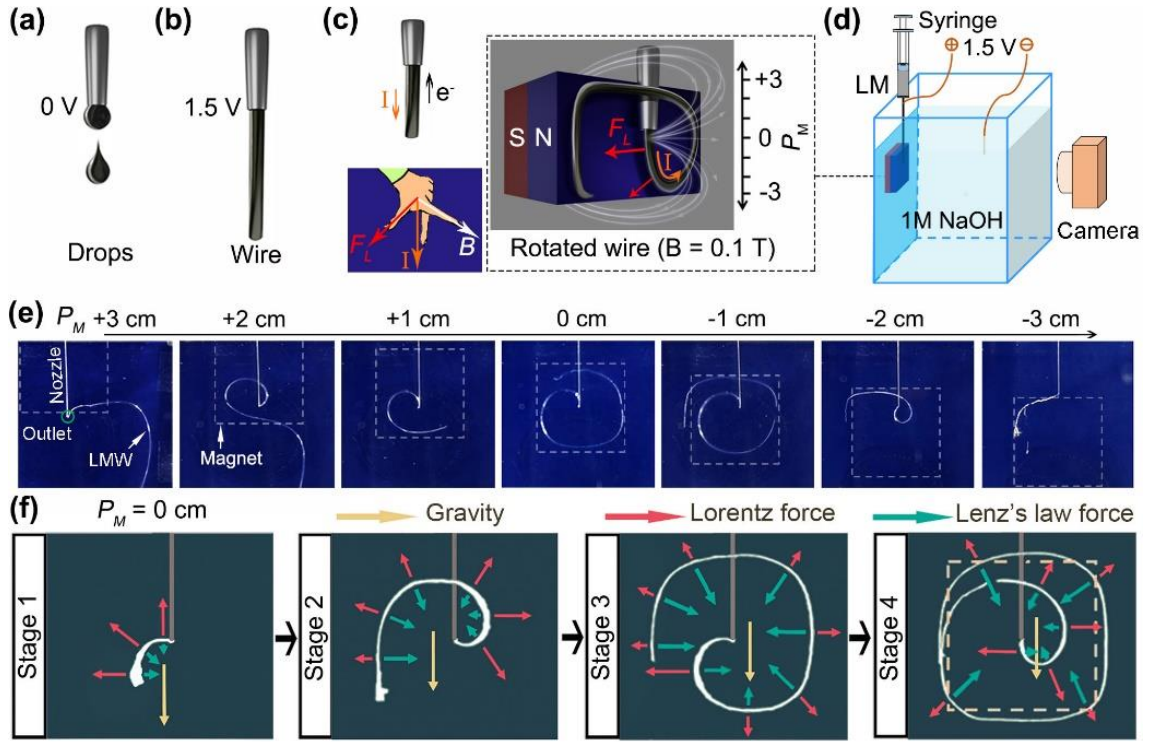
Figure 4.1. Liquid metal morphologies under different electric potential, (a) Droplets, 0 V and (b) Wire, 1.5 V. (c) Current-carrying liquid metal wire rotated by the Lorentz force within a magnetic field. (d) Schematic illustration of experimental setup, a blue piece of paper covered one wall of the vessel to facilitate imaging. (e) Original images showing the LMW path resulting from different positions of the magnet with N pole outwards. The dotted lines indicate the location and the shape of the magnet. (f) False colored images of LM (white) showing four sequences of frames with a force diagram and motion analysis.

Here, the viscous drag is neglected as it only dissipates energy and does not dictate the path of the LMW. The interfacial tension is extremely low ($\sim 10^{-5}$ mN/m). Considering the basic unit of the liquid metal wire is a cylinder, the Laplace pressure could be shown as the equation:

$$\Delta P = \gamma \frac{dA}{dV} = \frac{\gamma}{R} \tag{4-1}$$

Given that radius (R) is about 50 μm, then the scaling of pressure difference ΔP is

about 2 x 10^{-4} Pa. Moreover, the surface charge will experience the electrostatic pressure P_E of the external electric field, the LMW (anode), the cathode and NaOH can be regarded as the parallel capacitor:

$$P_E = \frac{\varepsilon_r \varepsilon_0}{d^2} U^2 \tag{4-2}$$

where $\varepsilon_0 = 8.854 \times 10^{-12}$ C^{2}N^{-1}m^{-2} is the vacuum permittivity, $\varepsilon_r = 70$ is relative permittivity of 1M NaOH solution, U is external potential of 1.5 V, d is the distance between the electrode and liquid metal wire of 5 cm. And the scaling of P_E is about 5.6×10^{-7} Pa. The LMW will be under the electromagnetic pressure as it whips by the Lorentz force:

$$P_L = \frac{F_L}{S} = \frac{B \cdot i_m \cdot \Delta L}{\pi R \cdot \Delta L} = \frac{B \cdot i_m}{\pi R} \tag{4-3}$$

where B is about 0.1 T, i_m is measured electrical current about 60 mA. The scaling of P_L is about 38.22 Pa, which is much larger than the other possible sources of pressure. Thus, the influences of Laplace and electrostatic pressure are also negligible when compared to the pressure from Lorentz force.

Yet, as the Lorentz force redirects the path of the metal, its motion retards as it approaches the edge of the magnet (from any direction). The edge of the magnet is the location at which changes in magnetic flux are greatest and thus, the forces from Lenz's law are largest. As shown in **Figure 4.1f**, the motion is divided into four stages. In the first stage, the Lorentz force directs LMW outward, and Lenz's force is presumably negligible since the liquid metal is still within the uniform field of the magnet. At stage 2, the LMW moves near the left edge of the magnet. At this location, the LMW experiences the maximum Lenz's force and a decreased Lorentz force (since it is no longer in the strongest part of the magnetic field). Therefore, its outward motion slows at this location. Yet, the fresh LMW continues to pump from the nozzle and emerges under the control of the relatively large Lorentz force. Thus, it moves outward radially, but in a

direction influenced by the instantaneous shape of the metal. For example, in the snapshot shown in **Figure 4.1f** (stage 2), the metal that emerges from the nozzle (and thus the current in the wire) directs to the right (the "3 o'clock position"). In stage 3, a greater portion of the LMW reaches the edge of the magnet, yet the Lorentz forces continues to drive outward the fresh metal emerging from the nozzle. Finally, in stage 4, the LMW fully covers the circumference of the magnet and roughly adopts its square shape (shown in yellow dotted square box), while the fresh LMW emerging from the nozzle keeps moving in response to the Lorentz force. Taken in sum, the LMW experiences the Lorentz force as it exits the nozzle, while Lenz's law force slows the motion and levitates the wire at the circumference of the magnet.

Two representative magnet positions ($P_M = 0$ and -3 cm) are picked for detailed Lorentz force analysis of the motion of LMWs. As shown in **Figure 4.2**, for $P_M = 0$ cm, the magnetic field could be divided into two perpendicular field (B_1 and B_2), B_1 is perpendicular to magnet (vertically outwards to magnet), the corresponding Lorentz force is F_1, which is parallel to magnet drives the LMW radially outwards. B_2 is parallel to magnet, the corresponding Lorentz force is F_2, which is perpendicular to magnet and drives the LMW towards the magnet (be drawn to magnet). In summary, the LMW moves radially outwards and get close to the magnet at the same time.
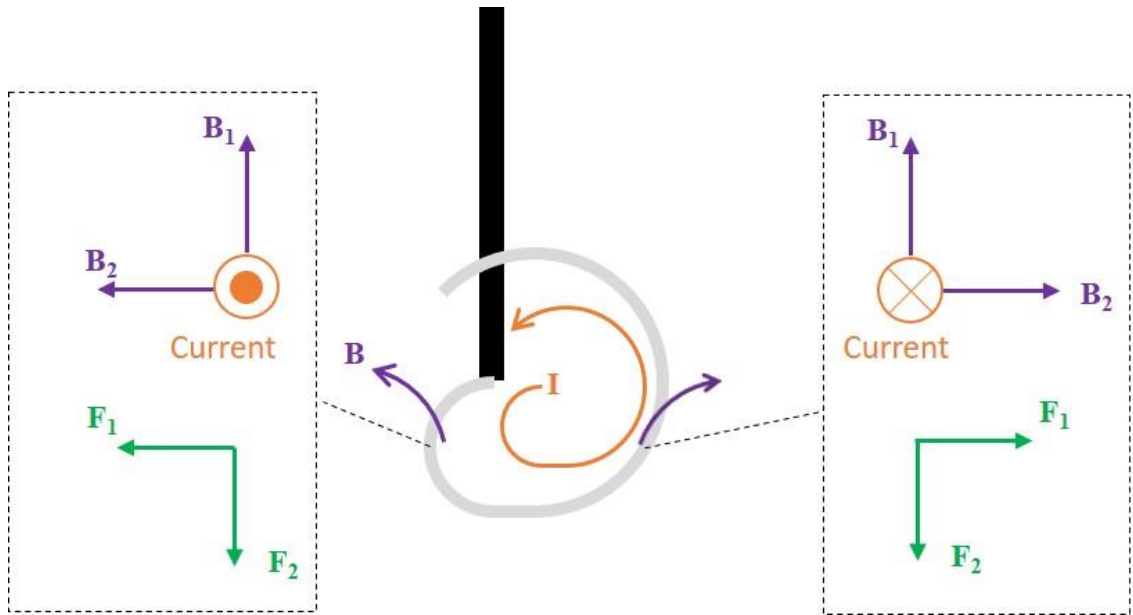
Figure 4.2. The magnetic field distribution and the corresponding Lorentz force on the LMW at $P_M = 0$ cm.

For $P_M = -3$ cm, the LMW moves in spiral motion, as shown in **Figure 4.3**. It could be seen in **Figure 4.3a** that the LMW has a curly motion through the time evolution of the trajectory. The Lorentz force is analyzed at the time (t) of 0 and 0.228 s, as in **Figure 4.3b** and **c** respectively. The left image is detailed analysis while right image is the simplified analysis.
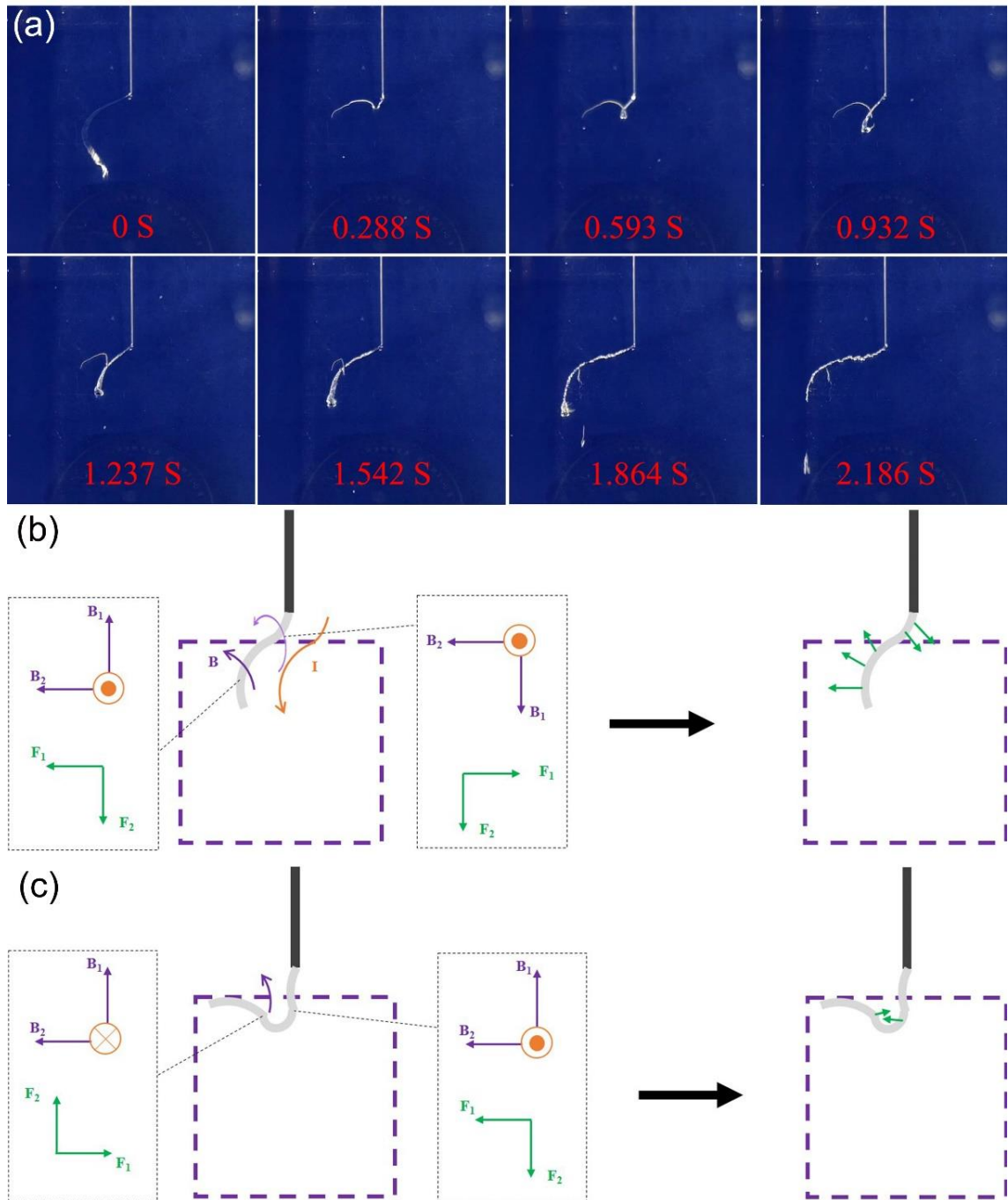
Figure 4.3. The time evolution of the trajectory of the LMW at P_M = -3 cm (a), the magnetic field distribution and the corresponding Lorentz force of the LMW at 0 s (b) and at 0.288 s (c).

The downward motion of LMW is stopped by Lenz's law, while the LM keeps ejecting from the nozzle. Then the LMW can be divided into 2 parts: inside and outside

the magnet. At $t = 0$ s, based on the distribution of magnetic field and the direction of current, the inside part will be driven by the radially outward Lorentz force, while the outside part experiences the perpendicular downward Lorentz force. Thus, the inside and outside parts both move to the edge of magnet. However, the outside part will keep moving and cross edge to enter the magnet. Once this part is in the magnet, the LMW will form a concave shape (snapshot of 0.288 s), and the Lorentz force also changes. At $t = 0.288$ s, the LMW will experience two opposite Lorentz forces at the concave part, driving the LMW form the curly shape.

The larger Lorentz force, the faster the LMW deviates from its natural linear downward trajectory. The VR controls the linear velocity of LMW; thus, higher VR will produce longer LMW (larger current at the same time) for a fixed time. Thus, I performed a series of experiments to gain insight into the mechanism of the electromagnetically driven trajectories of the LMWs as functions of both VR and the magnetic field strength (B) for fixed $P_M = 0$ cm and $V = 1.5$ V. **Figure 4.4** shows the trajectory of LMW at different times under various magnetic fields and VRs. **Figure 4.4a** shows the trajectory for VR = 2 μl/s and $B = 0.1$ T, with the N pole pointing outwards. The trajectory is a 'semicircle swing arm' moving clockwise (combination of both circular and curl motions). The same trend occurs for the S pole pointing outwards except that the LM moves counterclockwise. Increasing the VR to 4 μl/s, while keeping $B = 0.1$ T (**Figure 4.4b),** increases the length of the LMW for the same time duration for all the stages, as expected. At this increased flow rate, the maximum width of the trajectory increases to 5.0 cm (**Figure 4.4b**), and the total elapsed time reduces to 0.62 s for the four stages (in contrast, the shape in **Figure 4.4a** forms in 0.87 s with a width of 4.7 cm). It is evident that the increased Lorentz force drives the faster motion in longer wires produced by high VRs.

To examine the effect of field strength on the trajectory of the LMW, experiments

were also carried out with a magnetic field strength of 0.2 T (simply stacking one more magnet) with a fixed VR (2 or 4 μl/s). In **Figure 4.4c**, for VR = 2 μl/s, the size of the trajectory is significantly enlarged (width up to 5.5 cm) relative to 0.1 T, while the time for the motion (each stage) remains almost the same compared to that in **Figure 4.4a**. However, upon increasing the VR to 4 μl/s, as shown in **Figure 4.4d**, the enlarged size (width of ~5.3 cm) and the same time scales are also observed compared to those in **Figure 4.4b.** Moreover, the increased VR decreases the amount of time to reach each stage is mainly due to the reduced elapsed time at Stage 1. Which may be attributed to the accumulation process for the LMW to reach to a sufficient length at initial stage, to induce sufficient Lorentz force to redirect the path of the LMW (lift the LMW in stage 1).

To further demonstrate how Lorentz force drives the trajectory of LMWs from the first stage to the beginning of the third stage, the calculated average velocities (***v*** equals to the total length divided by time) and diameters of the LMW at different times, as reported in **Figure 4.4e**. The fourth stage is excluded in the plot since the effect of Lenz's law causes the LMW to fully stop at the edge of the magnet. There are major differences in the acceleration time and final velocity of LMWs depending on the conditions. For VR = 2μl/s, the velocity, ***v***, can reach about 20 cm/s in 0.7 s, while for VR = 4 μl/s, the velocity reaches up to 35 cm/s in as short as 0.45 s. Moreover, for the second stage, the acceleration (*a*) is about 60 cm/s^2 for VR = 4 μl/s, while it is about 40 cm/s^2 for VR = 2 μl/s. Doubling the magnetic field intensity has little effect on the average diameter and velocity of the LMW.
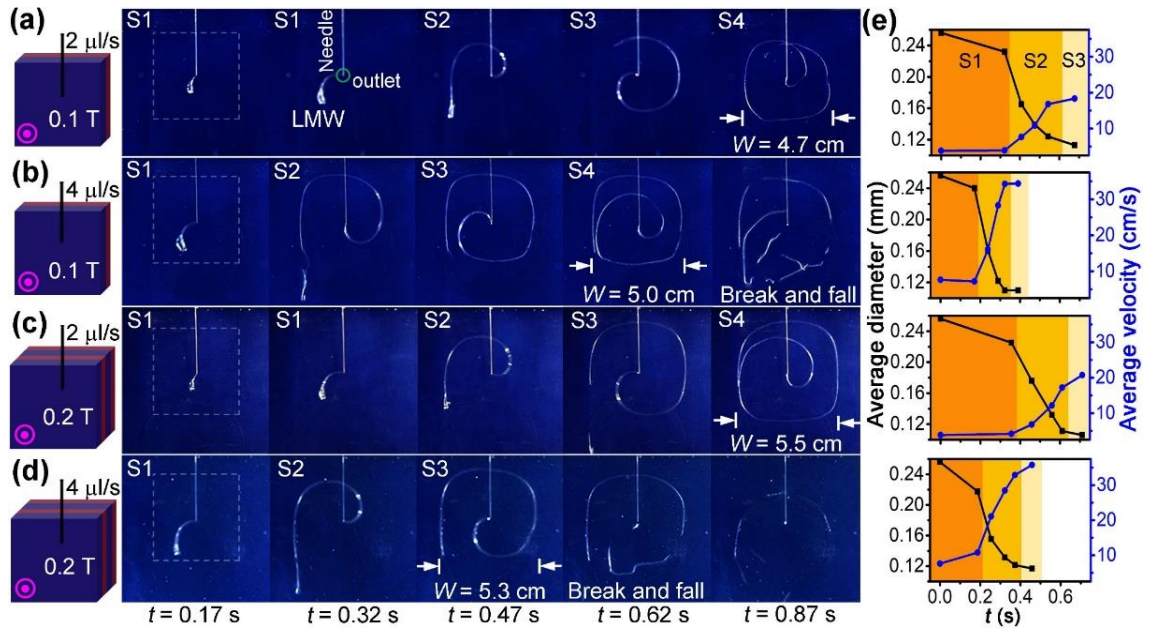
Figure 4.4. Liquid Dynamics under Various Magnetic Fields and VRs. Sequence of photographs recording the motion of a liquid metal wire under different experimental conditions with the magnet center fixed at 0 cm, N pole outwards. (**a**) 2 μl/s, 0.1 T; (**b**) 4 μl/s, 0.1 T; (**c**) 2 μl/s, 0.2 T; (**d**) 4 μl/s, 0.2 T. The square-shaped magnet is with dimensions of $5 \times 5 \times 0.5$ cm^3. (**e**) The changes of average velocity and diameter of LMW. The fourth stage is excluded from (e) as LM wire fully stops at the edge of magnet.

More detailed statistical results for elapsed time and the size of the trajectory, including height (H_{max}) and width (W_{max}) are shown in **Figure 4.5.** As shown in **figure 4.5a**, the curves represent the elapsed time as 'semicircle swing arm' moves clockwise of 90 degrees at intervals. And the VR determines the total elapsed time of the rotation process. While **figure 4.5b** demonstrate the size of the path of LMWs, and it is the magnetic field intensity that dominates the size.
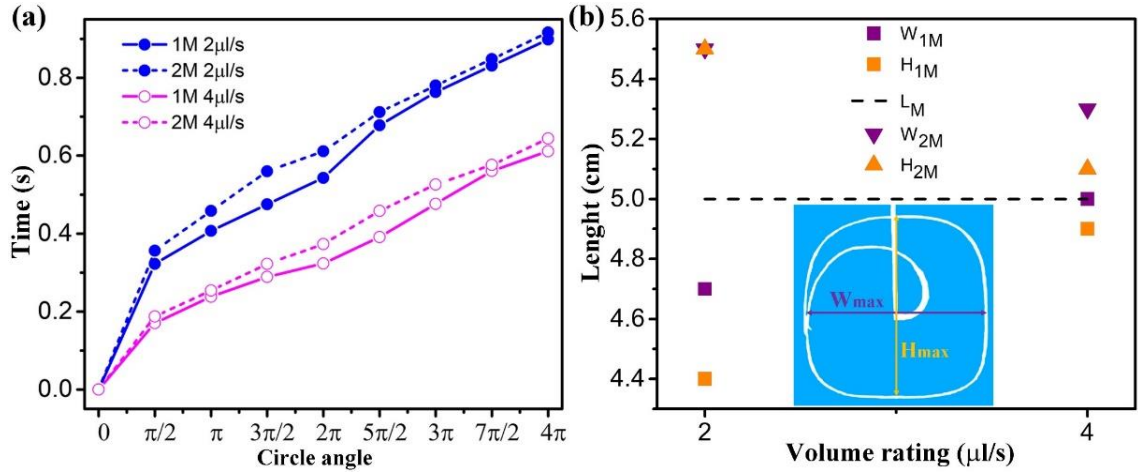
Figure 4.5. Statistical Results for Elapsed Time and the Size of Path. (a) Elapsed time with circle angles. (b) the size of the path of LMW under different conditions, including height (H_{max}) and width (W_{max}). L_M stands for the length of the magnet (fixed at 5 cm).

In fact, the velocity used here is a resultant velocity, as LMW is accelerated outward. At beginning, the LM is ejected out from the nozzle at a VR controlled by a syringe pump. The value of VR determines the initial velocity of the LMW (for VR = 2 ml/s, the initial velocity is about 3.7 cm/s), it is the v_1 along the LMW. At this initial stage, the true velocity (v) of the LMW equals to v_1. As the LMW is formed, it will experience the Lorentz force, which accelerates the LMW radially outwards, it is the v_2 perpendicular to the LMW. And v_2 keeps increasing to a large value (e.g., 20 cm/s) before it slows by Lenz's law. At this stage, the velocity (v) of the LMW is the resultant velocity of v_1 and v_2, as shown in **Figure 4.6**. The value of v_1 is influenced by gravity, considering that the LMW rotates in a small region (-2.5 ~ +2.5 cm) at $P_M = 0$ cm, the value of v_1 is taken as a constant. As v_2 is increasing, the direction of v will vary from the direction of v_1 to the direction of v_2. When the value of v_2 is significantly larger than v_1, the value and direction of v will be very close to that of v_2, as in **Figure 4.6**. The velocity of the LMW is calculated through the length of the LMW divided by time, this should be the true velocity (v) of the LMW. And the increase of v is due to the increase of v_2, thus, the increase of v shows the

96

acceleration of Lorentz force.
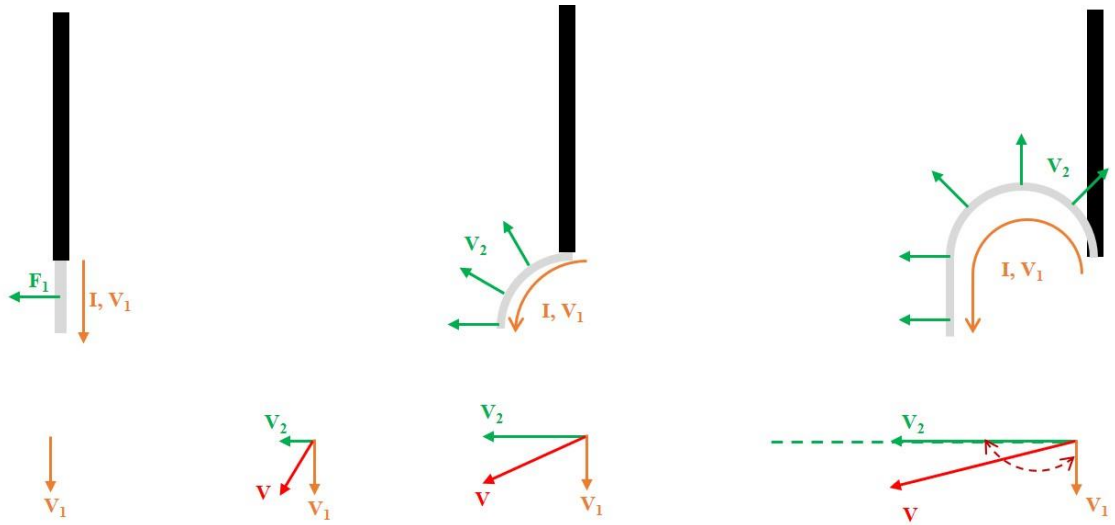
Figure 4.6. the velocity change of the LMW during the acceleration outwards process. v_1 is the velocity of LM flowing along the LMW, v_2 is the Lorentz force accelerated radially velocity, v is the true velocity of the LMW (resultant velocity of v_1 and v_2)

The results indicate that increasing the VR reduces the total time, while doubling the magnetic field considerably increases the size of the trajectory. Importantly, during the acceleration by the Lorentz force, the average diameter of the LMW's cross section decreases from 0.25 at stage 1 to 0.11 mm at stage 3. According to Newton's second law $\frac{\partial p}{\partial l} = -\rho \frac{\partial v}{\partial t}$, where ρ is the density of liquid metal wire. The decrease in diameter leads to the increase of velocity, and this further decreases the diameter of the wire, causing further acceleration in a positive feedback loop. Furthermore, the total length of the wire increases simultaneously, which leads to an increase in the current and the Lorentz force. Thus, the radial acceleration of the LMW consists of two contributions: the Lorentz force and the reduction of mass per unit length from the elongating wire (i.e., narrowing diameter and simultaneous elongation of LMW). In contrast, the force from Lenz's law slows down the LMW as it reaches the edge of the magnet.

In the central region of the magnet, the Lorentz force accelerates the LMW outward until it reaches the edge of the magnet, at which point it slows, stops, and ultimately levitates due to Lenz's law. Next, the trajectories (stage 4) of the LMW driven dominantly by the force from Lenz's Law are demonstrated. The experiments are designed to let LMW move into the region of the magnet by placing the magnet below the syringe (**Figure 4.7**). The gravity is allowed to accelerate the metal downward to form long LMWs to maximize the effect of Lenz's law.

First, the metal was pumped at a VR of 2 μl/s without a magnet to investigate the change in the velocity of the LMW due to gravity. A sequence of frames collected with an interval of 0.034 s allowed estimates of the velocity as shown in **Figure 4.7a**. The LMW emerges initially from the nozzle as a small bead. Gravity pulls this bead from the nozzle and a cylindrical stream follows. This acceleration causes the leading bead to reach a maximum value of ~25 cm/s at the position of -6 cm. Below this position, the velocity has an almost a constant value. The velocity change can be fitted with an exponential function. Thus, a few typical positions are chosen, representing four different velocities, to study the effect of the velocity on the LMWs in the presence of a magnet (N pole points outwards and $B \sim 0.1$ T) centered at these positions. The positions are marked as b, c, d, and e in **Figure 4.7a**, corresponding to the positions of -4, -5, -6, and -9 cm, respectively.

The images of the LMWs' trajectories for different P_M are shown in **Figure 4.7b-e**. For the $P_M = -4$ cm, the metal wire undergoes a clockwise spiral motion within a small region near the left-upper edge of the magnet. The trajectory becomes larger for $P_M = -5$ cm. There is a big difference in the LMW trajectory for $P_M = -6$ cm. The trajectory adopts the same square shape of the magnet circumference. The case is the same for the $P_M = -9$ cm. These results show that the force from Lenz's Law is fully responsible for the positioning of the LMW along the edge of the magnet at $P_M = -6$ cm, while the Lorentz

force only directs the outward motion during stage 1. The same experiments by putting the magnet with S pole outward are also performed, the same effects occurred except the LMW rotated anti-clockwise.
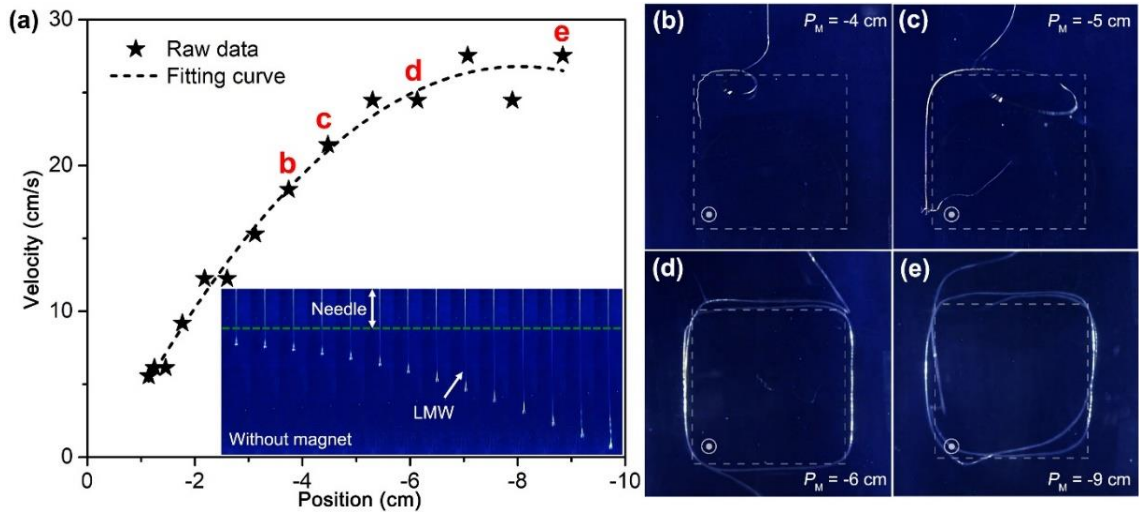
Figure 4.7. Role of Velocity on LMW Trajectory. (a) The velocity of LM pumped from the needle at 2 μl/s without a magnet, with the inset showing snapshots of the trajectories. The green dotted line represents the needle outlet, above the green line is the needle, while under the green line is the LMW. (b-e) and the typical trajectories under 0.1 T magnetic field at different positions with the N pole outwards. The dotted lines indicate the location and the shape of the magnet.

It is remarkable that the trajectory of the LMW (for P_M = -6 cm) adopts the same shape as the periphery of the square-shaped magnet. Thus, detailed Lorentz force and motion analysis are conducted for P_M = -4 and -6 cm to show the difference. As shown in **Figure 4.8**, for P_M = -4 cm, the LMW also moves in spiral motion. The motion is similar with that of LMW at P_M = -3 cm. The difference is that the spiral area is larger at -4 cm, which could be attributed to that the outside part of the LMW moves a longer distance along the magnet upper edge before the outside part enters the magnet. The

Lorentz force analysis shows that as the magnet is farther away from the nozzle, the part of the LMW near the nozzle will experience an upward Lorentz force (pointing away from the magnet), which will lift the part of magnet, contributing to the longer motion along the magnet edge.
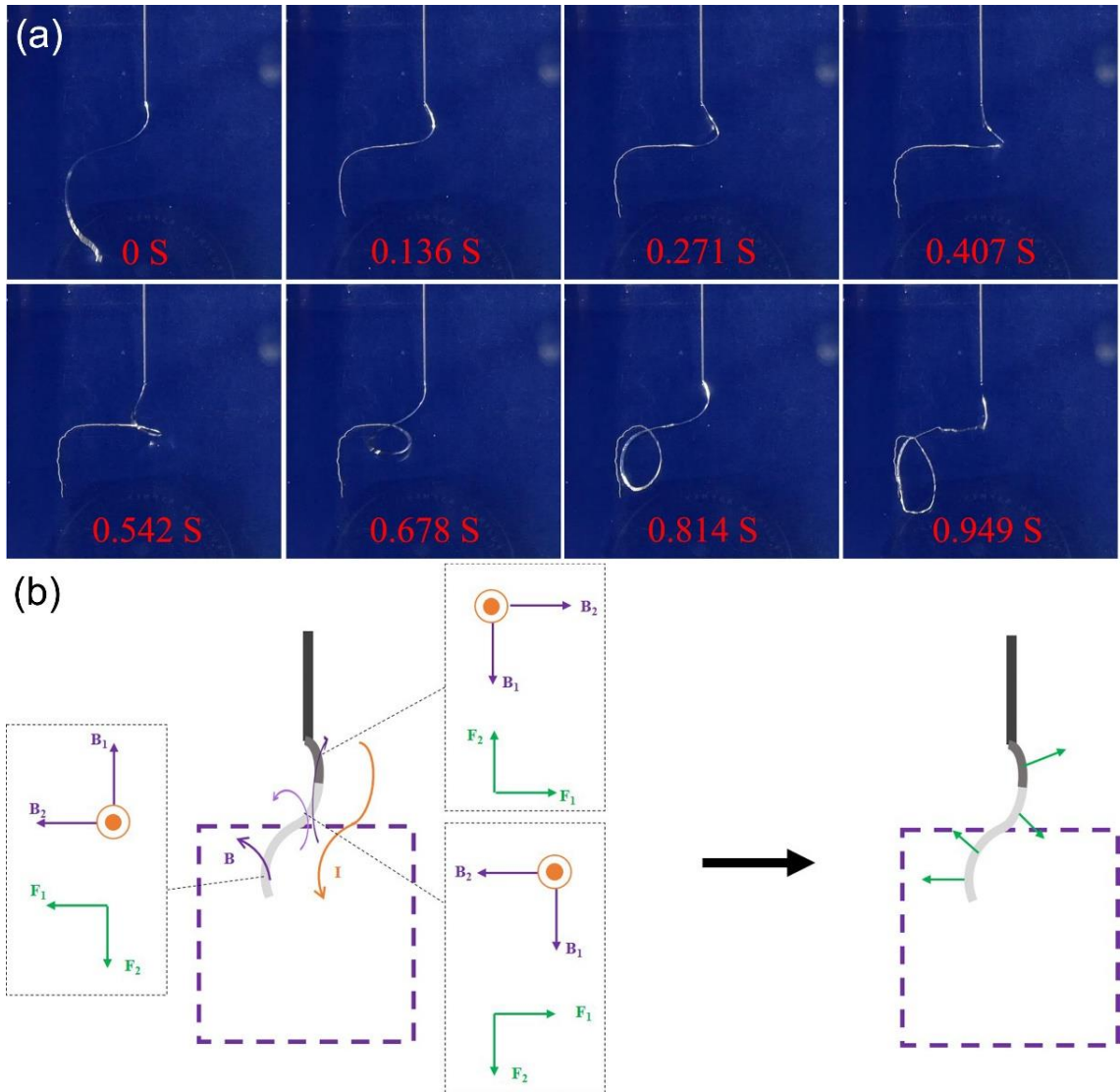
Figure 4.8. The time evolution of the trajectory of the LMW at $P_M = -4$ cm (a), the magnetic field distribution and the corresponding Lorentz force of the LMW at 0 s (b).

While for $P_M = -6$ cm, the big difference is that the LMW circles around the magnet. In fact, the circular motion at $P_M = -6$ cm is a kind of spiral motion like that at $P_M = -3$

and -4 cm, just because the motion of the LMW at -6 cm can cover the whole magnet. And the main factor is that the magnet much farther away from the nozzle, a larger part of the LMW near the nozzle will experience the upward Lorentz force. This enables that the LMW can move along the whole edge of magnet, as shown in **Figure 4.9**.
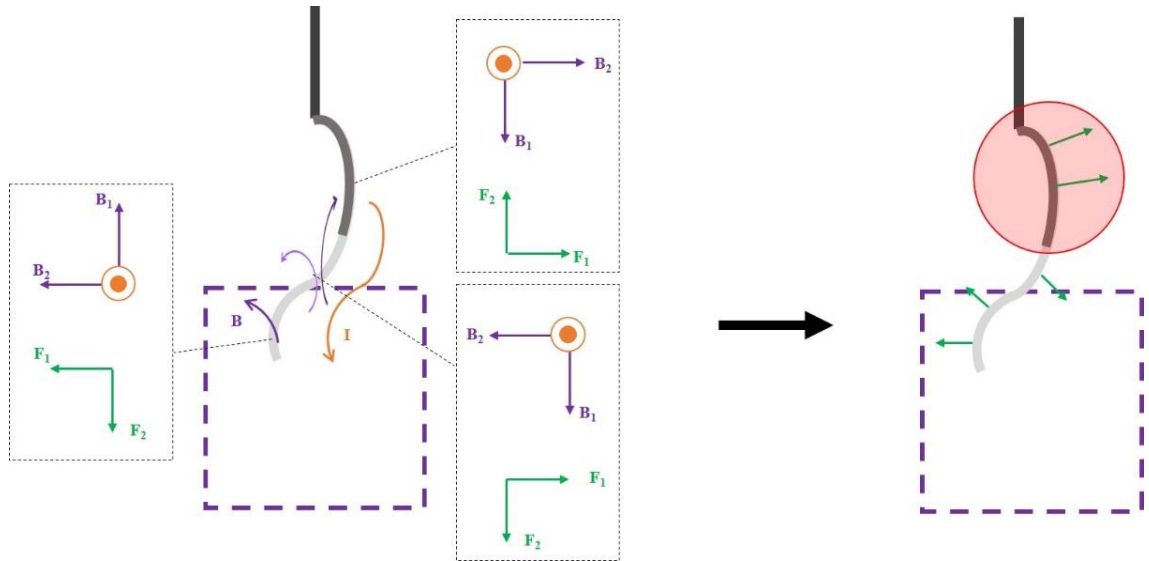
Figure 4.9. The magnetic field distribution and the corresponding Lorentz force of the LMW at P_M = -6 cm.

To further demonstrate the effect of LMW adopting the same shape of magnet, experiments using magnets with different shapes at P_M = -6 cm are also performed. As shown in **Figure 4.10a-c**, the shapes of LMW's trajectories match well with those of the magnets (**figure 4.10d**). These results show that the liquid wire arrests around the perimeter of the magnets where the divergence of the magnetic field or Lenz's Law force is largest. Experiments using two magnets which are arranged in various configurations at P_M = -6 cm are also conducted. For the configuration I (**Figure 4.10e**), two circular magnets were placed side-by-side at a distance of 0.5 cm with their N poles outwards. Placing the needle in the middle of the two magnets caused the LMW to move along the edges of the two magnets. It takes about 1 s for the wire to complete one loop. The whole

circular process lasts for 4 loops in about 4 s, before the LMW breaks and falls at the 5th loop. It is remarkable to note that all the loops appear to stay still (or levitate) and do not fall despite the density of the metal being nearly 6x larger than the electrolyte. When the S poles of the magnets point outwards, the motion of the LMW in **Figures 4.10f** is complementary (but in opposite directions) to the N poles outwards.

In configuration II (**Figures 4.10g, h**), two circular magnets were placed side-by-side, separated by a distance of 0.5 cm, with the N pole outwards for the left-side magnet and the S pole outwards for the right-side magnet. Unlike the configuration I, the LMW could no longer move along the two magnets, and it only circled around one of them, depending on which was closer to the needle instead. The LMW continues circling around the magnet within ~1 s and breaks and falls at end of the 3rd loop.

In the configuration III, two circular magnets were aligned vertically at a distance of 0.5 cm with N poles outwards. **Figures 4.10i** show that the LMW prefers to circle around the upper magnet. When the LM begins to drop down under the influence of gravity, however, the lower magnet slows down the descent and pulls the LMW to the edge of the lower magnet. When the first loop is finished, the bottom part of the LMW begins to slowly drop. The lower magnet gradually pulls this portion to its edge. When the third loop of liquid metal forms, the bottom part of the first loop reaches its maximum size and just moves along the edge of the lower magnet, this process is cyclic. Moreover, when the S poles of both magnets are arranged outwards, the motion of the LMW in **Figures 4.10j** is complementary to that when the N poles are outwards.

In configuration IV, two circular magnets align in a vertical column. One of them has the N pole outwards while the other has the S pole outwards. The results in **Figure 4.10k** and **Figure 4.10l** are almost the same: the LMW just moves around the upper magnet regardless of the magnetic pole. The LMW never circles around the lower magnet,

and the magnetic field of the lower magnet does not influence the falling process at all.
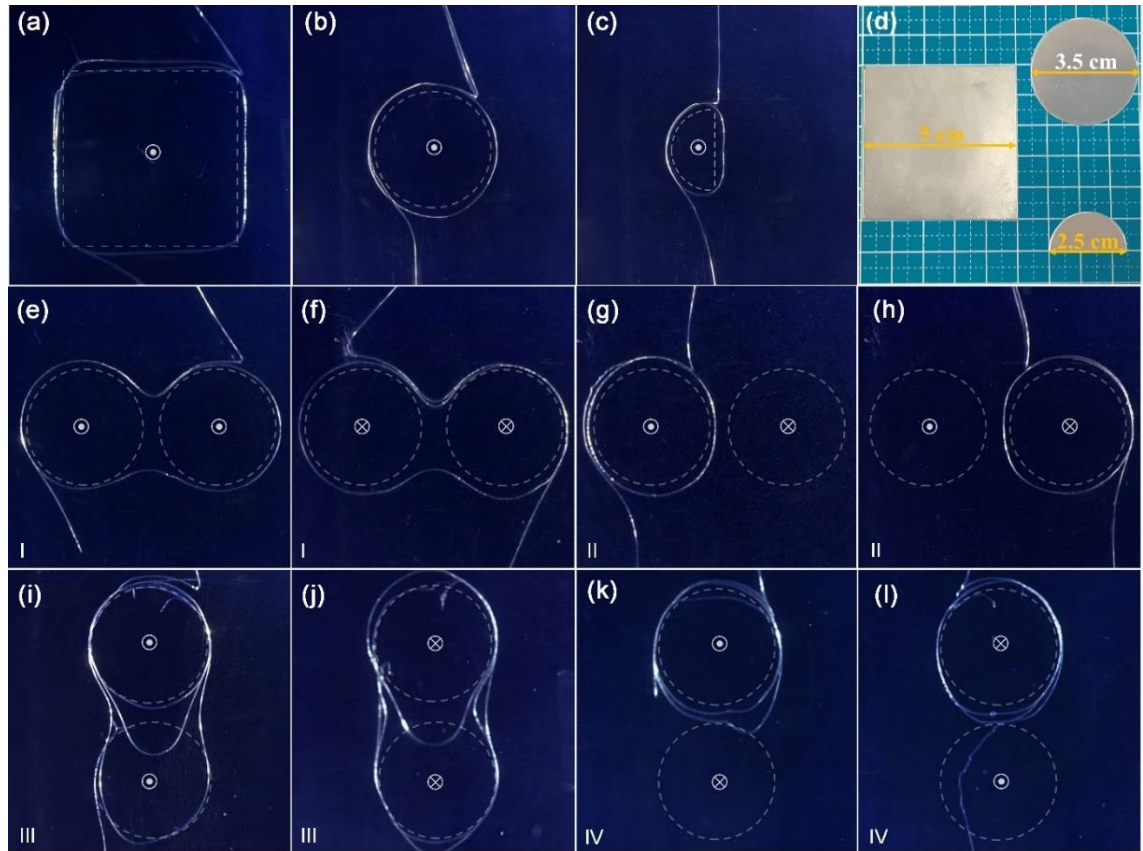
Figure 4.10. The liquid metal traces out the perimeter of the magnets, which are located behind the blue paper. The liquid metal can be configured into different shapes (a-d) and complicated magnetic field arrangements by using two circle magnets with diameters of 3.5 cm, (e-h) N/S poles placed side by side with a distance of 0.5 cm; (i-l) N/S poles arranged vertically with a distance of 0.5 cm. The yellow dotted lines indicate the location and the sahpe of the magnet.

In the four configurations, the liquid metal makes the hidden magnet effectively 'visible' by tracing the perimeter either immediately (configuration I) or in a gradual way (configuration III). Moreover, the displayed magnet can be re-invisible again by just reversing the N/S pole, which is just like an on-off switch.

In addition to these static patterns, I have also performed the dynamic pattern as the magnet moved horizontally at P_M = -6 cm. Here the square-shaped pattern of LMW displaced along with the magnet. When, the magnet moves to right at a very slow speed of 0.2 cm/s, the LWM also adopts the same shape of the square-shaped magnet at each position, as shown in the selected four patterns at different time (1st, 2nd, 3rd and 4th patterns are respectively at the time of 2 s, 6 s. 11 s and 16 s) in **Figure 4.11a**. The images on the far right are the superposition of the first four snapshots. However, the LMW breaks between the sequential patterns. That is, as the magnet moves to right, the LWM firstly break, and then quickly forms another pattern at a new position. When the speed of magnet displacement is increased to 1 cm/s, the dynamic pattern of LMW became a continuous process without any breakage, while slight distortion of the squared shape emerged (**Figure 4.11b**). As the speed of magnet was further increased to 3 cm/s, it was still a continuous process with obvious distortion of its squared shape (**Figure 4.11c**). These different dynamic patterns are controlled by Lenz's Law force, while higher speed of magnet induces larger Lenz's law forces, leading to significant distortion of the LMW pattern. All the patterns of LMWs are stable during the motion of the LMWs, which are unexpected and novel. The transiently stable wire and pattern structures could be formed under the interaction of electromagnetism and fluid dynamics by overcoming the Plateau-Rayleigh instability, realizing non-contact manipulation of liquid metal wires.
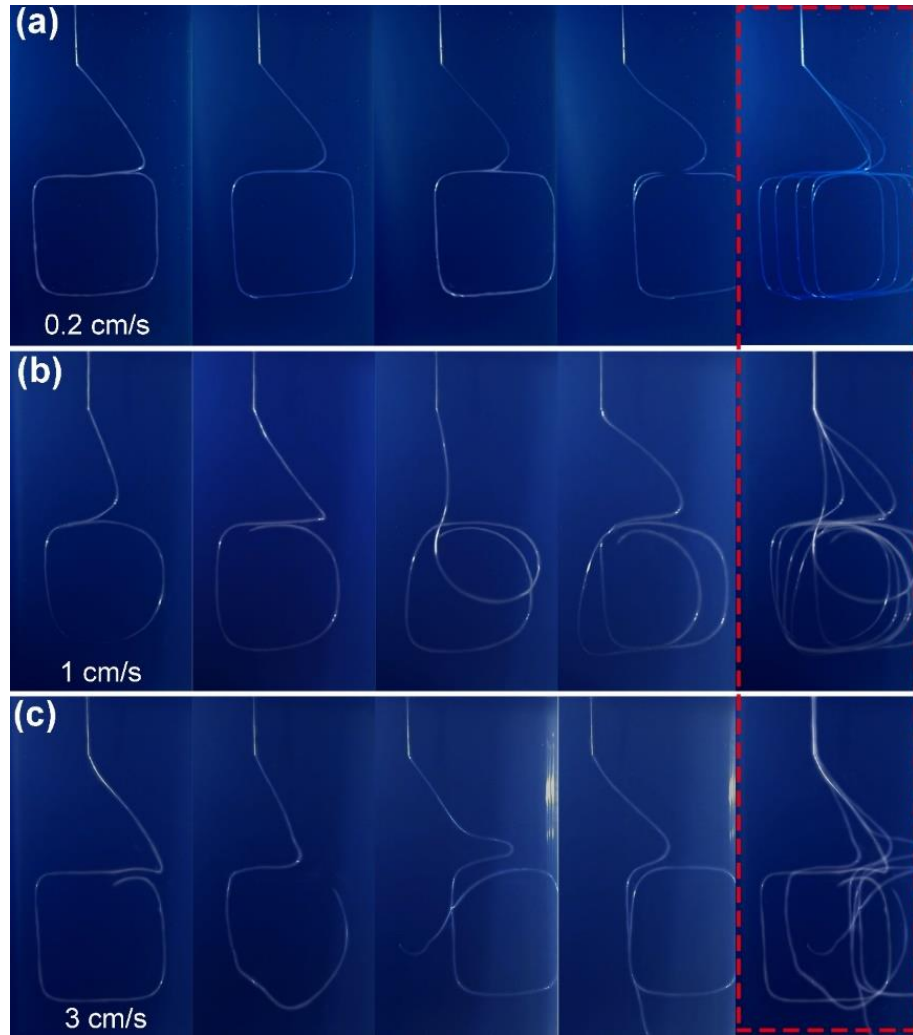
Figure 4.11. Representative images of dynamic patterns of LMW as magnet moved horizontally at $P_M = -6$ cm with different speed, N pole outwards and 0.1 T. (a) 0.2 cm/s, (b) 1cm/s, (c) 3cm/s. The images on the far right are the superposition of the first four snapshots.

To analyses the dynamics of LMWs, I build a physical mode based on the electrical current passing through the LMWs as the current plays an important role during the electromagnetic interaction induced motion of LMW. The electric current is believed to originate from the oxidizing surface reaction: $Ga \rightarrow Ga^{3+} + 3e^-$. The current travels through the wire (electrons flow toward the nozzle). I reason that the current should increase with proximity to the nozzle for two reasons: (1) fresh metal interface forms as

the metal exits the nozzle and must be oxidized via this reaction and (2) any oxide that dissolves in the NaOH solution along the length of the wire must be replaced electrochemically. The current, therefore is greatest near the nozzle, which has subtle implications for the behavior of the liquid metal thread. For example, the deformations for $P_M = +3$ and -3 cm are slightly different, though the magnetic field intensity at these two positions are almost the same. I reason that the current density is lower at $P_M = -3$ cm and thus the force is smaller.

To verify this, I have measured the electrical current in the circuit under different conditions. The electrical currents are collected by Keithley DMM 2002 on a Labview platform for three cases:

1) absence of LMW and magnet.

2) free falling of LMW without a magnet.

3) Substitute the LMW by a copper wire with comparable in diameter and length.
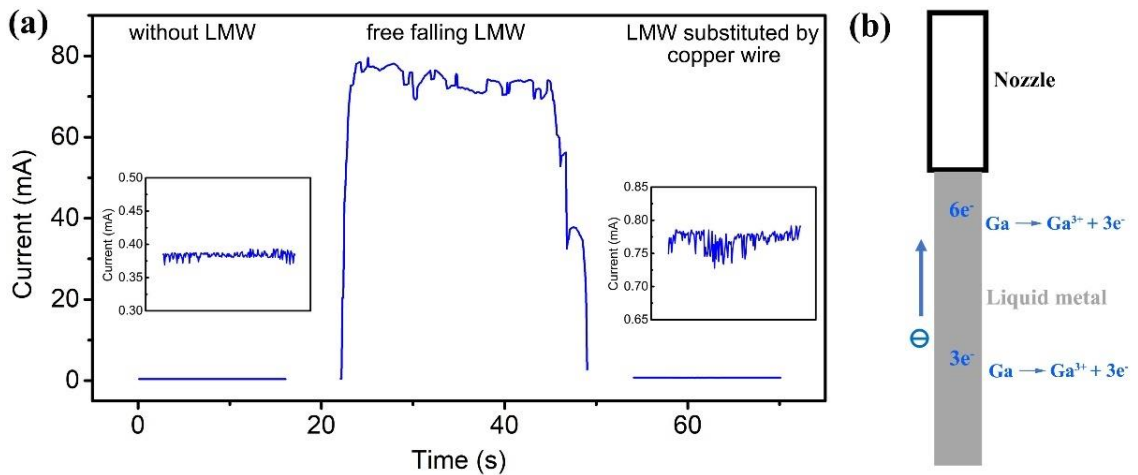
Figure 4.12. (a) The measured electrical current passing through the LMW and its comparison to the cases without the wire and with a copper wire under the same external voltage fixed at 1.5 V. (b) the diagram of electrons flow toward the nozzle. Here, I depict two oxidation reactions occurring at distinct positions, although in reality there are reactions occurring along the entire length. Consequently, the current increases along the

length of the metal toward the direction of the nozzle due to the cumulative effect of oxidation along the length of the wire

As shown in **Figure 4.12,** for the case 1, with the external voltage fixed at 1.5 V, the current is ~ 0.4 mA. While for case 2, the current increases by ~200x to ~80 mA (here the length of LWM is about 11 cm). Furthermore, the current remains nearly constant during the free falling of the LMW. For case 3, although copper wire is a good conductor as LM, it gives an insignificant current (< 1 mA) without the formation and dissolution of oxide. And for case 1 and case 3, the fluctuation on current is very small and it should be attributed to background noise. While for case 2, the fluctuation (about 10 mA) is induced by the dynamic oxidation/dissolution of surface oxide layer as above-discussion.

The current of the LMWs with different length are also measured and analysed, as shown in **Figure 4.13**. Here, the LMWs are obtained with length ranging from 5 to 14 cm, and all LMWs with different length can stably flow as LMs are pumped out from the syringe.

The current is divided into three regions (abbreviate as R1, R2 and R3 in **Figure 4.13a**). R1 refers to region where LMW freely falls from nozzle to bottom substrate. Current will quickly increase with the length of LMW for R1 region. R2 refers to region 2 where LMW keeps flowing stably, and the current remains a relatively stable value with small fluctuation induced by dynamic oxidation/dissolution on the surface of LMW. However, there are different humps appeared for the current curve for LWM length of 5 cm. This is because when LMW reaches the bottom substrate, it will not disintegrate into droplets immediately, yet remains as a continuous wire structure for a certain time. This leads to the slow increase in current for LWM length of 5 cm. For other LMWs with sufficient length, the cumulative effect of LMWs on bottom substrate is not significant.

R3 refers to region 3 where LM is stopped from being ejected from the nozzle. The volume of each ejection is pre-set. In my experiments, the pre-set volume of ejection to be 80 μl and the volumetric flow rate is 2 μl/s, then the duration for this ejection will be 40 s. The current will decrease to almost zero as LMWs break and falls. Moreover, the current passing through the LMWs was found to increase near linearly with the length of the wires, which can be linearly fitted by equation $y = 53.4 + 1.933x$, as shown in **Figure 4.13b**. This result agrees with my conclusion that the current is generated through the oxidation and dissolving of the surface oxide.
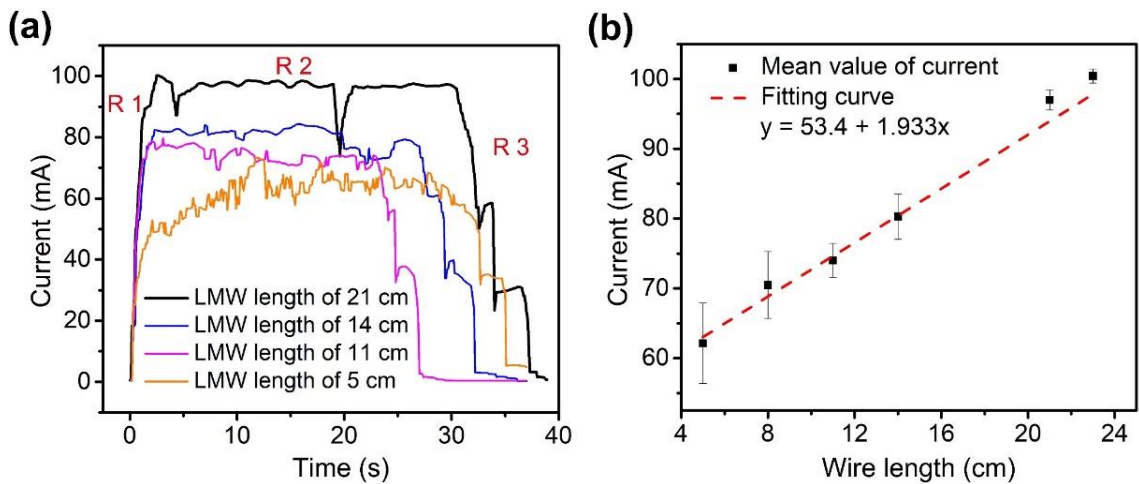
Figure 4.13. (a) Current versus time of LMWs with different length. (b) Statistical mean value of the current with different lengths measured in R2, which can be linearly fitted by equation $y = 53.4 + 1.933x$. The external voltage is fixed at 1.5 V for all cases.

When the square magnet is placed at different positions, the change of current is shown in **Figure 4.14**. Different magnet positions give rise to different currents. The currents show periodic oscillation with different frequencies and magnitudes [see **Figure 4.14a, d** and **g**]. The frequencies and oscillations correspond well to the cyclic dynamic formation/disintegration of LMWs. The frequency data is obtained through FFT of

current, and it decreases as magnet moves downwards (away from the nozzle). For the case of LMWs residing outside the magnets (P_M = -6 and -9 cm), the frequency is reduced to 0.34 and 0.20 Hz and their oscillating magnitudes are also significantly suppressed.

It is quite interesting to note that the current does not increase linearly with the increasing length of the wires. This is unexpected according to **Figure 4.13,** and the differences (**Figure 4.14c, f** and **i**) between the estimated current (i_e) and measured current (i_m) is very significant. This should be attributed to the effects of Lenz's law. The Faraday's law of induction is applied to quantitively explain the effect of the Lenz's law. For a LMW rotating in a magnet, a potential (ε) will be induced: $\varepsilon = \oint (E + v \times B) dl$, where v is the velocity of the LMW, and E is electric field along LMW. The $\oint E dl$ term on the right side of the equation shows the contribution of the Lenz's law effect, while $\oint v \times B dl$ is the Lorentz force on charges by the motion of LMW.
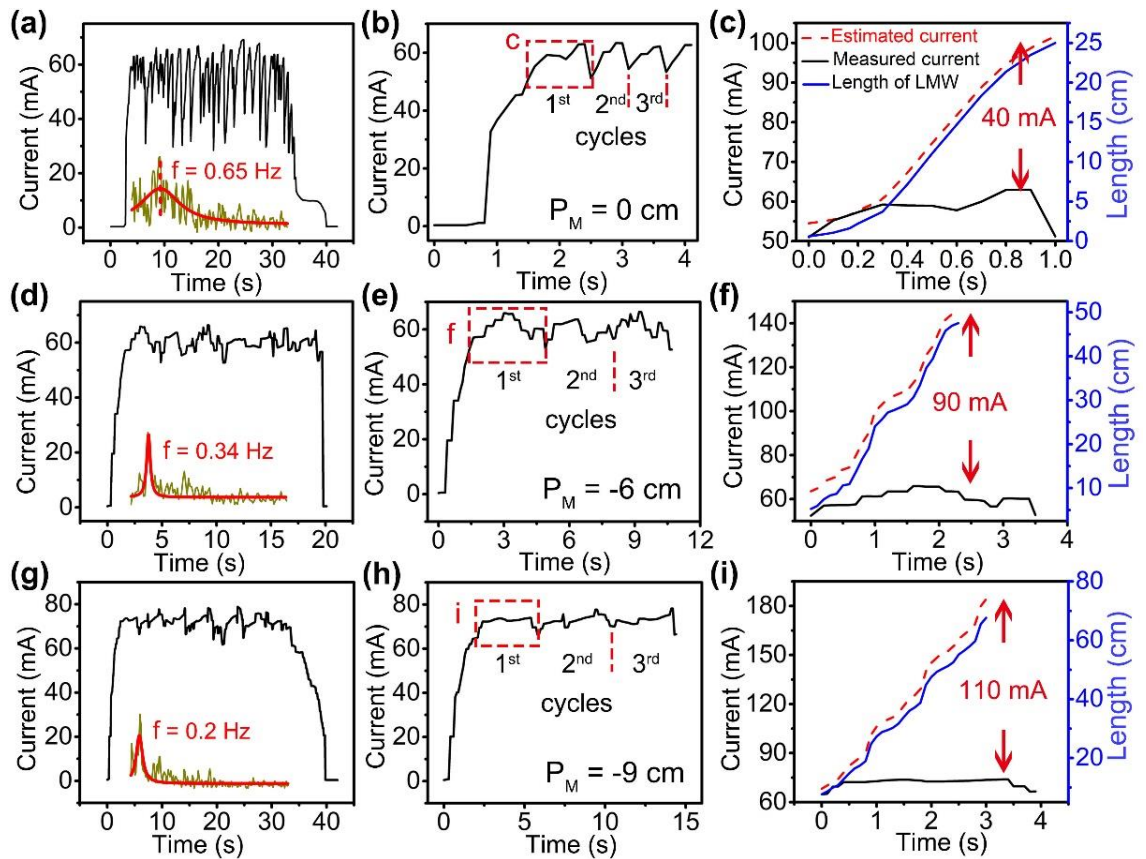
Figure 4.14. Electrical current data of LMWs with magnet placed at different positions, (a-c) P_M = 0 cm, (d-f) P_M = -6 cm, (g-i) P_M = -9 cm. The current value is synchronized with the periodically formation/disintegration of LMW. The inset figures in (a, d, g) are the frequency data through FFT of current. (b, e, h) are the first three cycles, and (c, f, i) show the current drop in the first cycle induced by Lenz's law effect. The external voltage is fixed at 1.5 V for all cases.

The current drop induced by Lenz's law effect is $i_l = i_e - i_m$. Where i_m is the measured current, $i_e(mA) = 53.4 + 1.933l\ (cm)$, l is the length of LMW. Thus, I can get the current density along the LMW:

$$J = \frac{I}{A} \tag{4-4}$$

where I is the current and A is the cross-sectional area of LMW. And a common approximation to the current density assumes the current simply is proportional to the electric field along the LMW, as expressed by:

$$J = \sigma E \tag{4-5}$$

where E is the electric field and σ is the electrical conductivity (about 3.3×10^6 S/m). Thus, the electric field along LMW could be expressed as:

$$E = \frac{I_l}{\sigma \cdot A} \tag{4-6}$$

Take the data of magnet position P_M = -6 cm for calculation, where i_m is 60 mA, the maximum length of the LMW is about 50 cm, the average velocity of LMW is 20 cm/s (one loops occurs in 1 s). The magnetic field is regarded as a uniform field (0.1 T).

$$\oint E_l dl = -\oint \frac{0.1933l - 0.0066}{\sigma \cdot A} dl = -\frac{\frac{0.1933l^2}{2} - 0.0066l}{\sigma \cdot A} \tag{4-7}$$

$$\oint v \times B dl = 2 \times 10^{-2} l \tag{4-8}$$

$\oint Edl$ is about -0.81 V (the negative sign indicates the direction opposite to that of

the oxidizing current). In comparison, $\oint v \times Bdl$ is only about 0.01 V, which is negligible. When the magnet is placed at other positions $P_M = 0$, and -9 cm, the calculated value of $\oint Edl$ is -0.18, and -1.63 V, respectively. In comparison, the calculated value of the Lorentz-force induced potential ($\oint v \times Bdl$) for the three magnet positions is only as small as 0.00625, and 0.014 V. Thus, the Lenz's law effect should be primarily responsible for the significant current drop. The effects of Lenz's Law increase with the length of the LMW, while the effect of Lorentz force on current change is negligible.

Despite that Lorentz force have no effect on the current change, it plays an important role in directing the rotation of LMW (and accelerating LMW inside magnet). Most importantly, as the LMWs reach the edge of the magnet, they stop and levitate in the solution for a few seconds. And the levitation of the LMWs is achieved due to the balance between gravity (G), buoyancy (F_b) and Lorentz force (F_L). To simplify the calculation of Lorentz force, the concept 'equivalent length', which stands for the corresponding length of measured current, is applied as follows:

$$L_e = \frac{\Delta i}{1.933} \tag{4-9}$$

where Δi is the current change in one loop when a LMW circles around magnet. For example, when magnet is at $P_M = $ -6 cm, the value of current is increased by 12 mA for two loops in 2 s, here Δi is 6 mA (12 mA/ 2 loops). Thus, the corresponding Lorentz force: $F_L = B \cdot i_{max} \cdot L_e$. Where i_{max} is the current before LMW finally starts to fall due to gravity: $G = \rho_l \cdot g \cdot V$. Where V is the volume of LMW and take buoyancy into consideration: $F_b = \rho_w \cdot g \cdot V$. The net force downward is as follows:

$$F_n = G - F_b = \Delta\rho \cdot g \cdot V = \Delta\rho \cdot g \cdot \pi r^2 \cdot L \tag{4-10}$$

where ρ_l is about 6.3 x 10^3 kg/m^3, ρ_w is 1.0x 10^3 kg/m^3, g is gravitational acceleration (9.8 N/kg), r is about 50 μm, L is the total length of LMW. Thus, I have the equation:

$$F_n = 4.08 \times 10^{-4} \cdot L \tag{4-11}.$$

Thus, the maximum length of LMW can be estimated by the following equation:

$$F_n = F_L \rightarrow L_{max} = \frac{10^4}{4.08} \cdot B \cdot i_{max} \cdot \frac{\Delta i}{1.933} \tag{4-12}$$

For P_M = 0 cm: Δi = 3.5 mA and i_{max} = 63 mA. And I can get L_{max} = 27.9 cm.

For P_M = -6 cm: Δi = 6 mA and i_{max} = 66 mA. Here, L_{max} = 50.2 cm.

For P_M = -9 cm: Δi = 8 mA and i_{max} = 73 mA. Then, L_{max} = 74 cm.

These calculated lengths are consistent with my statistical data in **Figure 4.14 c, f and j**.

Typically, within the range of LMW stably formed, the farther distance between the magnet and nozzle, the more loops will the LMW circle around the perimeter of magnet. Moreover, the frequency distributions of the current at P_M = 0 cm is decentralized, indicating an unstable structure of LMW patterns inside magnet. For other experimental conditions that LMW formed with different VRs and magnetic fields, electric currents are also measured, as shown in **Figure 4.15**. The currents of the LMWs at R2 stage (stable flowing stage) are selected to compare the current value and frequency of the LMW formed under different conditions. As expected, the current value increase by 5 mA when doubling the VR from 2 to 4 μl/s, while it significant decreases when double the magnetic field, as in **Figure 4.15e**. The difference of measured current value is consistent with my previous conclusion: the longer LMW formed in a fixed will increase the current while strong magnetic field will enhance the Lenz's law effect, leading to the current decrease. Meanwhile, the frequency decreases with the VR while significantly enlarged by doubling the magnetic field, resulting in the unstable structures and early fracture, as in **Figure 4.15f**.
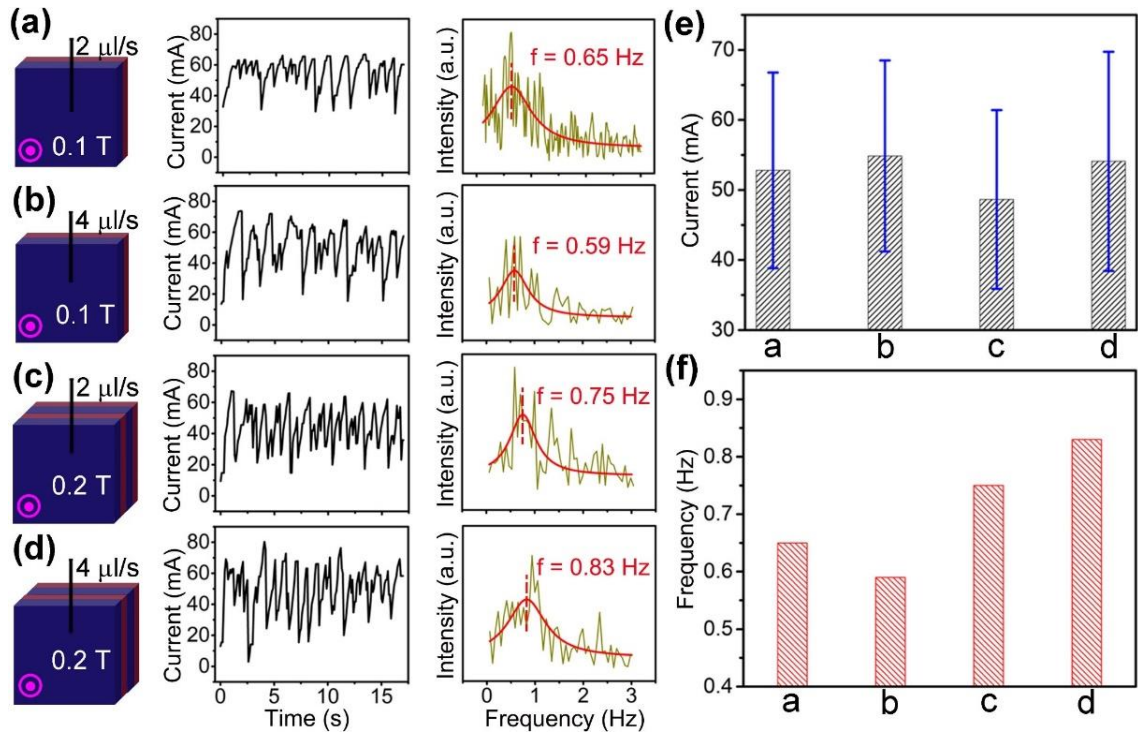
Figure 4.15. Current versus time of LMWs when a magnet placed at P_M = 0 cm under different experimental conditions. (**a**) 2 μl/s, 0.1 T; (**b**) 4 μl/s, 0.1 T; (**c**) 2 μl/s, 0.2 T; (**d**) 4 μl/s, 0.2 T.

The currents for different magnet positions when placing the magnet below the syringe are also measured. **Figure 4.16** shows the current difference for P_M = -4, -5, -6 and -9 cm. Besides the suppression of current for P_M = -6 and -9 cm, the current difference between the measured current and the estimated current (with the corresponding length) for P_M = -4, and -5 cm can be roughly calculated. For P_M = -4 cm, the length of the LMW is about 6 cm (based on the scale of dotted line of magnet size of 5 cm), the corresponding current should be 65 mA (based on y = 53.4 + 1.933x). While the measured current is about 55 mA, the current difference is 10 mA. For P_M = -5 cm, the length of the LMW is about 20 cm, the corresponding current should be 92 mA. While the measured current is about 60 mA, the current difference is 32 mA. And the current difference increases to 90 and 110 mA for P_M = -6 and -9 cm. And the strength of Lenz's law effect could be verified

from the value of current difference. Moreover, the current value keeps increasing as the magnet moving down away the nozzle (longer LMW), and the frequency decreases from 0.51 to 0.2 Hz, indicating a more stable structure at P_M = -9 cm.
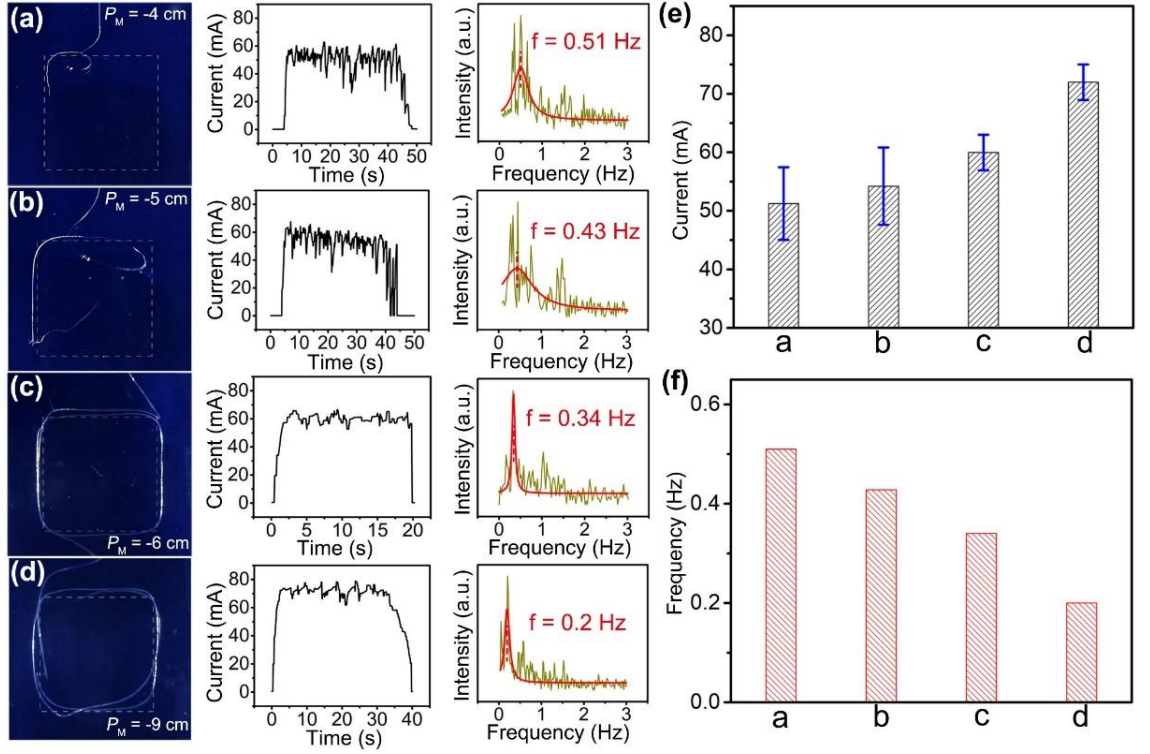
Figure 4.16. Current versus time of LMWs with a magnet placed at different positions. (a) P_M = -4 cm; (b) P_M = -5 cm; (c) P_M = -6 cm and (d) P_M = -9 cm.

As the early fracture emerges in the LMW with high velocity at P_M = 0 cm (decentralized frequency of the current) is observed, implying that the effect of inertial should also be considered as LMW whips by the Lorentz force. Here, a dimensionless number He as the ratio of inertial force and Lorentz force is defined as follows:

$$He = \Delta\rho v^2 d / B \cdot i_m \qquad (4\text{-}13)$$

The number for different cases is calculated, as shown in **Figure 4.17**. When the He is small, the LMWs can be continually formed before they finally break due to gravity, enabling the successfully patterns around magnet (**Figure 4.17a**, He < 5 for all positions).

When *He* is large, the inertial of the LMWs becomes significant, resulting in the early fracture of the LMWs. As shown in **Figure 4.17b**, the lower fracture threshold value of *He* is found to be around 5 under current experiment conditions.
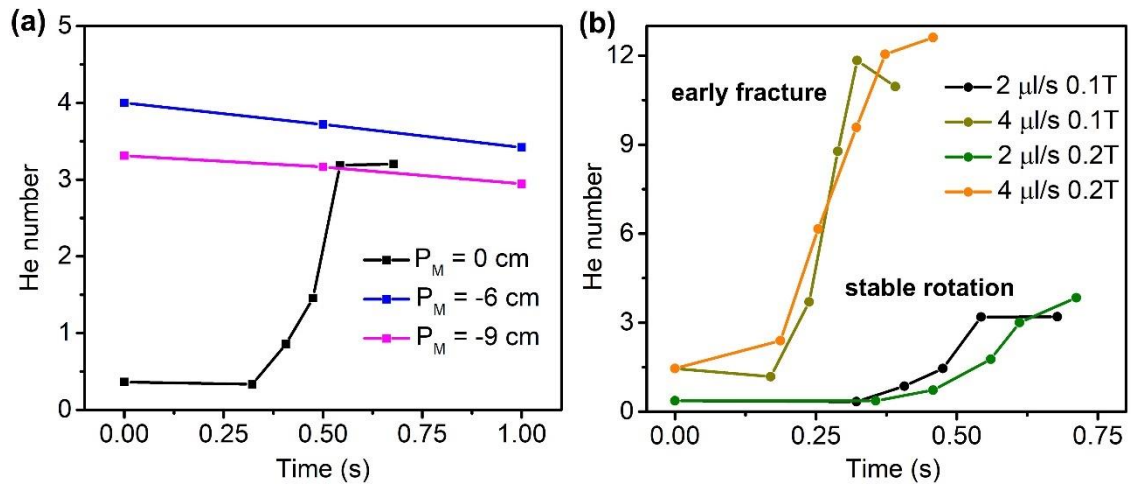
Figure 4.17. Calculated ration of inertial force and Lorentz force (*He*) when (a) magnet is placed at different positions, and (b) LMW is formed under different conditions with magnet placing at $P_M = 0$ cm.

4.4 Conclusion and Prospect

In summary, using only 1.5 V and a common magnet, the unique ability to steer free-flowing liquid metal wires in a non-contact manner into paths and suspended shapes was demonstrated. This enables fascinating effects including rotational motion, levitation, and acceleration. The electrical current passing through the LMWs enable me to connect the Lenz's Law effect, Lorentz force and gravity together, and to build a physical mode to analyses the dynamics of the LMWs. Lenz's law effect stabilizes the LMW pattern by controlling the current through LMW within a stable range. While Lorenz force rotates and accelerates the LMW, and the levitated LMW patterns are achieved by the force balance of Lorentz force and gravity. The transiently stable structures formed here could

be routes to build on this patterning method to stabilize the structures by either co-extruding a shell (e.g., polymeric material), cooling the receiving substrate (for solidification), or by curing the structures in a monomer solution (e.g., hydrogel). The findings are visually stunning and reveal previously hidden capabilities of such forces due to the use of soft (and highly conductive) liquid conductors, thereby enabling the patterning of useful metallic shapes and as a new strategy for shaping fluids in a non-contact manner.

Chapter 5. Screening Effect of Liquid Metal Droplets

5.1 Abstract

Room temperature liquid metals are known for their giant deformation property under application of voltage. This paper demonstrates an unusual deformation phenomenon of liquid metal droplets, which induces a Faraday cage-like screening effect. Such a screening effect is induced when a droplet deforms and surrounds the cathode, yielding a huge inner electric field within an electrical-double-layer to screen the external electric field. The screening effect protects the droplet or other droplets from further oxidation and contact with the cathode. Moreover, analogous contact inhibition behavior of multiple droplets triggered by the screening effect is observed. The droplets are arranged to arrive at the cathode at the same time (e.g., tilted substrate), and they come into contact with each other without merging and stop their deformation. Once they are separated by moving the cathode, the deformation process is restarted. The screening effect of liquid metal droplets may unlock a potential application in liquid systems, just as the analogous biological contact inhibition behavior enables new strategies for biochemistry and biophysics.

5.2 Observation of New Fluid Phenomenon Based on Screening Effect

Recently, liquid metals (LMs), especially gallium-based (Galinstan, the eutectic alloy of gallium indium and tin used in this work) LMs have received significant attention recently because of their multifunctional properties of soft and stretchable metallic conductors, microchannels, suitability for electrochemical manipulation and different printing methods, *et*.[2-3, 6-8, 10-11] The LMs are well known for their giant deformation property under application of a voltage in base/acid solution, leading to electrochemical oxidation of the surface of the LMs.[10, 25, 164] This electrochemical manipulation lowers the

effective interfacial tension and enables the deformation and fluidity of the LMs. Thus, various unique properties/behavior of LMs have been explored,[10-11, 25, 152-153, 158, 164-166, 181, 183] such as reversible deformation,[10] controllable locomotion,[152-153, 158] patterning,[165] heartbeat effects,[166] a "superfluid-like" penetration effect,[181] and liquid metal streams.[11, 183] The reversible deformation of liquid metal droplets (LMDs) is the first phenomenon of great concern. An LMD connected to an anode spread like the growth of a tree in NaOH solution under a DC voltage. There was also a previous report that irreversible deformation could be achieved by using an electrode wetted with liquid gallium, realizing simultaneous deformation and solidification.[164]

Meanwhile, most explorations were conducted in a free space (to avoid contact with the cathode) to investigate the deformation behavior or instabilities of LMs, none of which were designed to be carried out in a finite space. That is, to determine what happens when the LMDs move toward the cathode within an extremely close distance. The most intuitive view is that the LMs would easily come into contact with the cathode (copper electrode) due to the wetting property of the oxide surface (Ga_2O_3 layer) of LMDs,[88, 161, 184] resulting in a short circuit. The oxides accumulating on the surface increase the thickness of the surface oxide layer (up to hundreds of nanometers),[163] however, which significantly decreases the strength of the external electrical field within a short distance. In contrast, an electrical-double-layer (EDL) is induced by the distribution of ions at the LM/solution interface[25-26, 28, 119, 152] and has a thickness of a few nanometers,[185-187] forming a huge interior electrical field (typically with scale of ~10^7 V/cm under dozens of millivolts).[186] Once the LMD moves around the cathode within the EDL, the inner electrical field is expected to counter the external electrical field. Thus, the deformation and locomotion towards the cathode of the LMs should not be theoretically assumed to be a simple oxidation and wetting process. Instead, the behavior of the LMs is supposed

to be controllable and complicate, especially within the distance of EDL zone. New phenomena as well novel fluidic properties are expected to be observed.

In my work, the LMDs deform and move towards the cathode under different external voltages and electrode distances. For one LMD configuration, the LMD has no direct contact with the cathode when it arrives at cathode. Instead, the LMD bypasses the cathode and surrounds it without wetting. Then, no further oxidation of the LMD is observed, while the LM keeps flowing from anode to cathode until all the LM has left anode. The screening effect, which is induced by the mutual resistance of the external and internal electrical fields, is supposed to prevent the droplet from further oxidation and contact with cathode. In the multi-LMD configuration, the droplets compete to deform and move toward the cathode. Once one LMD arrives at the cathode, other LMDs stop their oxidation/deformation and are retracted to the anode as the one LMD surrounds the cathode. The screening effect counteracts the external electrical field outside the surrounding zone at the cathode. Moreover, when two LMDs are arranged to arrive at cathode at the same time, they remain in contact with each other without merging, while LMDs easily merge in NaOH solution. During the contact, their oxidation is terminated while they keep flowing from anode to cathode. Once one LMD leaves the anode and breaks, significant reactivated oxidation of the other LMD is simultaneously observed. This shows that the screening effect interacts with multi-LMDs. The oxidation can also be restarted for all LMDs by moving the cathode, which can be used to separate LMDs. This deformation process of LMDs, to some extent, is analogous to contact inhibition in cell biology, which may enable new strategies for biochemistry and biophysics.

5.3 Experimental Setup and Analysis of Screening effect

The LMDs were immersed in NaOH solution in a horizontal petri dish with anode

attached. The experiments were first conducted by using one LMD 1 cm in size, as shown in **Figure 5.1a**. Different distances (D) between the LMD and the cathode, as well as various external voltages were applied to investigate the deformation of the LMD under different voltages and electric fields (E). The experiments were conducted under relatively low voltage from 3 to 10.5 V, with the distance varying from 2 to 7 cm. Images of LMDs reaching the cathode under different conditions are presented to demonstrate the differences. With a fixed electric field of 1.5 V/cm, as in **Figure 5.1b**, the LMDs under low voltage (3 - 5 V) show directional locomotion towards the cathode with less fractals compared to the highly deformed tree-like shapes of LMDs subjected to high voltages (7.5 - 10.5V). In **Figure 5.1c**, however, when the voltage is fixed at 5 V, the LMDs moved in a similar direction as D increases from 2 cm to 7 cm with increased movement time (t). Surprisingly, the LMDs did not break as soon as they reached the cathode. **Figure 5.1d** (5 V with $D = 3.33$ cm) shows that the LMD further surrounds the cathode for a certain time until all LM leave the anode and break, indicating that no short circuit appears during the deformation process.
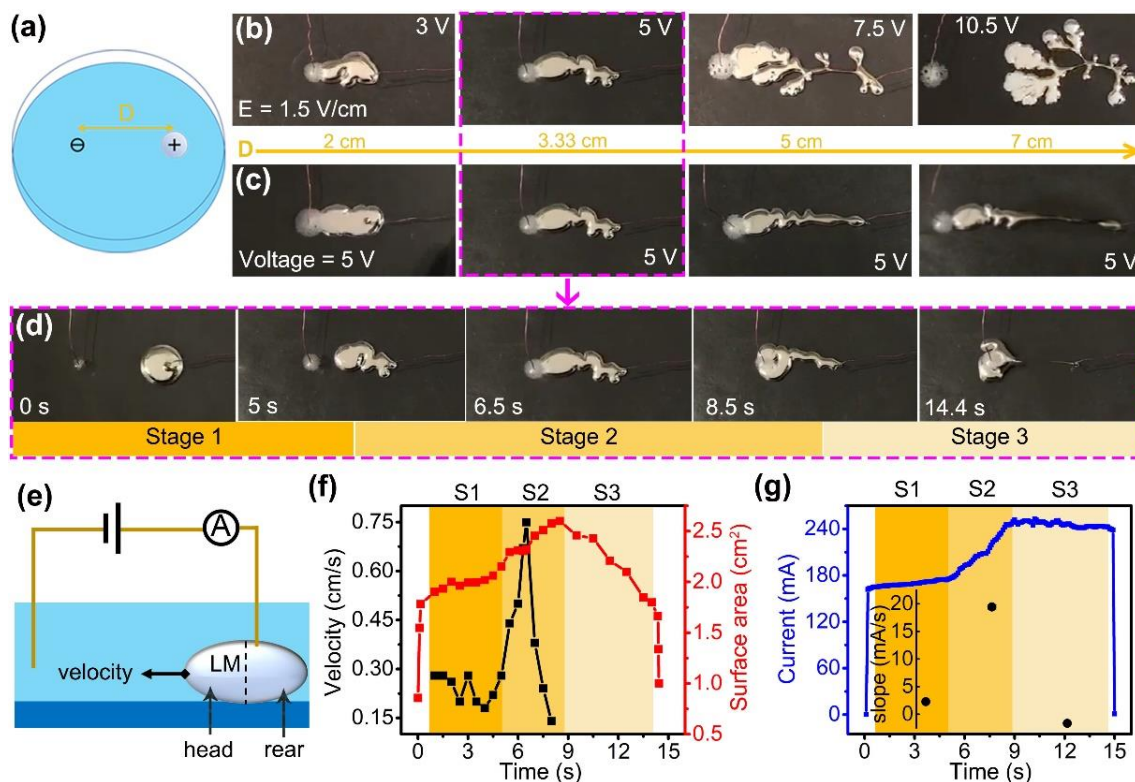
Figure 5.1. (a) The configuration of one droplet. D stands for distance between electrodes. Different deformations triggered by (b) voltages with fixed electric field of 1.5 V/cm, and (c) electric fields with fixed voltage of 5 V. (d) the deformation over time of one liquid metal droplet, under voltage of 5 V and electric field of 1.5 V/cm. (e) Illustrated motion and equivalent circuit of the droplet. (f) Changes of velocity, surface area size, and (g) electrical current of the droplet over three stages.

The deformation of the LMD in **Figure 5.1d** is divided into three stages based on the calculated velocity of the head of the LMD (illustrated in **Figure 5.1e**). At stage 1 (S1), the LMD moves toward the cathode at a low velocity of around 0.25 cm/s (black curve in **Figure 5.1f**). At stage 2 (S2), the LMD accelerates to the maximum velocity of 0.75 cm/s as it reaches the cathode at time, $t = 6.5$ s. Then, the LMD further moves around the cathode with decreased velocity. At $t = 8.5$ s, the head of the LMD stops and surrounds the cathode. At stage 3 (S3), the LMD keeps flowing from anode to cathode until the rear

of the LMD breaks at the anode at t = 14.4 s. The LMDs under different voltages and electric fields were observed to show the same trend of velocity change. That is, the velocity of the LMD undergoes significant acceleration near the cathode at stage 2. Moreover, the increase of surface area of the LMD (red curve in **Figure 5.1f**) is also more significant at stage 2 compared to the increase at stage 1. Then, the surface area of the LMD quickly decreases as the LM keeps flowing instead of deforming at stage 3. The changes of the velocity and surface area are induced by decreasing the interfacial tension (γ) of the LMD with electrochemical surface oxidation reduced to an extremely low value. Meanwhile, a significant electrical current (I) arises from the electrochemical oxidation, as shown in **Figure 5.1g**. The electrical current slowly increases from 162 to 175 mA (t = 5 s) at stage1 (with a slope factor of 2.3 in the **Figure 5.1g** inset), while the current changes to rapid growth to 245 mA (t = 8.5 s) at stage 2 with a slope factor of 20. The changes in the current in stage 1 and stage 2 correspond to the surface area change. The current does not decrease as dramatically as the surface area does at stage 3. The current slowly decreases with a slope factor of -1.6. To date, the value of current is a constant value of about 70 mA without the LMD under the same conditions (5 V, D = 3.33 cm).

The current change in stage 3 is unexpected, as the current originates from the surface oxidation: $Ga \rightarrow Ga^{3+} + 3e^-$, so the value of the electrical current is always considered highly dependent on the size of surface area.[183] The change in the deformation and electrical current changes can be attributed to interfacial tension gradients induced by local potential gradients, which is also known as Marangoni flow,[188-189] as shown in **Figure 5.2a**. In the absence of an external power, reactions between the LM and the NaOH solution slowly produce negative charges (like [Ga(OH)$_4$]$^-$), making the LM negatively charged with the surface positively charged (first image in **Figure 5.2a**). The equilibrium shape of LM is controlled by the balance between the pressure due to gravity

$(P_g = \rho g h)$ and interfacial tension $(P_L = \gamma \frac{2}{R})$, where P_g is the gravity induced pressure, ρ is the density of the LM, g is the gravitational acceleration, h is the height of the gravity center, P_L is the interfacial-tension-induced Laplace pressure, γ is the interfacial tension, and R is the radius of the curvature at the edge of the LM. Once an anodic potential is applied, the charges on the surface alter from positive to negative (second image in **Figure 5.2a**). With external voltage of 5 V, an oxide layer of Ga_2O_3 is formed on the surface, and such surface oxides are known to lower the interfacial tension of the LM. As a result, the LM becomes flat immediately due to gravity ($P_g = P_L$, decrease in h and increase in R). Moreover, an imbalanced charge distribution is also induced, triggering the deformation and propelling the LM towards the cathode. More oxides are formed on the head part compared to the rear part of the LM, leading to smaller interfacial tension at the head. Thus, the surface oxides as well as electrons flow from the head to the rear, forming a Marangoni flow on the surface (third image in **Figure 5.2a**). Meanwhile, the interfacial gradient on the surface generates larger Laplace pressure on the rear (compared to pressure of the head part). The pressure difference drives the interior part of the LM to flow from the rear to the head. As the head surrounds the cathode, directional locomotion with decreased fractals of the rear is observed, indicating the reduced oxidation reaction on the surface of the rear at stage 2. Considering the stable value of electrical current at stage 3, the surface oxidation might only occur at the head part surrounding the cathode, with negligible oxidation on the surface of the rear at stage 3. The ions in solution are distributed within the extremely short distance between the LMD and the cathode (fourth image in **Figure 5.2a**), which yields an opposite interior electric field screening the external electric field, leading to the 'screening effect' on the rear part of the LMD.

Figure 5.2. (a) Surface charge distributions and motion analysis of the liquid metal droplet. (b) Equivalent circuit of the experimental setup: C_A and R_A are the electrical-double-layer capacitance and the charge transfer resistance between the liquid metal and the solution; C_C and R_C are the electrical-double-layer capacitance and charge transfer resistance between the copper electrode and the solution; R_E is the resistance of the electrolyte. The electrical-double-layer is divided into two subregions: the inner compact layer (CL) and the outer diffuse layer (DL). (c) Illustration of the charge distributions, and (d) the potential drop across the liquid metal and the copper electrode.

The distribution/redistribution of surface charge at the LMD/solution or electrode/solution interfaces forms an EDL. These EDLs determine the potential drop at the interfaces and are connected in series in the experimental setup, which controls the motion of the LMD. An equivalent circuit is introduced for the mechanism analysis, as shown in **Figure 5.2b**. C_A and R_A are the EDL capacitance and charge transfer resistance between the LMD and the solution; C_C and R_C are the EDL capacitance and charge transfer resistance between the copper electrode and the solution; R_E is the resistance of the electrolyte. Based on the Gouy-Chapman-Stern model, the EDL comprises an immobile compact layer (CL) and a mobile diffuse layer (DL).[186-187, 190-191] Meanwhile, a gallium oxide layer (OL) also forms at the anode, as shown in **Figure 5.2c**. As these layers

are connected in series, the EDL capacitance is calculated as follows:

$$C_A^{-1} = C_1^{-1} + C_{ACL}^{-1} + C_{ADL}^{-1} \qquad (5\text{-}1)$$

$$C_C^{-1} = C_{CCL}^{-1} + C_{CDL}^{-1} \qquad (5\text{-}2)$$

where C_{ACL} and C_{ADL} are the capacitances of the CL and DL at the LMD/solution interface, C_1 is the capacitance of the gallium oxide layer, C_{CCL} and C_{CDL} are the capacitances of the CL and DL at the copper electrode/solution interface. The corresponding potential drops of these layers are shown in **Figure 5.2d**, where φ_0, φ_1, φ_d, and φ_z is the potential of anode, OL, CL (known as the Stern potential), and DL (known as the Zeta potential), respectively.

Quantitative characterization of the capacitance and potential drop at the anode was done for the special OL formed at the anode, as shown in **Figure 5.3**. The capacitance of the OL could be expressed as a parallel plate capacitor:

$$C_1 = \frac{\varepsilon_0 \varepsilon_1}{d_1} \qquad (5\text{-}3)$$

where ε_0 is the permittivity of vacuum ($8.854 \times 10^{-12} C^2/(N \cdot m^2)$), and ε_1 (~10) and d_1 are the relative permittivity and the thickness of the Ga$_2$O$_3$. The value of d_1 increases as the LM moves toward the cathode with as more oxides are formed. To estimate the thickness of the OL, Faraday's law of electrolysis was employed:

$$m = \frac{Mq}{Fz} = \frac{M}{Fz} \int I(t)dt \qquad (5\text{-}4)$$

where m is the mass of gallium oxide, M is the molar mass of gallium oxide (187.44 g/mol), F is the Faraday constant (96487 C/mol), z is the valence of Ga^{3+} ($z = 3$), and $I(t)$ is the current as a function of time. To date, the value of $I(t)$ is equal to the measured value of current minus the value of the current without liquid metal (~ 70 mA). Thus, the moles of Ga^{3+} are:

$$n = \frac{m}{M} = \frac{\int I(t)dt}{Fz} \qquad (5\text{-}5)$$

and the oxidation rate (R_O) is estimated as follows:

$$R_O = \frac{n}{A_O \Delta t} \tag{5-6}$$

where A_O is the surface area. As liquid metal is ultra-flat when it moves toward the cathode, I treat the liquid metal as a 2-layer structure. That is, the value of A_O is double the statistical value of the surface area. Moreover, the dissolution rate (R_D) can be estimated by measuring the current and surface area when the liquid metal droplet becomes a disk-like shape in the equilibrium state (without directional motion). This equilibrium state is realized by the balance of oxidation/dissolution rate:

$$R_D = R_{O,\ equi} = \frac{n_{equi}}{A_D \Delta t} \tag{5-7}$$

where $R_{O,\ equi}$ is the oxidation rate in the equilibrium state. The equilibrium shape is obtained with external voltage of 1V (constant current of about 40 mA), and n_{equi} represents the moles of Ga^{3+} formed under this current. This equilibrium shape of the liquid metal is regarded as a 3D cylinder, and thus the total surface area A_D is estimated as follows:

$$A_D = 2S + 2h\sqrt{\pi S} \tag{5-8}$$

where S is the measured top surface area ($S = 1.5\ cm^2$) and h is the height of liquid metal ($h \sim 0.2\ cm$). The calculated values of R_O and R_D are shown in **Figure 5.3a**. The value of R_O is relatively stable at stages 1 and 2, but it goes up almost in an exponential manner in stage 3, while the value of R_D is assumed to be a constant value throughout the motion of LMD. From these values, the thickness of the gallium oxide is estimated by:

$$d_1(t) = \frac{M}{\rho} \int_0^t (R_O - R_D)dt \tag{5-9}$$

Where ρ is the density of the gallium oxide (6.44 g/cm^3). This estimated value is the average thickness across the surface, while the experimental observations and previous reports indicate that the layer is thicker in areas closer to the cathode. As shown

in **Figure 5.3b,** the thickness of the OL increased almost linearly from monolayer (~ 1 nm) to 100 nm at $t = 8.5$ s (the end of stage 2). Then, the thickness of the OL soared to 500 nm at the end of stage 3 due to the decreased size of the surface area.
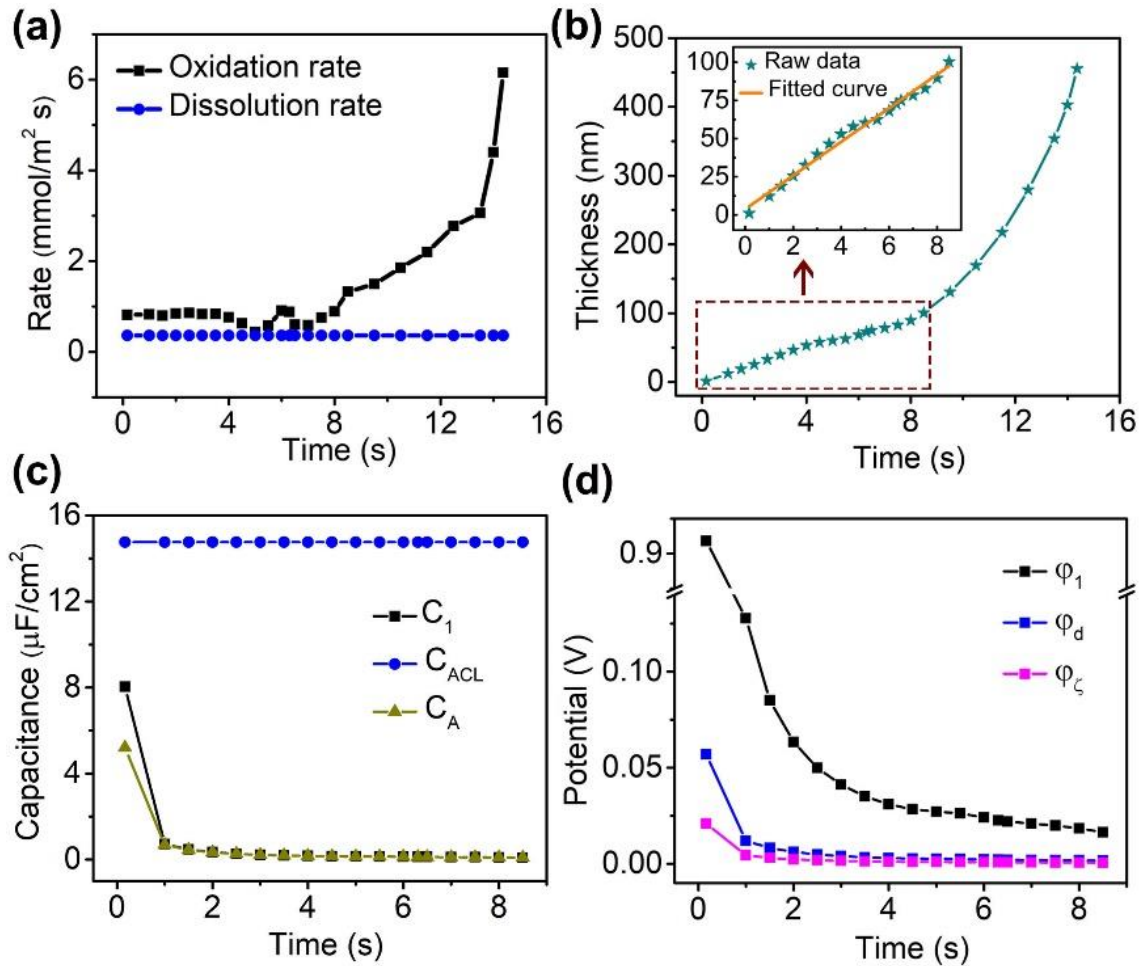
Figure 5.3. Quantitative characterization of the capacitance and potential drop at the anode. **(a)** oxidation rate and dissolution rate of liquid metal droplet as it moves toward the cathode. **(b)** The corresponding thickness change of the oxide layer, with the inset showings the thickness and corresponding linear fitted curve from 0 to 8.5 s. **(c)** The changes of capacitance and **(d)** potential within the layers in stages 1 and 2.

The thickness of the OL from stage 1 to the end of stage 2 to can be used to characterize the changes in capacitance and potential drop, as the LMD completely

127

surrounds the cathode at the end of stage 2. The value of C_1 decreases from 8.854 to 0.11 $\mu F/cm^2$. Meanwhile, the capacitance of CL could be also expressed as analogous to a parallel plate capacitor:

$$C_{ACL} = \frac{\varepsilon_0 \varepsilon_2}{d_2} \tag{5-10}$$

where ε_2 and d_2 are the relative permittivity and the thickness of the compact layer (also known as the Stern layer). The calculated values of C_{ACL} is 14.76 $\mu F/cm^2$. For the DL, the Poisson-Boltzmann equations are introduced to calculate the capacitance:[190]

$$C_{ADL} = \sqrt{\frac{2\varepsilon_0 \varepsilon_s z^2 F^2 c_0}{RT}} \cosh\left(\frac{zF\varphi_d}{2RT}\right) \tag{5-11}$$

where ε_s is the permittivity of the bulk solution (~70), z is the valence of cations and anions, F is the Faraday constant, c_0 is the concentration of the bulk solution (1000 mol/m³), R is the gas constant (8.314 J/(mol·K)), and T is the absolute temperature (~300 K). The equation could be simplified when the value of φ_d is small (scale of millivolt):

$$C_{ADL} = 2.15 \cosh(19.34\varphi_d) \geq 215 \, \mu F/cm^2 \gg C_{ACL} > C_1$$

Considering that these equivalent capacitances are connected in series, the value of C_{ADL} has a negligible effect on C_A. Thus, the value of C_A is mainly dependent on the values of C_{ACL} and C_1:

$$C_A \approx C_2 = \left(\frac{1}{C_1} + \frac{1}{C_{ACL}}\right)^{-1} = \frac{\varepsilon_0 \varepsilon_1 \varepsilon_2}{d_1 \varepsilon_2 + d_2 \varepsilon_1} \tag{5-12}$$

C_1 quickly becomes the dominant capacitance as the OL grows thicker, as shown in **Figure 5.3c**. The potential drops within OL and CL are expressed as:

$$\varphi_0 - \varphi_1 = \frac{\sigma d_1}{\varepsilon_0 \varepsilon_1} \tag{5-13}$$

$$\varphi_1 - \varphi_d = \frac{\sigma d_2}{\varepsilon_0 \varepsilon_2} \tag{5-14}$$

where σ is the charge density. The potential within DL is highly dependent on the potential of OL:[187]

$$\varphi_{\zeta(x)} = \frac{2RT}{zF} \ln \frac{e^{kx} + \tanh \frac{zF\varphi_d}{4RT}}{e^{kx} - \tanh \frac{zF\varphi_d}{4RT}} \tag{5-15}$$

$$k = \sqrt{\frac{2z^2 F^2 c_0}{\varepsilon_0 \varepsilon_s RT}} \tag{5-16}$$

where $\varphi_{\zeta(x)}$ is the potential of the diffuse layer, $1/k$ (known as the Debye Length: $\lambda = 1/k$) is usually defined as the thickness of the diffuse layer, and R is the gas constant, while x is the distance to the inner surface of the diffuse layer. The equation of φ_ζ could be simplified for small value of φ_d:

$$\tanh \frac{zF\varphi_d}{4RT} \approx \frac{zF\varphi_d}{4RT} \tag{5-17}$$

Thus, φ_ζ is expressed as:

$$\varphi_{\zeta(x)} = \varphi_d e^{-kx} \tag{5-18}$$

When $x = \lambda = 1/k$, the value of the Zeta potential can be derived:

$$\varphi_\zeta = \frac{\varphi_d}{e} \tag{5-19}$$

Where e is the natural logarithm (≈ 2.71828). The potential drop within DL is:

$$\varphi_d - \varphi_\zeta = \frac{e-1}{e} \varphi_d \tag{5-20}$$

As the LMD moves towards the cathode, the ions are pushed within the shortened distance between the LM and the cathode. Thus, the values of φ_1, φ_d, and φ_ζ are dynamic. An approximate relationship is built to estimate these values by approximating the diffuse layer as a parallel plate capacitor:

$$C_{ADL} = \frac{\sigma}{\varphi_d - \varphi_\zeta} = 2.15 \cosh(19.34\varphi_d) \tag{5-21}$$

$$\sigma = \frac{(\varphi_0 - \varphi_d)\varepsilon_0 \varepsilon_1 \varepsilon_2}{d_1 \varepsilon_2 + d_2 \varepsilon_1} \tag{5-22}$$

The external voltage between the anode and cathode is 5 V, and the potential at the anode (φ_0) is +2.5 V for symmetric system. Thus, I have:

$$C_{ADL} = 2.15 \cosh(19.34\varphi_d) = \frac{\varphi_0 - \varphi_d}{(10d_1 + 6) \times 0.7138\varphi_d} \tag{5-23}$$

The potential changes at the interfaces of layers are shown in **Figure 5.3d**. These potentials decrease dramatically once the OL is formed, and they continue to decrease slowly as the thickness of the OL increases. The potential drop through the OL increases from 1.58 to 2.48 V, while the potential drop through the CL and DL decreases from 0.89 V to 16 mV. The capacitance and potential drop finally depend on the thickness of the OL, which indicates that the oxidation process on the surface dominates the motion of the LMD. As the LMD get very close to the cathode at $t = 8.5$ s (distance within CL and DL), however, the electrostatic effect of charges in solution emerges. This effect forms a counter electrical field against the external electrical field, and stops the motion of the LMD. Under this critical condition, the external electrical field is estimated as:

$$E_{EX} = \frac{\varphi_0}{d_{1, \ t=8.5s}}$$ (5-24)

where $d_{1, \ t=8.5s}$ is the thickness of the OL at $t = 8.5$ s. The calculated scale of E_{EX} is about 2.5×10^7 V/m, and it keeps decreasing to about 5×10^6 V/m as d_1 increases to 500 nm at $t = 14.3$s. And the inner counter electrical field is estimated as:

$$E_{IN} = \frac{\varphi_1 - \varphi_\zeta}{d_2 + \lambda}$$ (5-25)

Where λ is the Debye Length with calculated value of 0.3 nm, the value of $\varphi_1 - \varphi_\zeta$ is about 16 mV at $t = 8.5$ s. The calculated scale of E_{IN} is about 1.8×10^7 V/m. Thus, the external electrical field decreases as the thickness of OL increases, and it is increasingly electrically screened by the inner electrical field within CL and DL. Which forms the 'screening effect' on the rear part of the LMD with decreased oxidation.

Figure 5.3 shows that the capacitance and potential drop are strongly depends on the thickness of the OL, while the thickness of the OL is determined by the electrical current. This indicates that the electrical current could be treated as an important clue for analyzing the deformation/motion of the LMDs under different external voltages/electrical fields. As shown in **Figure 5.4**, the measured currents under different

conditions go through three similar stages that change within the distance from 2 to 5 cm. that is, slowly increase in stage 1, dramatically increase in stage 2, and hold a stable value or slightly decrease in stage 3. For the distance of 7 cm, the LMDs are unable to reach up to the cathode, so only the slow increase of the LMD in this stage is observed.
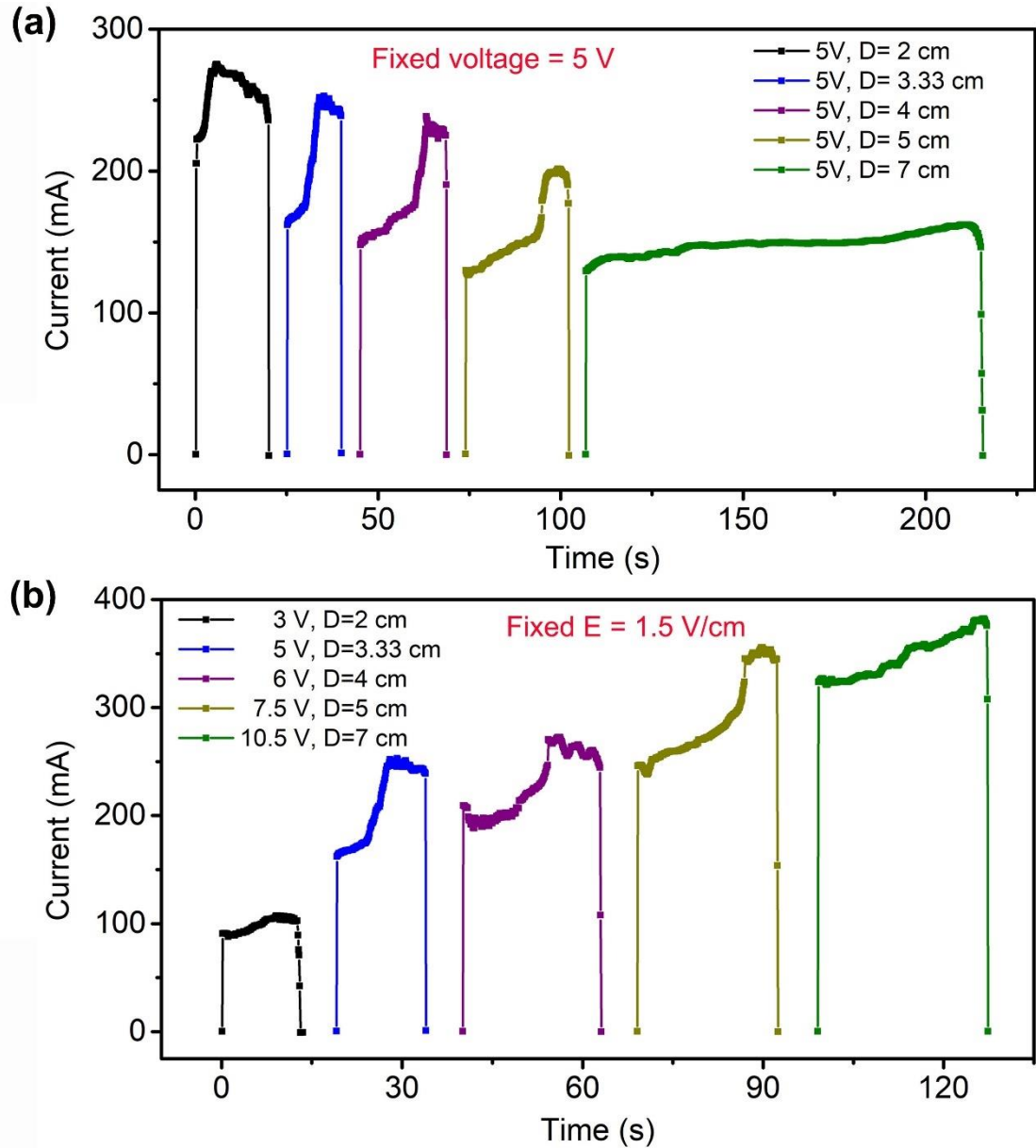
Figure 5.4. The measured electrical currents under different conditions. (a) fixed external voltage of 5 V. (b) Fixed electric field of 1.5 V/cm.

The corresponding statistical values of the currents under different conditions are shown in **Figure 5.5**. With fixed voltage of 5 V, the currents at each stage decrease with distance (initial electrical field decrease from 2.5 to 0.7 V/cm), while with initial electrical field fixed at 1.5 V/cm, the currents at each stage increase with distance (external voltage increase from 3 to 10.5 V), as shown in **Figure 5.5a**. The magnitude difference of the decrement/increment of current at each stage indicates that the external voltage plays a more significant role during the deformation. The slopes of the curves for the electrical currents at each stage were also calculated, as shown in **Figure 5.5b**. At stage 1, all the slopes of electrical current increase with external voltage or initial electrical field on the same scale, while the value of the slope increases more significantly with increasing voltage than increasing electrical field at stage 2. The difference in the slope change might be attributed to the different driving forces at stages 1 and 2, since the electrical current increases with surface area at these two stages. At stage 1, the motion of the LMD is mainly driven by the difference in the interfacial tension, because the OL dramatically reduces the interfacial tension to an extremely low value (scale of 10^{-5} mN/m) once the external voltage exceeds the critical value (~1 V for the equilibrium state). Thus, the interfacial tension of the LMDs under different conditions (voltage $\geq$ 3 V) is on the same scale, and so is the driving force. This can be verified by the similar velocities of the LMDs under different conditions at stage 1, with a value of about 0.2 cm/s. When the LMDs move closer to the cathode at stage 2, the electric field force, which is derived from the increasing external electric field, starts to play a more influential role, and finally becomes the dominant driving force before the external electric field is electrically screened by the inner electrical fields within the CL and DL, which leads to the surge in the values of velocity and current in stage 2. The slope change under different conditions at stage 2 is influenced by the external electric field. At stage 3, the values of slopes are

small and remain stable near zero, indicating that the 'screening effect' prevents the LM from further oxidation.
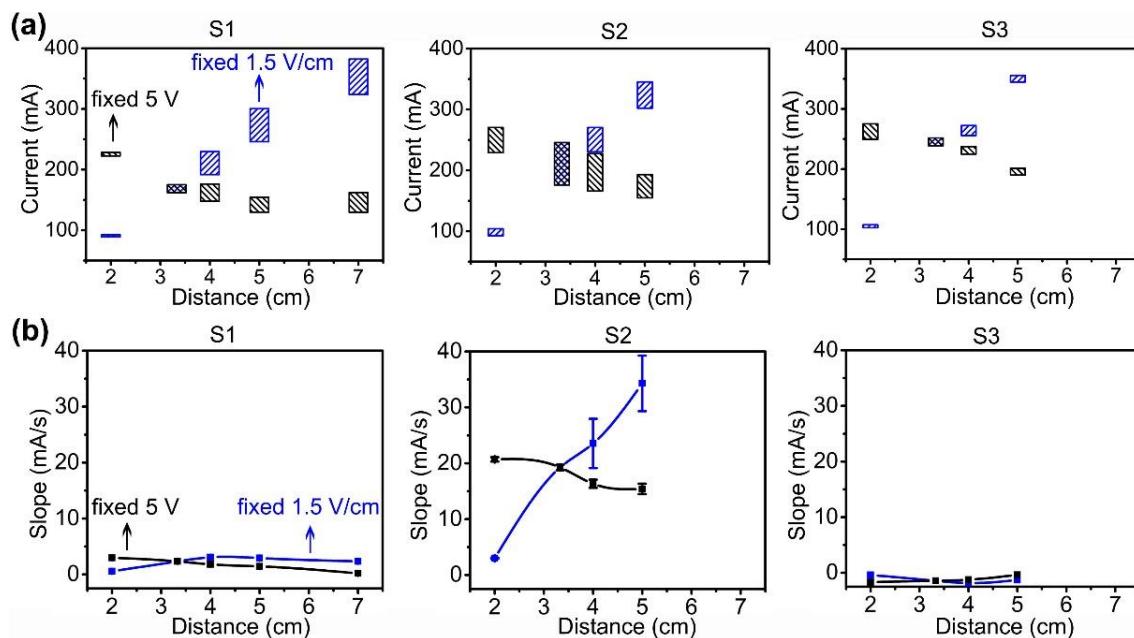
Figure 5.5. (a) Statistical data and (b) calculated curves for the slopes of the electrical current changes at each stage under different experimental conditions.

To furtherly demonstrate the unique deformation and 'screening effect' of the LMD, more experiments were conducted with multi-LMDs. As shown in **Figure 5.6a**, two LMDs are both connected to the anode (5 V) with the same distance to cathode ($D =$ 3.33 cm). The time-evolution images of the deformation of the two LMDs are shown in **Figure 5.6b**. Once the external voltage is applied, the two LMDs become flat immediately and start to deform. These two LMDs compete as they move toward cathode, during which one LMD wins the competition and moves faster toward the cathode (the left LMD in my case). When the faster one arrives at the cathode, the deformation of the slower one is retarded. As the faster one surrounds the cathode from $t = 9.9$ to 18.4 s, the slower one even retracts to the anode, indicating the decreased oxidation of the slower

LMD. Once the faster one leaves the anode, the faster one comes into contact with the cathode and becomes a part of cathode at $t = 19.3$ s. Meanwhile, the slower one immediately spreads out with dramatic deformation. To reveal the underlying mechanism of this unique motion, the electrical currents were measured, as shown in **Figure 5.6c** and **d**. A_1 and A_2 represent the electrical current of the faster LMD and slower LMD, respectively. During the competition stage, the values of A_1 and A_2 are stable, and the value of A_1 is slightly larger than that of A_2. When the faster LMD starts to surround the cathode, the value of A_1 significantly increases from 165 to 270 mA, while the value of A_2 gradually decreases from 145 to 60 mA (equivalent to the slower LMD with oxidation voltage of about 1.3 V). Then, the values of A_1 and A_2 remain constant until the faster LMD breaks from the anode, at which the value of A_1 immediately drops to nearly zero, while A_2 simultaneously increases to an extremely high value. Moreover, the statistical data on the surface areas of these two LMDs demonstrate a similar change with the electrical current, as shown in **Figure 5.6e**. The deformation and the electrical current changes of the faster LMD are the same as with one LMD. When the faster LMD fully surrounds the cathode, the electrical current does not decrease with surface area, also indicating the 'screening effect' on the rear part of the faster LMD. Most importantly, the slower LMD retracts to the anode with decreasing electrical current as the faster LMD surrounds the cathode, which fully confirms the 'screening effect' (induced by the faster LMD) on the slower LMD. This is convincing evidence that, once the LMD fully surrounds the cathode, the surrounding LMD blocks the external electrical field like a Faraday cage, forming the 'screening effect' outside the blocking zone. This unique deformation process and the 'screening effect' are also observed for a three-LMD experimental setup.
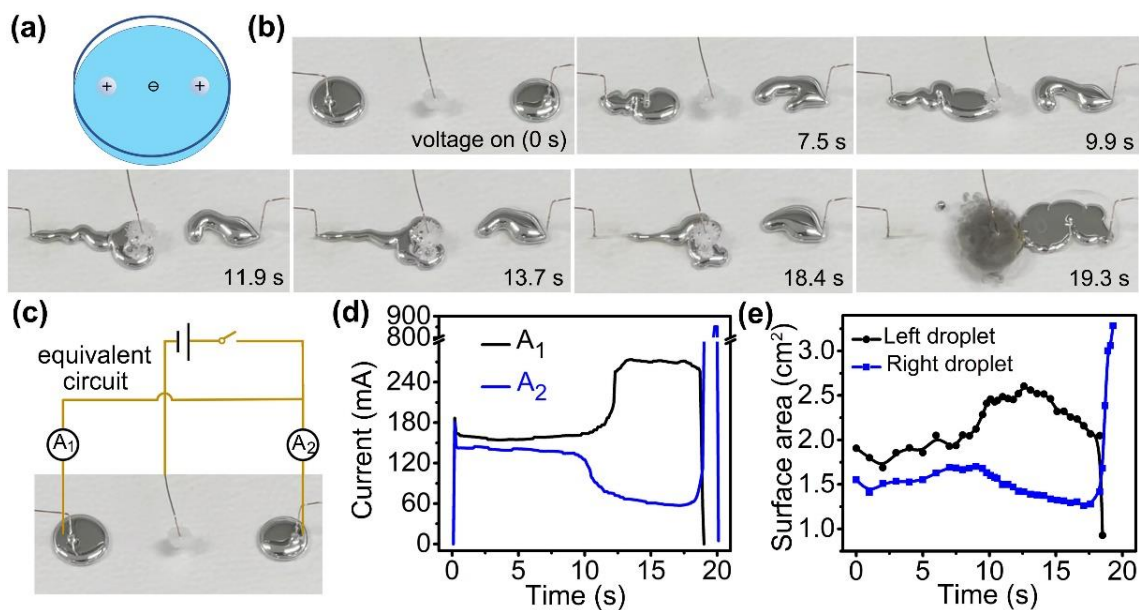
Figure 5.6. (a) The configuration of the two droplets. (b) Photographs show the deformation of the two liquid metal droplets. (c) Equivalent circuit of two droplets system for the measurement of electrical current. (d) The electrical current and (e) the changes in surface areas of the two liquid metal droplets.

Moreover, when the two LMDs are arranged to arrive at the cathode at almost the same time (e.g., the right side of petri dish is slightly tilted, as shown in **Figure 5.7a**), the observed experimental phenomenon is different. The photographs in **Figure 5.7b** show that, as the two LMDs meet each other at the cathode at $t = 8.3$ s, no further oxidation of either LMD is observed. On the contrary, the surface areas of the two LMDs both decrease. Neither of them shows significant oxidation surrounding the cathode nor retraction to anode like the two LMDs in **Figure 5.6**. The head parts of the two LMDs remaining contact with each other, while the rear parts of the two LMDs keep flowing to the heads, until the left droplet completely leaves the anode and breaks into a spherical structure at $t = 11.67$ s. Significant oxidation of the right LMD is observed simultaneously. This process is the result of the mutual influence of the 'screening effect' of the two LMDs, during which the two LMDs stop further oxidation and touch each

135

other without merging. They can be easily separated by moving the cathode, however, and then their deformation is reactivated, as shown in **Figure 5.7c**. The two LMDs deform and follow the cathode, and they can be controlled to touch/separate from each other by adjusting the position of the cathode. The deformation process of the two LMDs is analogous to the contact inhibition of cell growth,[192-193] and they stop deforming/growing once they are in contact. The cathode plays the role of 'energy' for the cell, and the two LMDs chase the cathode for deformation energy. The LMDs regain the ability to deform/grow once they are separated by the moving cathode. This unique behavior is also observed for the multi-LMD experimental setup with moving cathode. The 'screening effect' induced analogous contact inhibition behavior might unlock the potential biological applications of multi-LMDs.
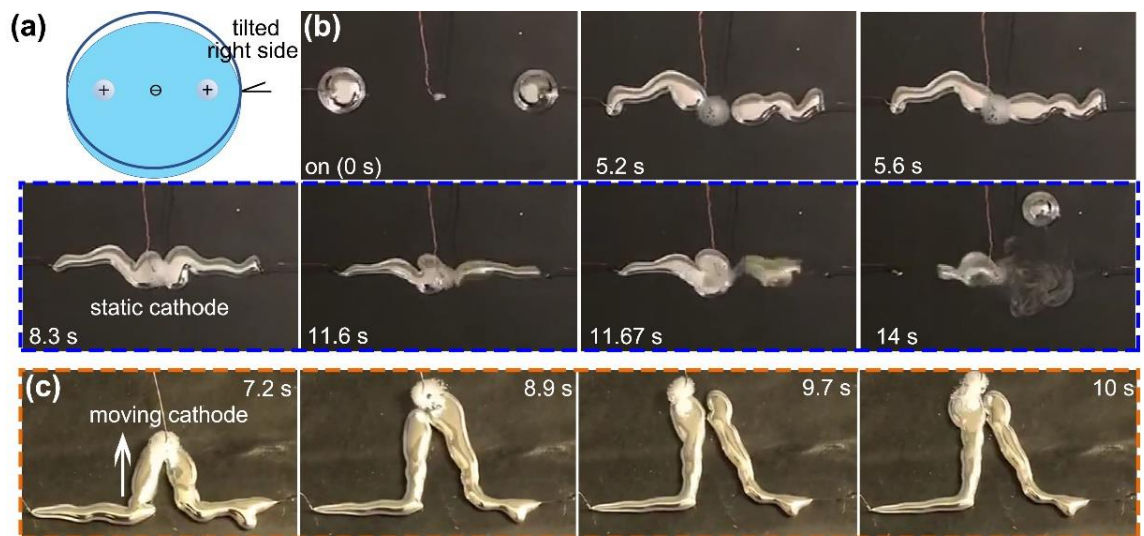
Figure 5.7. (a) The configuration when the right side of the petri dish is tilted. (b) The images show that the two droplets arrive at the static cathode at almost the same time with different deformation behavior. (c) The two droplets are manipulated (contact/separated) by the moving cathode.

5.4 Conclusion and Potential applications

In this work, a novel deformation phenomenon of liquid metals has been demonstrated, and the potential applications were also explored. The liquid metal droplet unexpectedly surrounds the cathode without merging during the deformation process. This behavior yields a huge inner electrical field and forms a screening effect within the distance of the electrical-double-layer, which prevents the droplet or other droplets outside the screening zone from undergoing further oxidation. Moreover, the interplay of the screening effect within multi-droplets was also observed by arranging the droplets so that they arrived at the cathode at the same time. The droplets remained in contact with each other without merging and stopped the oxidation process, which is analogous to contact inhibition in cell biology. The oxidation was restarted when the droplets were separated by moving the cathode. This unique screening effect expands the potential application of liquid metal in a liquid system, and could be regarded as mimicking the biological motion.

Chapter 6. Controllable Heartbeat Effect of Liquid Metal

6.1 Abstract

Fluid oscillations have great importance in both fundamental research and practical applications. How to control the oscillations and realize regular motion has been attracting intensive attention. In previous work, the regular heartbeat effect of liquid metal was achieved by shape shifting with a voltage simulation. In this work, the experimental setup is modified for easier implementation. The heartbeat effect of liquid metal droplets with different sizes is stimulated by a small voltage of 1.5 V with various electrode positions. A beating factor k, the ratio of the height to the diameter of droplets, is defined to characterize the periodic process within the balance between gravity and interfacial tension. This work optimizes the heartbeat effect of liquid metal and provides a fundamental insight into beating process, as well as enabling potential fluidic and bionic applications, such as liquid actuators/pumps and soft robots.

6.2 Importance and Realization of Controllable Heartbeat Motion

Liquid motion is common in daily life, and how to control the liquid motion has long been important in engineering, fluid dynamics applications and other fundamental research.[194-197] Liquid shows directional locomotion in designed channels or surfaces,[198] and acoustical/electrical/magnetic/optical methods are also applied to control the liquid motion.[199-207] Among these methods, electrochemical/chemo-mechanical manipulation is a high effective method with low cost to control liquid motion, especially when the surface properties of the liquid are adjustable.[208-210] The liquid motion can be easily controlled by changing the surface state. In this context, liquid metal (LM), metallic fluid, is attracting intensive attention due to its unique interfacial properties for controllable motion with electrochemical manipulation.[8, 10, 25, 44, 163]

LMs, especially gallium based LMs (gallium, indium gallium alloy, and galinstan), are cutting-edge materials with promise for soft composite structures,[2, 92, 102, 211-213] micro-fluids,[35, 44, 154] core-shell structures,[14, 20] and biological applications,[124, 214] due to their unique properties combining conductivity, fluidity, and low toxicity. Moreover, the oxide layer, which can be dissolved either in acid or base solution,[28, 154] can be electrochemically manipulated, leading to various novel fluidic phenomena.[164-166, 181] Among these, the heartbeat effect,[166] the periodic beating motion of a liquid metal droplet (LMD) with a voltage stimulation, is eye-catching due to its potential applications in fluid-based timers, actuators, and bionics.

Unlike the chaotic beating of mercury (high toxicity), the periodic beating of LM is controllable. Here, in this work, the heartbeat effect of LMDs is demonstrated with different sizes stimulated by a small voltage of 1.5 V (low energy consumption) with various electrode positions. The LMD deforms from spherical to another shape and recovers periodically during the beating process. The beating frequency, which is related to different shapes of LMD, is controllable from 2 to 6 Hz. The underlying beating mechanism is the dynamic balance between the electrochemically manipulated interfacial tension and gravity. A shape-related beating factor, which is the ratio of the height to the diameter of LMD, is defined as k, where the height and diameter stands for gravity and interfacial tension, respectively. This work provides a fundamental way to understand the shape-related heartbeat effect of liquids, and enables potential fluidic and bionic applications, such as liquid actuators/pumps and soft robots.

6.3 Optimized Experimental Setup and Heartbeat Process

The LMD is immersed in NaOH solution in a horizontal petri dish, confined by an insulator, as illustrated in **Figure 6.1a**. The anode is attached to the top of the LMD while

the cathode is placed in NaOH solution with a distance of 5 cm between electrodes. Periodic beating of the LMD is observed under external voltage of 1.5 V. When the anode touches the LMD, the LMD moves downward and leaves the anode instead of merging with the anode. Then, the LMD moves back to its initial position and come into contact with the anode, forming the periodic beating. The underlying mechanism is that when the LMD touches the anode, electrochemical oxidation takes place on the surface of the LMD, resulting in the decrease of its interfacial tension (γ) of LMD. The equilibrium shape of LMD is achieved by the balance between gravitational pressure ($P_g = \rho g h$) and the Laplace pressure induced by interfacial tension ($P_L = \gamma \frac{2}{R}$), where P_g is the gravity induced pressure, ρ is the density of the LM, g is the gravitational acceleration, h is the height of the center of gravity, P_L is Laplace pressure induced by the interfacial tension, γ is the interfacial tension, and R is the radius of curvature at the edge of the LM. The value of the Laplace pressure decreases with the interfacial tension. Thus, the value of the gravitational pressure also decreases to reach a new balanced state, which manifests as a decreased value of the height (h) of the droplet. When the LMD leaves the anode, the surface oxides dissolve in NaOH, and the interfacial tension is then recovered. As a result, the LMD bounces back to the anode, as shown in **Figure 6.1b**. The movements of the LMD are cyclic with a specific frequency, which forms the periodic heart-beating effect. **Figure 6.1c** shows front-view images of the LMD and anode. The vertical cylinder part is the fixed anode, while the moving surface is the top of the LMD. The LMD comes into contact with and separates from the anode without any merge observed. **Figure 6.1d** shows top-view images of the experimental setup, the ring surrounding the LMD is the insulator confining. The LMD retains its spherical shape with changing diameter during the beating process. The LMD expands with increasing diameter when it leaves the anode, while the LMD shrinks with decreasing diameter when it bounces back to the anode.

Moreover, a groove on the top of the LMD is observed as the LMD bounces back, indicating that the moving LMD exceeds the original height of the LMD at the initial stage without voltage.
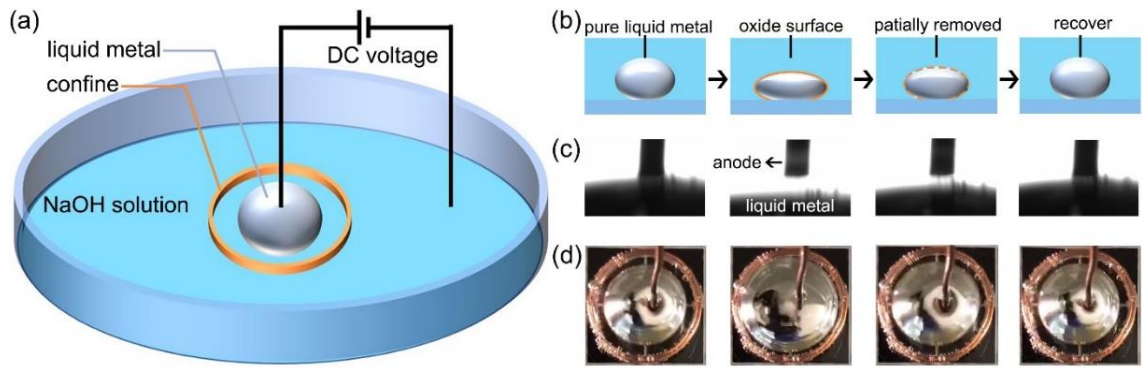
Figure 6.1. Working mechanism of the periodic beating effect of liquid metal. (a) Schematic diagram of the experimental setup. (b) Schematic illustration of interfacial-tension-induced beating process. (c) Front and (d) top-view real-time images of THE beating effect of liquid metal.

To describe the heart-beating effect in detail, the statistical data on the distance between the LMD and the anode, and the diameter change were collected, as shown in **Figure 6.2a** and **b**. The original diameter of the LMD (without voltage) is 14 mm, confined by a ring of 16 mm in diameter. The vertical displacement of LMD is defined relative to the fixed anode. That is, when the value of displacement is zero, the top of the LMD is in contact with the anode. The negative values of displacement indicates that the LMD deforms and moves beneath the anode. The descending part of the displacement curve in **Figure 6.2a** means that the LMD leaves the anode and moves downward, while the rising part indicate that the LMD bounces back to the anode. Once the external voltage is on, the LMD starts the beating process, and a stable periodic beating effect is observed after unsteady beating in the initial stage. The amplitude for the periodic beating stage

reaches up to 1 mm. **Figure 6.2b** shows the diameter change of the LMD during the beating process, where the diameter expands from 13.9 to 14.6 mm. The blue and purple dashed lines delineate the specific part of the displacement and diameter waveform shown in **Figure 6.2c** and **d**, respectively. The waveforms are both well fitted by the same sine function with frequency of about 6 Hz. **Figure 6.2** demonstrates that, for an LMD with diameter of 14 mm, regular periodic beating process with fixed frequency of 6 Hz is achieved under 1.5 V external voltage in NaOH.
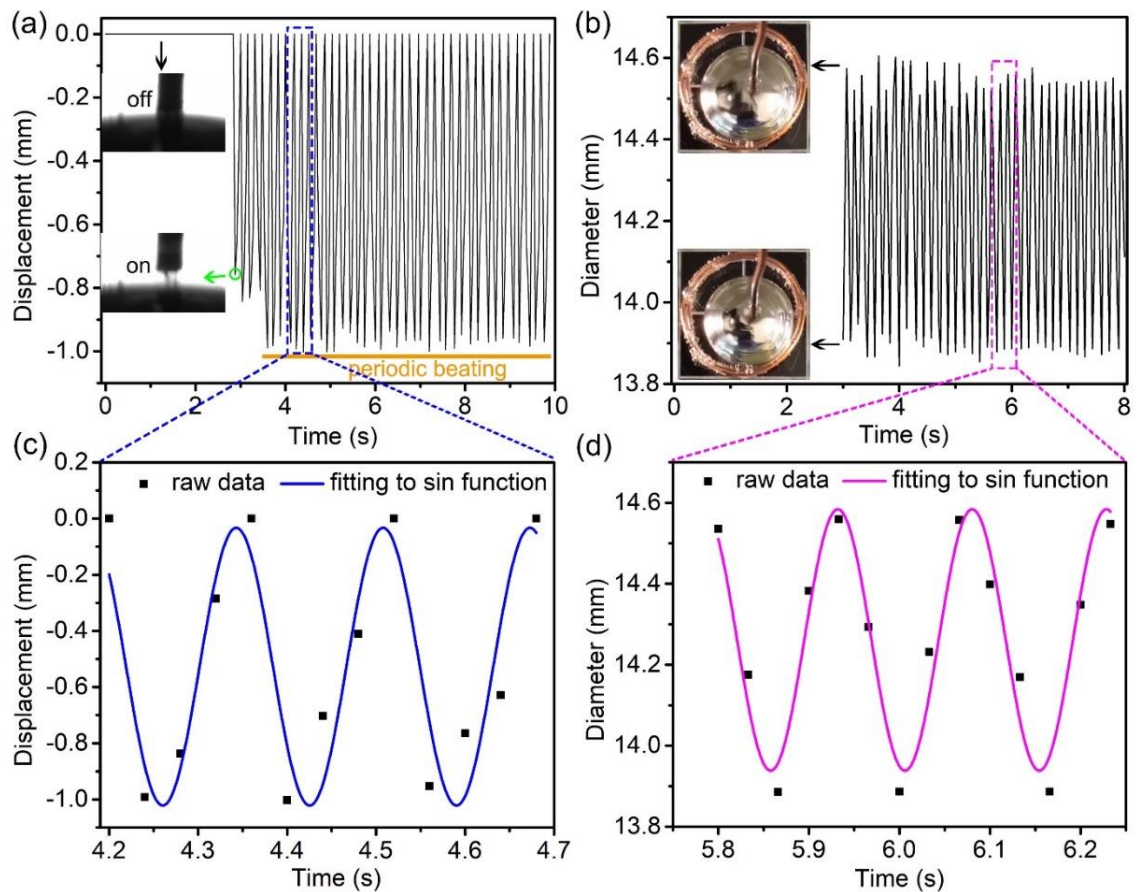
Figure 6.2. Statistical data for displacement (a) and diameter change (b) of the periodic beating of liquid metal with size of 14 mm at the position of 0 mm, the confinement ring 16 mm in size, inset photographs show the heart-beating phenomenon. The blue and purple dashed lines delineate the specific parts of displacement and diameter waveform shown in **c** and **d**, respectively. (**c, d**) The waveform is well fitted by the sine function

with frequency of about 6 Hz.

To realize a controllable heart beating effect, that is, a stable periodic beating process with controllable frequency, LMDs with different diameters from 8.5 to 14 mm were used in the following experiments. **Figure 6.3a** shows the displacement of LMDs, which decreases with their diameter. The curve for each LMD indicates that the stability also decreases with the diameter of the LMD. However, the diameter changes of the LMDs are slightly different, as shown in **Figure 6.3b.** The diameter changes stand for the value of the real-time diameter minus the original diameter. The diameter changes remain almost the same as the diameter decreases from 14 to 10 mm. Then, a sudden drop is observed when the diameter further decreases to 8.5 mm. The curves of diameter changes also indicate that the stability decreases with the diameter. The corresponding statistical data on the displacement and diameter changes of LMDs with different diameters are shown in **Figure 6.3c.** Moreover, the beating frequency for each LMD is also analyzed in **Figure 6.3d**. Surprisingly, the frequency for LMDs with different diameters does not show any diameter-dependent increase or decrease. The frequency changes within only 1 Hz as the diameter changes by 6 mm. **Figure 6.3** shows that the diameter of the LMD determines the stability of the periodic beating process, while the frequency is independent of the diameter (size) of the LMD.
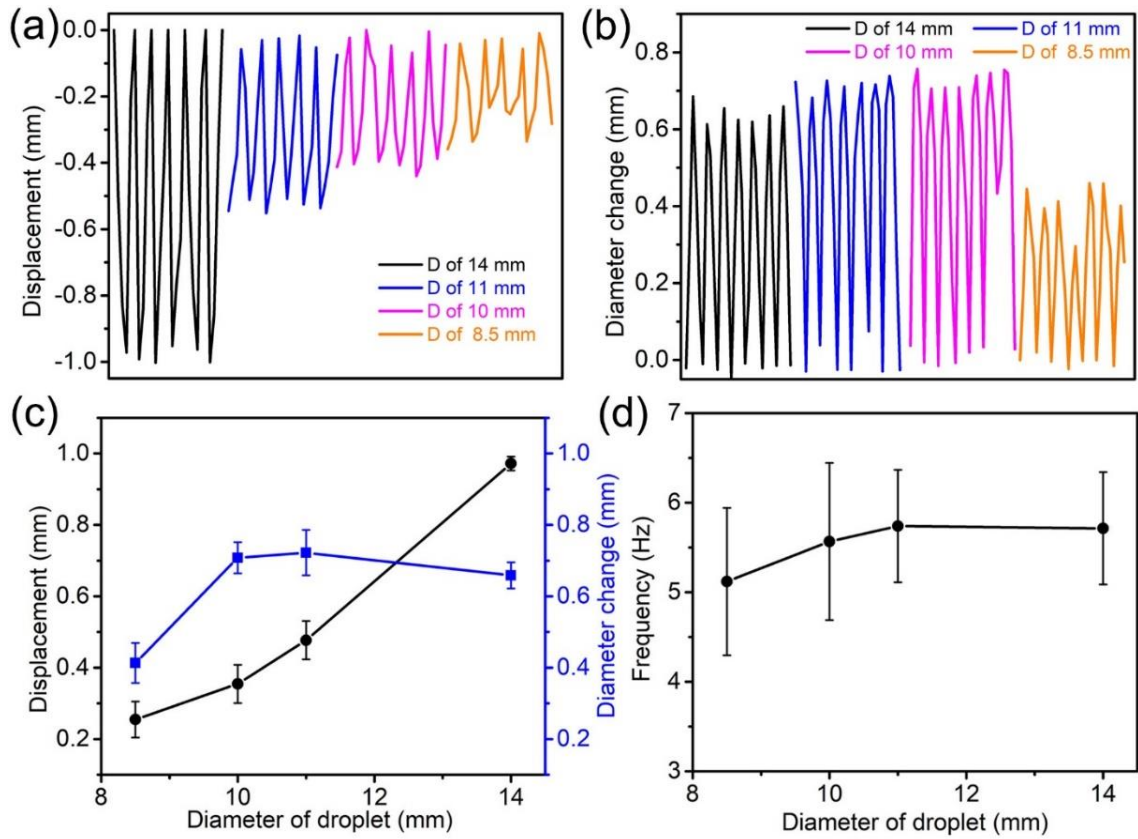
Figure 6.3. Periodic beating effect for LMDs with different diameters from 8.5 to 14 mm with (a) different displacements and (b) various diameter changes. (c) The displacement and diameter changes, as well as (d) the frequency changes.

Thus, a new approach was developed to realize the periodic beating effect with controllable frequency. That is, changing the initial position of anode for the cyclic movements. The top of the LMD with deformation was defined as the zero point. When the anode is in contact with the LMD at the point, the value of the anode position (P_A) is defined as $P_A = 0$ mm. The negative value of P_A indicates that the anode moves downward to trigger the beating process, as shown in **Figure 6.4a**. The anode position varies from 0 to -2 mm. Once the voltage is on, the anode is then fixed during each periodic beating process. The displacement, which is still defined as the distance between the top surface of the LMD and anode is shown in **Figure 6.4b**. The displacement remains the periodic with stable change at $P_A = -0.5$ mm, while the LMD starts to bounce back over the position

of the anode. When P_A further decreases to -1.0 mm, instability in the beating process emerges. Most displacement of the LMD is recorded within the range of -1.5 to -0.5 mm, while some large displacements accompanied by wider peaks are observed when the LMD bounces back to the position of zero point. The results indicate that every time the LMD bounces back, it moves upward over the anode position at P_A = -1.0 cm. These wider peaks result in a decrease of the beating frequency. When P_A = -1.5 mm, the LMD still shows periodic beating but with a further decreased frequency, and the displacement becomes more unsteady. That is, the amplitude of the displacement changes from smallest value of 0.75 mm (with the position from -0.75 to 0 mm) to the biggest value of 2.5 mm (with the position from -2.0 to +0.5 mm). The width change of each peak is consistent with displacement change. For most beating, the LMD moves within the range from -1.75 to -0.25 mm, during which the LMD moves downward for a short displacement reaching the position of -1.75 mm, but the distance for downward motion is only 0.25 mm. Then, the LMD bounces back a long distance to the position of -0.25 mm, while the distance for upward motion reaches 1.5 mm, which is 6× times that for downward motion. The results show that the anode is immersed in the LMD without merging for most of their time during the beating process. When P_A = -2.0 mm, the difference in amplitude of displacement is more significant. The displacement changes within the range from -2.5 to +0.5 mm. Moreover, dual peaks of curves are observed in a single cycle, and the time interval for dual peaks is almost double the time interval for a single peak. The beating process is roughly composed of two kinds of peaks with different width. The amplitude of displacement is further enlarged (from -4.5 to -0.5 mm) when P_A = -2.5 cm, with decreased frequency. The difference for the two kinds of peaks, including displacement amplitude and frequency between each cycle, is more significant. When the anode is placed at -3.0 cm, however, the amplitude of the displacement dramatically decreases

within changes from -4 to -2 cm while the frequency keeps decreasing.

Moreover, the statistical data for diameter changes at each position of the anode, as shown in **Figure 6.4c**, was also collected. The LMD remains a spherical structure for P_A from 0 to -1.0 mm, and the even changes in the diameter show the stable and periodic beating process at these positions, while some uneven changes with higher peaks start to emerge at P_A = -1.0 mm. Moreover, the uneven changes of diameter become more significant at P_A = -1.5 mm, and they turn into chaotic beating at P_A = -2.0 mm. The uneven change of diameter is manifested as an elliptical shape of the LMD, which is the dominant structure of the LMD at P_A = -2.0 mm. The elliptical shapes are shown as the error bars in the diameter curves at P_A = -1.5 and -2.0 mm. When P_A = -2.5 mm, the statistical diameter is no longer applicable, as a new triangular shape of LMD emerges during the beating process. The LMD deforms between circular/elliptical and triangular shapes, leading to violent and chaotic beating, which is also responsible for the largest change in amplitude of displacement. When P_A = -3.0 cm, the LMD forms a new hybrid structure instead of deforming between different shapes. As shown in the inset image, the hybrid structure is composed of a circular shape for top half and triangular shape for the bottom half. When the triangular part occasionally turns into the circular shape, the beating process stops. That is what happens at P_A = -3.5 mm, where the LMD stops beating as it deforms in larger circular shape and fully fills the confine.
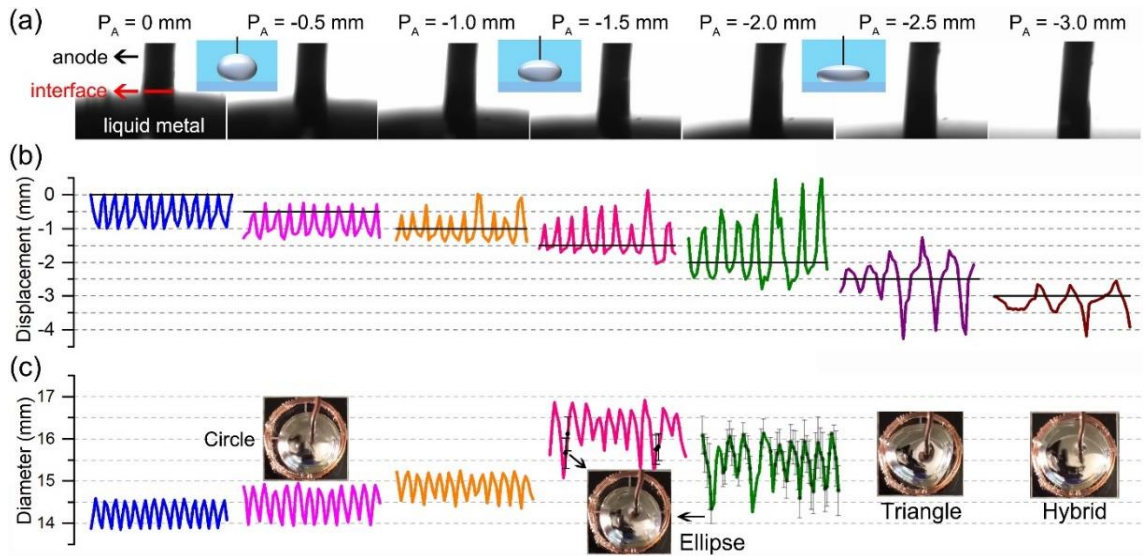
Figure 6.4. Periodic beating effect with different anode positions. (a) Schematic diagram of the anode-position-dependent beating process, with a negative value indicating that the anode moves downward. Corresponding displacement (b) and diameter (c) of LMDs at different position.

By changing the anode position, the beating frequency of an LMD is controllable with a synchronous morphological transformation process. The beating shape experiences circular, elliptical, triangular, and hybrid structures as the anode position moves downward. The beating motion of LMDs with different sizes and with different anode positions were also explored to further demonstrate the variable beating with different frequency and morphology, as well as the correlation between frequencies and morphologies. The corresponding statistical data on displacement and frequency were collected, as shown in **Figure 6.5**. The displacement of different LMDs shows the same trend, that is, the displacement first increases, reaching a maximum value at a certain anode position. Then, it immediately decreases to zero, as in **Figure 6.5a**. The value of the anode position for maximum displacement increases with droplet size. The corresponding frequency of the beating process, which decreases with droplet size all the

way to zero, can be divided into three modes. As shown in **Figure 6.5b**, modes I, II, and III stand for the beating shape difference of LMDs, which are circular/elliptical, elliptical/triangular, and hybrid shapes, respectively. Mode I is located in the area before maximum displacement, in which the beating shape changes form a circle to an ellipse. In this mode, the beating process is stable and lasts for a long time with typical frequency from 6 to 4 Hz. Mode II is at the position of maximum displacement, where the beating shapes shifts between ellipse and triangle. The beating process is violent, and a beating break is observed during shape shift, with typical frequency of around 3 Hz. In the case of mode III, which is in the region after the maximum displacement, the LMD forms a hybrid structure composed of part circle (greater deformation compared to the circular shape in mode I) and part triangle. The beating frequency in this mode depends on the ratio of circle to triangle. That is, the beating frequency decreases with the increase of the circle to triangle ratio until the beating stops at the fully deformed circular shape. The typical frequency for this mode is lower than 2.5 Hz.
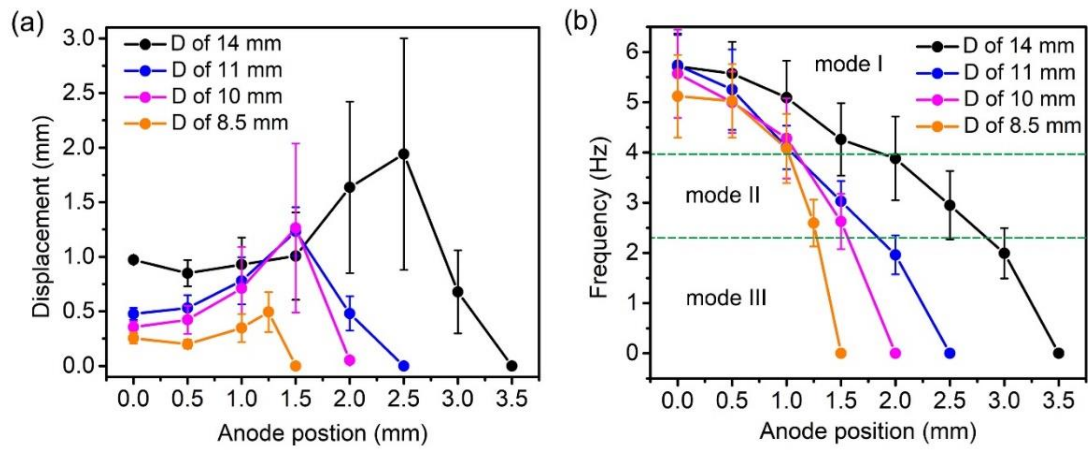
Figure 6.5. (a) Displacement and (b) frequency of LMDs of different sizes with different anode positions. Modes I, II, and III stand for different beating shapes of LMDs, which are circular/elliptical, elliptical/triangular, and hybrid shapes, respectively.

During the beating process of an LMD, the diameter and height of the LMD change

in opposite ways. That is, when the LMD moves downward, the diameter increases while the height decreases, and vice versa when the LMD bounces upward. The equilibrium shape of the LM is controlled by the balance between gravity (spreading force) and the Laplace pressure (restoring force) induced by interfacial tension. The maximum gravitational pressure at the crest of the LMD is as follows:

$$P_g \approx \rho g h \tag{6-1}$$

The Laplace pressure is:

$$P_L \approx \gamma \frac{2}{R} \tag{6-2}$$

where P_g is the gravitational pressure, ρ is the density of the LM, g is the gravitational acceleration, h is the height of the LMD, P_L is the interfacial tension induced Laplace pressure, γ is the interfacial tension, and R is the radius of curvature at the crest of the LMD. For small LMDs that form quasi-spherical structured:

$$R \approx \frac{h}{2} \tag{6-3}$$

Thus, for every balanced state ($P_g = P_L$) with specific interfacial tension, the height of the LMD:

$$h \approx \sqrt{\frac{4\gamma}{\rho g}} \tag{6-4}$$

For a static LMD without external power, the calculated value of h is about 6 mm. That is, for a quasi-spherical structure of an LMD, the height of the LMD is under the value for the equilibrium state. The shape of an LMD deforms, however, as LMD becomes larger. The height of an LMD slowly increases with the volume of the LMD, the diameter (d), however, increases faster with the volume compared to the height, changing the quasi-spherical structure to an elliptical shape. The radius of the curvature at the crest of the LMD varies in the region:

$$R > \frac{d}{2} > \frac{h}{2} \tag{6-5}$$

The relationship between height and diameter is set as:

$$h = kd, \ (0 < k \leq 1) \tag{6-6}$$

where k is defined as beating factor, the ration of the height to the diameter of the LMD for heartbeat process. This is because the gravity depends on the height, while the interfacial tension is represented by the diameter. The value of k reflects the relationship bewteen gravity and interfacial tension. And the value of $k = 1$ represents the quasi-spherical structure of an LMD, thus:

$$h \leq \sqrt{\frac{4k\gamma}{\rho g}} \leq 6 \ mm \tag{6-7}$$

The changes in the height and height-diameter ratio of a static LMD in the equilibrium state are shown in **Figure 6.6**. The statistical data on height of an LMD is fitted well by an exponential growth function (black curve):

$$h = 6.5 - 6.16 \cdot e^{\frac{-d}{6.77}} \leq 6.5 \ mm \tag{6-8}$$

which is consistent with my calculations within the margin of error. The statistical data on the h/d ratio (k) is fitted well by an exponential decay function (blue curve in **Figure 6.6**):

$$k = 0.2 + 0.86 \cdot e^{\frac{-d}{10}} \geq 0.2 \tag{6-9}$$

Thus, for a static droplet without external voltage, the threshold value of k is 0.2 for a balanced state.
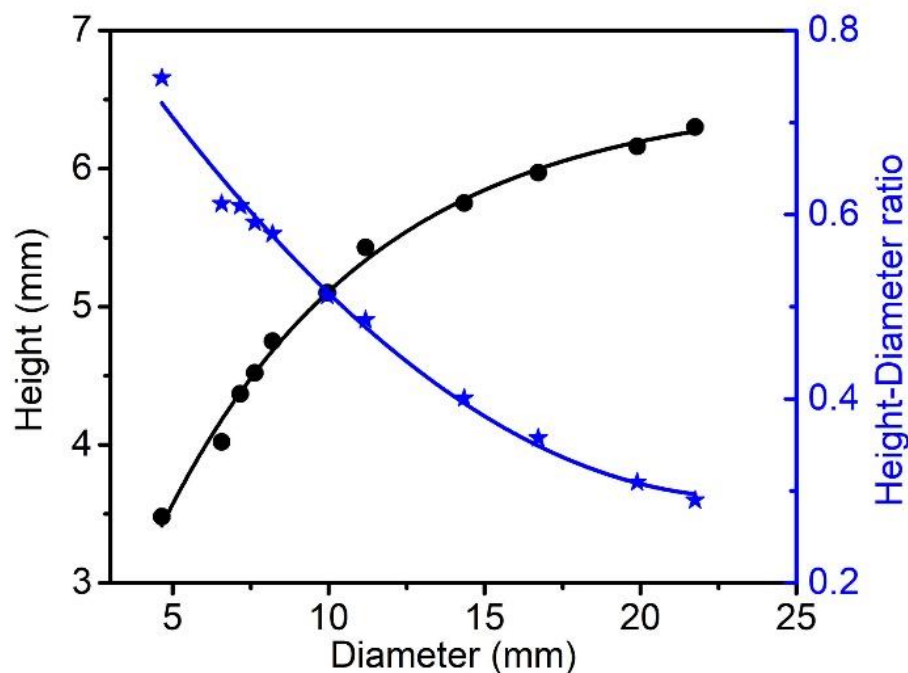
Figure 6.6. Height-diameter ratio of a static LMD in the equilibrium state due to the balance between gravitational pressure and Laplace pressure induced by interfacial tension.

A lower value of *k* is expected, however, when external voltage is applied, since the voltage induced electrochemical oxidation process on the surface of the LMD decreases the surface tension. Thus, a new balanced state will be achieved with lower shifting of the critical value of *k*. Once *k* reaches the threshold value, the LMD is expected to demonstrate a similar static balanced state even with external voltage. As mentioned above, the threshold value of *k* is reached by moving the anode downward to a critical value, until the LMD loses the ability to deform and keeps in contact with the anode, realizing the new static balance state. The critical value of the anode position varies for different LMDs with different sizes. With the position of the anode between zero and the critical value, variable beating motions are observed with different amplitudes and frequencies. Thus, the value of *k* for different LMDs with changing position of the anode has been collected for better analysis, as shown in **Figure 6.7**. The blue curve represents

the k value change of static state droplets without external voltage, while the new static state is achieved by the balance between gravity and reduced interfacial tension. The red points are where the LMDs stop beating at the critical anode position (see **Figure 6.5**). The heartbeat region between the two static states is divided into three modes based on beating amplitude and frequency. These beating curves are roughly fitted by the same exponential decay function as static state droplets without external voltage (blue curve) as follows:

$$static\ state: k_s = 0.2 + 0.86 \cdot e^{\frac{-d}{10}} \tag{6-11}$$

$$mode\ I: k_I = 0.11 + 0.86 \cdot e^{\frac{-d}{10}} \tag{6-12}$$

$$mode\ II: k_{II} = 0.05 + 0.86 \cdot e^{\frac{-d}{10}} \tag{6-13}$$

$$mode\ III: k_{III} = 0.01 + 0.86 \cdot e^{\frac{-d}{10}} \tag{6-14}$$

When $k_I < k < k_s$, a beating process with circular/elliptical shape of LMDs at the frequency of 4-6 Hz is observed. When $k_{II} < k < k_I$, the beating shape transforms to elliptical/triangular with frequency of about 3 Hz, while for $k_{III} < k < k_{II}$, LMDs deform in a hybrid shape with frequency lower than 2.5 Hz. When the value of k is lower than k_{III}, the LMDs become flat and stop the heartbeat process, which indicates that the interfacial tension is extremely low, resulting in flowing shapeless LM. These typical curves can be used to predict the beating process of an LMD with specific height and diameter.
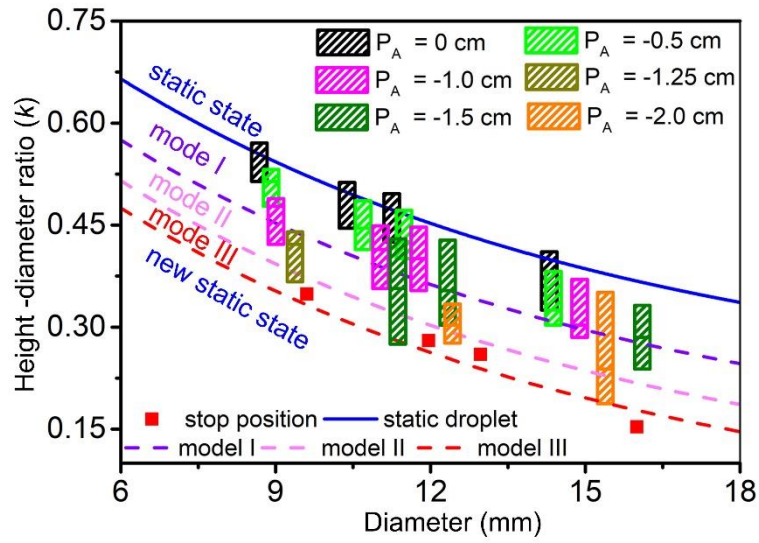
Figure 6.7. Statistical value of k for LMDs with different size beating at different anode position (P_A). The blue curve represents the k value change of static state droplets without external voltage, while the new static state is achieved by the balance between gravity and reduced interfacial tension. The heartbeat region between the two static states is divided into three modes based on beating amplitude and frequency.

6.4 Conclusion and Prospect

In this work, the heartbeat effect of liquid metal droplets is optimized, and droplets with different sizes stimulated by a small voltage of 1.5 V with various electrode positions are presented. The beating process with different amplitudes and frequencies is systematical studied by setting experimental variables. An intuitive visual connection between the beating shapes and frequency is built. LMD deforms from spherical to other shapes (i.e., elliptical, triangular and hybrid) and recovers periodically during the beating process. The beating frequency, which is related to different shapes of the LMD, is controllable from 2 to 6 Hz. A beating factor k, the ratio of the height to the diameter of droplets, is also defined to characterize the periodic process within the balance between gravity and interfacial tension. The curves of the values of k for different beating modes, which are

fitted by an exponential decay function, have been developed to predict the beating process for an LMD with a specific height and diameter. This work provides a fundamental insight into the beating process, as well as enabling potential fluidic and bionic applications, such as liquid actuators/pumps and soft robots.

Chapter 7. Conclusions and Prospect

7.1 Major Conclusions

In this doctoral work, emerging fluidic and electrochemical properties of gallium-based liquid metal are explored. Novel new phenomena are observed, and potential corresponding applications are proposed. The new screening effect, optimized heartbeat effect, and non-contact manipulation of liquid metal wires are systematically studied with thorough analysis of underlying mechanism. The major conclusions are as follows:

1. I discovered that the liquid metal streams could be formed with the help of electrochemical oxidation by overcoming the Rayleigh–Plateau instability. Moreover, I explored a non-contact manipulation of the freefalling cylindrical streams of liquid metals into unique shapes, such as levitated loops and squares. Such cylindrical streams can be formed in aqueous media by electrochemically lowering the interfacial tension. The electrochemical reactions require an electrical current that flows through the streams, making them susceptible to Lorentz forces. Consequently, varying the position and shape of a magnetic field relative to the stream controls these forces. Moreover, the movement of the metal stream relative to the magnetic field induces significant forces arising from Lenz's law that cause the manipulated streams to levitate in unique shapes. The ability to control streams of liquid metals in a non-contact manner will enable new strategies for shaping electronically conductive fluids for advanced manufacturing and dynamic electronic structures.

2. I demonstrated the screening effect which prevented the further oxidation of liquid metals. The screening effect is induced when a liquid metal droplet deforms and surrounds the cathode in an electrical circuit, yielding a huge inner electric field within the electrical-double-layer to counter the external electric field. Analogous

contact inhibition behavior of multi-droplets triggered by the screening effect was also observed. The droplets were arranged to arrive at the cathode at the same time (e.g., tilted substrate), and they came into contact with each other without merging and stopped their deformation. Once they were separated by moving the cathode, the deformation process was restarted.

3. I optimized the controllable heart beating effect of liquid metal. In this work, the experimental setup is modified for easier implementation compared to previous report. The heartbeat effect of liquid metal droplets with different sizes were stimulated by a small voltage of 1.5 V with various electrode positions. A beating factor k, the ratio of the height to the diameter of the droplets, was defined to characterize the periodic process within the balance between gravitational pressure and interfacial tension. This work optimizes the heartbeat effect of liquid metal, and provides a fundamental insight into the beating process, as well as enabling potential fluidic and bionic applications, such as liquid actuators/pumps and soft robots.

7.2 Prospect and Challenges

As liquid metals and alloys possess simultaneous fluidic and metallic properties, endowing them various novel properties as well as potential applications. The intrinsic functions such as he unusual rheological properties, wettability, and core-shell structure make liquid metals unique. This thesis tried to explore the liquid metal actuation based on the unique rheological properties and electrochemically controlled surface state of liquid metal, thereby discovering new fluid dynamic phenomenon and realizing manipulation if fluids. These actuations might provide new mechanism for novel fluid properties, lay the foundation for precisely manipulation of fluidic motion, and pave the way for new strategies of shaping useful metallic shapes/soft robots. However, how to

realize these actuations in more precise ways is still a major challenge in future. And the challenge could be subdivided into specific issues to be solved. That is, 1) the precise control and characterization of the surface tension of liquid metal, 2) stable and sustainable manipulation of liquids in controllable temporal and spatial scales to build universal ways for fluidic manipulation, 3) associated liquid metal with traditional liquids and metals for a broader range of potential practical use. And my following work will focus on theses issues and try to explore the liquid metal actuation in a broader and more accurate way, and finally contribute to useful applications of liquid metal.

Bibliography or List of References

1.   W. M. Haynes, D. R. L., T. J. Bruno, *CRC Handbook of Chemistry and Physics*. CRC Press: Boca Raton, FL, 2017.

2.   Dickey, M. D., Stretchable and Soft Electronics using Liquid Metals. *Advanced materials* **2017,** *29* (27).

3.   Daeneke, T.; Khoshmanesh, K.; Mahmood, N.; de Castro, I. A.; Esrafilzadeh, D.; Barrow, S. J.; Dickey, M. D.; Kalantar-Zadeh, K., Liquid metals: fundamentals and applications in chemistry. *Chemical Society reviews* **2018,** *47* (11), 4073-4111.

4.   Bartlett, M. D.; Fassler, A.; Kazem, N.; Markvicka, E. J.; Mandal, P.; Majidi, C., Stretchable, High-k Dielectric Elastomers through Liquid-Metal Inclusions. *Advanced materials* **2016,** *28* (19), 3726-31.

5.   Liu, T., Sen, P., & Kim, C. J., Characterization of nontoxic liquid-metal alloy galinstan for applications in microdevices. Journal of Microelectromechanical Systems. *Journal of Microelectromechanical Systems* **2011,** *21(2)*, 443-450.

6.   Wang, Q.; Yu, Y.; Yang, J.; Liu, J., Fast Fabrication of Flexible Functional Circuits Based on Liquid Metal Dual-Trans Printing. *Advanced materials* **2015,** *27* (44), 7109-16.

7.   Ladd, C.; So, J. H.; Muth, J.; Dickey, M. D., 3D printing of free standing liquid metal microstructures. *Advanced materials* **2013,** *25* (36), 5081-5.

8.   Khan, M. R.; Trlica, C.; Dickey, M. D., Recapillarity: Electrochemically Controlled Capillary Withdrawal of a Liquid Metal Alloy from Microchannels. *Advanced Functional Materials* **2015,** *25* (5), 671-678.

9.   Wang, X.; Yao, W.; Guo, R.; Yang, X.; Tang, J.; Zhang, J.; Gao, W.; Timchenko, V.; Liu, J., Soft and Moldable Mg-Doped Liquid Metal for Conformable Skin Tumor Photothermal Therapy. *Advanced healthcare materials* **2018,** *7* (14), e1800318.

10. Khan, M. R.; Eaker, C. B.; Bowden, E. F.; Dickey, M. D., Giant and switchable surface activity of liquid metal via surface oxidation. *Proceedings of the National Academy of Sciences of the United States of America* **2014,** *111* (39), 14047-51.

11. Minyung Song, K. K., Keith D. Hillaire, Cheng Li, Collin B. Eaker, Abolfazl Kiani,Karen E. Daniels, Michael D. Dickey, Overcoming Rayleigh–Plateau instabilities: Stabilizing and destabilizing liquid-metal streams via electrochemical oxidation. *Proceedings of the National Academy of Sciences* **2020,** *17(32)*, 19026-19032.

12. So, J.-H.; Thelen, J.; Qusba, A.; Hayes, G. J.; Lazzi, G.; Dickey, M. D., Reversibly Deformable and Mechanically Tunable Fluidic Antennas. *Advanced Functional Materials* **2009,** *19* (22), 3632-3637.

13. Zheng, Y.; He, Z. Z.; Yang, J.; Liu, J., Personal electronics printing via tapping mode composite liquid metal ink delivery and adhesion mechanism. *Scientific reports* **2014,** *4*, 4588.

14. Ali Zavabeti, J. Z. O., Benjamin J. Carey, Nitu Syed, Rebecca Orrell-Trigg, Edwin L. H. Mayes, Chenglong Xu, Omid Kavehei, Anthony P. O'Mullane, Richard B. Kaner, Kourosh Kalantar-zadeh, Torben Daeneke., A liquid metal reaction environment for the room-temperature synthesis of atomically thin metal oxides. *Science* **2017,** *358 (6361)*, 332-335.

15. Alsaif, M. M. Y. A.; Kuriakose, S.; Walia, S.; Syed, N.; Jannat, A.; Zhang, B. Y.; Haque, F.; Mohiuddin, M.; Alkathiri, T.; Pillai, N.; Daeneke, T.; Ou, J. Z.; Zavabeti, A., 2D SnO/In2O3 van der Waals Heterostructure Photodetector Based on Printed Oxide Skin of Liquid Metals. *Advanced Materials Interfaces* **2019,** *6* (7), 1900007.

16. Mahmood, N.; Khan, H.; Tran, K.; Kuppe, P.; Zavabeti, A.; Atkin, P.; Ghasemian, M. B.; Yang, J.; Xu, C.; Tawfik, S. A.; Spencer, M. J. S.; Ou, J. Z.; Khoshmanesh, K.; McConville, C. F.; Li, Y.; Kalantar-Zadeh, K., Maximum piezoelectricity in a few unit-

cell thick planar ZnO – A liquid metal-based synthesis approach. *Materials Today* **2021,** *44*, 69-77.

17.	Carey, B. J.; Ou, J. Z.; Clark, R. M.; Berean, K. J.; Zavabeti, A.; Chesman, A. S.; Russo, S. P.; Lau, D. W.; Xu, Z. Q.; Bao, Q.; Kevehei, O.; Gibson, B. C.; Dickey, M. D.; Kaner, R. B.; Daeneke, T.; Kalantar-Zadeh, K., Wafer-scale two-dimensional semiconductors from printed oxide skin of liquid metals. *Nature communications* **2017,** *8*, 14482.

18.	Daeneke, T.; Atkin, P.; Orrell-Trigg, R.; Zavabeti, A.; Ahmed, T.; Walia, S.; Liu, M.; Tachibana, Y.; Javaid, M.; Greentree, A. D.; Russo, S. P.; Kaner, R. B.; Kalantar-Zadeh, K., Wafer-Scale Synthesis of Semiconducting SnO Monolayers from Interfacial Oxide Layers of Metallic Liquid Tin. *ACS nano* **2017,** *11* (11), 10974-10983.

19.	Messalea, K. A.; Carey, B. J.; Jannat, A.; Syed, N.; Mohiuddin, M.; Zhang, B. Y.; Zavabeti, A.; Ahmed, T.; Mahmood, N.; Della Gaspera, E.; Khoshmanesh, K.; Kalantar-Zadeh, K.; Daeneke, T., Bi2O3 monolayers from elemental liquid bismuth. *Nanoscale* **2018,** *10* (33), 15615-15623.

20.	Syed, N.; Zavabeti, A.; Messalea, K. A.; Della Gaspera, E.; Elbourne, A.; Jannat, A.; Mohiuddin, M.; Zhang, B. Y.; Zheng, G.; Wang, L.; Russo, S. P.; Esrafilzadeh, D.; McConville, C. F.; Kalantar-Zadeh, K.; Daeneke, T., Wafer-sized ultrathin gallium and indium nitride nanosheets through the ammonolysis of liquid metal derived oxides. *Journal of the American Chemical Society* **2018**.

21.	Sivan, V.; Tang, S.-Y.; O'Mullane, A. P.; Petersen, P.; Eshtiaghi, N.; Kalantar-zadeh, K.; Mitchell, A., Liquid Metal Marbles. *Advanced Functional Materials* **2013,** *23* (2), 144-152.

22.	Wei Zhang, J. Z. O., Shi-Yang Tang, Vijay Sivan, David D. Yao, Kay Latham, Khashayar Khoshmanesh, Arnan Mitchell, Anthony P. O'Mullane, Kourosh Kalantar-

zadeh., Liquid Metal/Metal Oxide Frameworks. *Advanced Functional Materials* **2014,** *24 (24)*, 3799-3807.

23.   David, R.; Miki, N., Synthesis of sub-micrometer biphasic Au-AuGa2/liquid metal frameworks. *Nanoscale* **2019,** *11* (44), 21419-21432.

24.   Ma, B.; Xu, C.; Chi, J.; Chen, J.; Zhao, C.; Liu, H., A Versatile Approach for Direct Patterning of Liquid Metal Using Magnetic Field. *Advanced Functional Materials* **2019**, 1901370.

25.   Zhang, J.; Sheng, L.; Liu, J., Synthetically chemical-electrical mechanism for controlling large scale reversible deformation of liquid metal objects. *Scientific reports* **2014,** *4*, 7116.

26.   Hu, L.; Wang, L.; Ding, Y.; Zhan, S.; Liu, J., Manipulation of Liquid Metals on a Graphite Surface. *Advanced materials* **2016,** *28* (41), 9210-9217.

27.   Wang, X.; Guo, R.; Liu, J., Liquid Metal Based Soft Robotics: Materials, Designs, and Applications. *Advanced Materials Technologies* **2018**, 1800549.

28.   Handschuh-Wang, S.; Chen, Y.; Zhu, L.; Gan, T.; Zhou, X., Electric Actuation of Liquid Metal Droplets in Acidified Aqueous Electrolyte. *Langmuir : the ACS journal of surfaces and colloids* **2019,** *35* (2), 372-381.

29.   Tang, S.-Y.; Sivan, V.; Khoshmanesh, K.; O'Mullane, A. P.; Tang, X.; Gol, B.; Eshtiaghi, N.; Lieder, F.; Petersen, P.; Mitchell, A.; Kalantar-zadeh, K., Electrochemically induced actuation of liquid metal marbles. *Nanoscale* **2013,** *5* (13), 5949.

30.   Wang, L.; Liu, J., Electromagnetic rotation of a liquid metal sphere or pool within a solution. *Proceedings of the Royal Society A: Mathematical, Physical and Engineering Sciences* **2015,** *471* (2178), 20150177.

31.   Tingyi Liu, P. S. a. C.-J. K., Characterization of nontoxic liquid-metal alloy

galinstan for applications in microdevices. *JOURNAL OF MICROELECTROMECHANICAL SYSTEMS* **2012,** *21*, 443.

32.   Handschuh-Wang, S.; Chen, Y.; Zhu, L.; Zhou, X., Analysis and Transformations of Room-Temperature Liquid Metal Interfaces - A Closer Look through Interfacial Tension. *ChemPhysChem* **2018,** *19* (13), 1551-1551.

33.   Spells, K. E., The determination of the viscosity of liquid gallium over an extended nrange of temperature. *Proceedings of the Physical Society* **1936,** *48*, 299.

34.   Zhu, L.; Wang, B.; Handschuh-Wang, S.; Zhou, X., Liquid Metal-Based Soft Microfluidics. *Small* **2020,** *16* (9), e1903841.

35.   Dickey, M. D.; Chiechi, R. C.; Larsen, R. J.; Weiss, E. A.; Weitz, D. A.; Whitesides, G. M., Eutectic Gallium-Indium (EGaIn): A Liquid Metal Alloy for the Formation of Stable Structures in Microchannels at Room Temperature. *Advanced Functional Materials* **2008,** *18* (7), 1097-1104.

36.   Sun, X.; Yuan, B.; Rao, W.; Liu, J., Amorphous liquid metal electrodes enabled conformable electrochemical therapy of tumors. *Biomaterials* **2017,** *146*, 156-167.

37.   Chechetka, S. A.; Yu, Y.; Zhen, X.; Pramanik, M.; Pu, K.; Miyako, E., Light-driven liquid metal nanotransformers for biomedical theranostics. *Nature communications* **2017,** *8*, 15432.

38.   Boley, J. W.; White, E. L.; Chiu, G. T. C.; Kramer, R. K., Direct Writing of Gallium-Indium Alloy for Stretchable Electronics. *Advanced Functional Materials* **2014,** *24* (23), 3501-3507.

39.   Thelen, J.; Dickey, M. D.; Ward, T., A study of the production and reversible stability of EGaIn liquid metal microspheres using flow focusing. *Lab on a chip* **2012,** *12* (20), 3961-7.

40.   Hutter, T.; Bauer, W.-A. C.; Elliott, S. R.; Huck, W. T. S., Formation of Spherical

and Non-Spherical Eutectic Gallium-Indium Liquid-Metal Microdroplets in Microfluidic Channels at Room Temperature. *Advanced Functional Materials* **2012,** *22* (12), 2624-2631.

41.   Yang Yu, Q. W., Liting Yi, Jing Liu, Channelless Fabrication for Large-Scale Preparation of Room Temperature Liquid Metal Droplets. *Advanced Engineering Materials* **2014,** *16(2)*, 255-262.

42.   Wen-Qiang Fang, Z.-Z. H., Jing Liu, Electro-hydrodynamic shooting phenomenon of liquid metal stream. *Applied Physics Letters* **2014,** *105(13)*, 134104.

43.   Yu, Y.; Wang, Q.; Wang, X. L.; Wu, Y. H.; Liu, J., Liquid metal soft electrode triggered discharge plasma in aqueous solution. *RSC Advances* **2016,** *6* (115), 114773-114778.

44.   Tang, S. Y.; Joshipura, I. D.; Lin, Y.; Kalantar-Zadeh, K.; Mitchell, A.; Khoshmanesh, K.; Dickey, M. D., Liquid-Metal Microdroplets Formed Dynamically with Electrical Control of Size and Rate. *Advanced materials* **2016,** *28* (4), 604-9.

45.   Qian Wang, Y. Y., Jing Liu, Preparations, Characteristics and Applications of the Functional Liquid Metal Materials. *Adv. Eng. Mater* **2018,** *20*, 1700781.

46.   Honey, E. M.; Kavehpour, H. P., Astonishing life of a coalescing drop on a free surface. *Physical review. E, Statistical, nonlinear, and soft matter physics* **2006,** *73* (2 Pt 2), 027301.

47.   Aussillous, P., Quéré, D. , Liquid marbles. *Nature* **2001,** *411(6840)*, 924-927.

48.   Dell'Aversana, P.; Neitzel, G. P., Behavior of noncoalescing and nonwetting drops in stable and marginally stable states. *Experiments in Fluids* **2003,** *36* (2), 299-308.

49.   Sreenivas, K. R., De, P. K., Arakeri, J. H., Levitation of a drop over a film flow. *Journal of Fluid Mechanics* **1999,** *380*, 297-307.

50.   Lhuissier, H.; Tagawa, Y.; Tran, T.; Sun, C., Levitation of a drop over a moving

surface. *Journal of Fluid Mechanics* **2013,** *733*.

51. Ding, Y.; Liu, J., Dynamic interactions of Leidenfrost droplets on liquid metal surface. *Applied Physics Letters* **2016,** *109* (12), 121904.

52. Couder, Y.; Fort, E.; Gautier, C. H.; Boudaoud, A., From bouncing to floating: noncoalescence of drops on a fluid bath. *Phys Rev Lett* **2005,** *94* (17), 177801.

53. Zhao, X.; Tang, J.; Liu, J., Surfing liquid metal droplet on the same metal bath via electrolyte interface. *Applied Physics Letters* **2017,** *111* (10), 101603.

54. Zhao, X.; Tang, J.; Liu, J., Electrically switchable surface waves and bouncing droplets excited on a liquid metal bath. *Physical Review Fluids* **2018,** *3* (12).

55. Tang, J.; Zhao, X.; Liu, J., Quantized orbital-chasing liquid metal heterodimers directed by an integrated pilot-wave field. *Physical Review Fluids* **2020,** *5* (5).

56. Han, J.; Tang, J.; Idrus-Saidi, S. A.; Christoe, M. J.; O'Mullane, A. P.; Kalantar-Zadeh, K., Exploring Electrochemical Extrusion of Wires from Liquid Metals. *ACS applied materials & interfaces* **2020,** *12* (27), 31010-31020.

57. Jeong, S. H.; Hagman, A.; Hjort, K.; Jobs, M.; Sundqvist, J.; Wu, Z., Liquid alloy printing of microfluidic stretchable electronics. *Lab on a chip* **2012,** *12* (22), 4657-64.

58. Kim, H. J., Son, C., Ziaie, B. , A multiaxial stretchable interconnect using liquid-alloy-filled elastomeric microchannels. *Applied Physics Letters* **2008,** *92(1)*, 011904.

59. Lazarus, N.; Meyer, C. D.; Turner, W. J., A microfluidic wireless power system. *RSC Advances* **2015,** *5* (96), 78695-78700.

60. Lin, Y.; Cooper, C.; Wang, M.; Adams, J. J.; Genzer, J.; Dickey, M. D., Handwritten, Soft Circuit Boards and Antennas Using Liquid Metal Nanoparticles. *Small* **2015,** *11* (48), 6397-403.

61. Markvicka, E. J.; Bartlett, M. D.; Huang, X.; Majidi, C., An autonomously electrically self-healing liquid metal-elastomer composite for robust soft-matter robotics

and electronics. *Nature materials* **2018,** *17* (7), 618-624.

62.   Wang, L.; Liu, J., Compatible hybrid 3D printing of metal and nonmetal inks for direct manufacture of end functional devices. *Science China Technological Sciences* **2014,** *57* (11), 2089-2095.

63.   Zhu, S.; So, J.-H.; Mays, R.; Desai, S.; Barnes, W. R.; Pourdeyhimi, B.; Dickey, M. D., Ultrastretchable Fibers with Metallic Conductivity Using a Liquid Metal Alloy Core. *Advanced Functional Materials* **2013,** *23* (18), 2308-2314.

64.   Palleau, E.; Reece, S.; Desai, S. C.; Smith, M. E.; Dickey, M. D., Self-healing stretchable wires for reconfigurable circuit wiring and 3D microfluidics. *Advanced materials* **2013,** *25* (11), 1589-92.

65.   Li, G.; Wu, X.; Lee, D. W., A galinstan-based inkjet printing system for highly stretchable electronics with self-healing capability. *Lab on a chip* **2016,** *16* (8), 1366-73.

66.   Joshipura, I. D.; Ayers, H. R.; Majidi, C.; Dickey, M. D., Methods to pattern liquid metals. *Journal of Materials Chemistry C* **2015,** *3* (16), 3834-3841.

67.   Zhang, Q.; Gao, Y.; Liu, J., Atomized spraying of liquid metal droplets on desired substrate surfaces as a generalized way for ubiquitous printed electronics. *Applied Physics A* **2013,** *116* (3), 1091-1097.

68.   Gui, H.; Tan, S.; Wang, Q.; Yu, Y.; Liu, F.; Lin, J.; Liu, J., Spraying printing of liquid metal electronics on various clothes to compose wearable functional device. *Science China Technological Sciences* **2016,** *60* (2), 306-316.

69.   Guo, C., Yu, Y., Liu, J. , Rapidly patterning conductive components on skin substrates as physiological testing devices via liquid metal spraying and pre-designed mask. *Journal of Materials Chemistry B* **2014,** *2(35)*, 5739-5745.

70.   Gozen, B. A.; Tabatabai, A.; Ozdoganlar, O. B.; Majidi, C., High-density soft-matter electronics with micron-scale line width. *Advanced materials* **2014,** *26* (30), 5211-

6.

71. Jeong, S. H.; Hjort, K.; Wu, Z., Tape transfer printing of a liquid metal alloy for stretchable RF electronics. *Sensors (Basel)* **2014,** *14* (9), 16311-21.

72. Kramer, R. K.; Majidi, C.; Wood, R. J., Masked Deposition of Gallium-Indium Alloys for Liquid-Embedded Elastomer Conductors. *Advanced Functional Materials* **2013,** *23* (42), 5292-5296.

73. So, J. H.; Dickey, M. D., Inherently aligned microfluidic electrodes composed of liquid metal. *Lab on a chip* **2011,** *11* (5), 905-11.

74. Park, Y. L., Chen, B. R., & Wood, R. J., Design and fabrication of soft artificial skin using embedded microchannels and liquid conductors. *IEEE Sensors journal* **2012,** *12(8)*, 2711-2718.

75. Zhao, W.; Bischof, J. L.; Hutasoit, J.; Liu, X.; Fitzgibbons, T. C.; Hayes, J. R.; Sazio, P. J.; Liu, C.; Jain, J. K.; Badding, J. V.; Chan, M. H., Single-fluxon controlled resistance switching in centimeter-long superconducting gallium-indium eutectic nanowires. *Nano letters* **2015,** *15* (1), 153-8.

76. Tabatabai, A.; Fassler, A.; Usiak, C.; Majidi, C., Liquid-phase gallium-indium alloy electronics with microcontact printing. *Langmuir : the ACS journal of surfaces and colloids* **2013,** *29* (20), 6194-200.

77. Zheng, Y., Zhang, Q., Liu, J. , Pervasive liquid metal based direct writing electronics with roller-ball pen. *Aip Advances* **2013,** *3(11)*, 112117.

78. Lu, T.; Finkenauer, L.; Wissman, J.; Majidi, C., Rapid Prototyping for Soft-Matter Electronics. *Advanced Functional Materials* **2014,** *24* (22), 3351-3356.

79. Khan, M. R.; Bell, J.; Dickey, M. D., Localized Instabilities of Liquid Metal Films via In-Plane Recapillarity. *Advanced Materials Interfaces* **2016,** *3* (23), 1600546.

80. Park, S.; Thangavel, G.; Parida, K.; Li, S.; Lee, P. S., A Stretchable and Self-

Healing Energy Storage Device Based on Mechanically and Electrically Restorative Liquid-Metal Particles and Carboxylated Polyurethane Composites. *Advanced materials* **2019,** *31* (1), e1805536.

81.	Chu, K.; Song, B. G.; Yang, H.-I.; Kim, D.-M.; Lee, C. S.; Park, M.; Chung, C.-M., Smart Passivation Materials with a Liquid Metal Microcapsule as Self-Healing Conductors for Sustainable and Flexible Perovskite Solar Cells. *Advanced Functional Materials* **2018,** *28* (22), 1800110.

82.	Guo, R. S., X. Yuan, B. Wang, H. Liu, J., Magnetic Liquid Metal (Fe-EGaIn) Based Multifunctional Electronics for Remote Self-Healing Materials, Degradable Electronics, and Thermal Transfer Printing. *Adv Sci* **2019,** *6* (20), 1901478.

83.	Krisnadi, F.; Nguyen, L. L.; Ankit; Ma, J.; Kulkarni, M. R.; Mathews, N.; Dickey, M. D., Directed Assembly of Liquid Metal-Elastomer Conductors for Stretchable and Self-Healing Electronics. *Advanced materials* **2020,** *32* (30), e2001642.

84.	Xu, C.; Ma, B.; Yuan, S.; Zhao, C.; Liu, H., High‑Resolution Patterning of Liquid Metal on Hydrogel for Flexible, Stretchable, and Self‑Healing Electronics. *Advanced Electronic Materials* **2019,** *6* (1), 1900721.

85.	Mou, L.; Qi, J.; Tang, L.; Dong, R.; Xia, Y.; Gao, Y.; Jiang, X., Highly Stretchable and Biocompatible Liquid Metal-Elastomer Conductors for Self-Healing Electronics. *Small* **2020,** *16* (51), e2005336.

86.	Ito, R., Dodbiba, G., Fujita, T., MR fluid of liquid gallium dispersing magnetic particles. *International Journal of Modern Physics B* **2005,** *19(07n09)*, 1430-1436.

87.	Ma, K.-Q.; Liu, J., Nano liquid-metal fluid as ultimate coolant. *Physics Letters A* **2007,** *361* (3), 252-256.

88.	Tang, J.; Zhao, X.; Li, J.; Zhou, Y.; Liu, J., Liquid Metal Phagocytosis: Intermetallic Wetting Induced Particle Internalization. *Advanced science* **2017,** *4* (5),

1700024.

89.　Carle, F.; Bai, K.; Casara, J.; Vanderlick, K.; Brown, E., Development of magnetic liquid metal suspensions for magnetohydrodynamics. *Physical Review Fluids* **2017,** *2* (1).

90.　Blaiszik, B. J.; Kramer, S. L.; Grady, M. E.; McIlroy, D. A.; Moore, J. S.; Sottos, N. R.; White, S. R., Autonomic restoration of electrical conductivity. *Advanced materials* **2012,** *24* (3), 398-401.

91.　Mei, S.; Gao, Y.; Deng, Z.; Liu, J., Thermally Conductive and Highly Electrically Resistive Grease Through Homogeneously Dispersing Liquid Metal Droplets Inside Methyl Silicone Oil. *Journal of Electronic Packaging* **2014,** *136* (1).

92.　Fassler, A.; Majidi, C., Liquid-phase metal inclusions for a conductive polymer composite. *Advanced materials* **2015,** *27* (11), 1928-32.

93.　Kazem, N.; Bartlett, M. D.; Majidi, C., Extreme Toughening of Soft Materials with Liquid Metal. *Advanced materials* **2018,** *30* (22), e1706594.

94.　Tutika, R.; Zhou, S. H.; Napolitano, R. E.; Bartlett, M. D., Mechanical and Functional Tradeoffs in Multiphase Liquid Metal, Solid Particle Soft Composites. *Advanced Functional Materials* **2018,** *28* (45), 1804336.

95.　Chen, S.; Wang, H.-Z.; Zhao, R.-Q.; Rao, W.; Liu, J., Liquid Metal Composites. *Matter* **2020,** *2* (6), 1446-1480.

96.　Ren, L.; Zhuang, J.; Casillas, G.; Feng, H.; Liu, Y.; Xu, X.; Liu, Y.; Chen, J.; Du, Y.; Jiang, L.; Dou, S. X., Nanodroplets for Stretchable Superconducting Circuits. *Advanced Functional Materials* **2016,** *26* (44), 8111-8118.

97.　Yun, G.; Tang, S.-Y.; Zhao, Q.; Zhang, Y.; Lu, H.; Yuan, D.; Sun, S.; Deng, L.; Dickey, M. D.; Li, W., Liquid Metal Composites with Anisotropic and Unconventional Piezoconductivity. *Matter* **2020,** *3* (3), 824-841.

98.　Vallem, V.; Roosa, E.; Ledinh, T.; Jung, W.; Kim, T. i.; Rashid‑Nadimi, S.;

Kiani, A.; Dickey, M. D., A Soft Variable‑Area Electrical‑Double‑Layer Energy Harvester. *Advanced materials* **2021**, 2103142.

99.   Ambulo, C. P.; Ford, M. J.; Searles, K.; Majidi, C.; Ware, T. H., 4D-Printable Liquid Metal-Liquid Crystal Elastomer Composites. *ACS applied materials & interfaces* **2021,** *13* (11), 12805-12813.

100.   Kong, W.; Wang, Z.; Casey, N.; Korah, M. M.; Uppal, A.; Green, M. D.; Rykaczewski, K.; Wang, R. Y., High Thermal Conductivity in Multiphase Liquid Metal and Silicon Carbide Soft Composites. *Advanced Materials Interfaces* **2021,** *8* (14), 2100069.

101.   Pan, C.; Markvicka, E. J.; Malakooti, M. H.; Yan, J.; Hu, L.; Matyjaszewski, K.; Majidi, C., A Liquid-Metal-Elastomer Nanocomposite for Stretchable Dielectric Materials. *Advanced materials* **2019,** *31* (23), e1900663.

102.   Yan, J.; Malakooti, M. H.; Lu, Z.; Wang, Z.; Kazem, N.; Pan, C.; Bockstaller, M. R.; Majidi, C.; Matyjaszewski, K., Solution processable liquid metal nanodroplets by surface-initiated atom transfer radical polymerization. *Nature nanotechnology* **2019,** *14* (7), 684-690.

103.   Chang, B. S.; Thomas, B.; Chen, J.; Tevis, I. D.; Karanja, P.; Cinar, S.; Venkatesh, A.; Rossini, A. J.; Thuo, M. M., Ambient synthesis of nanomaterials by in situ heterogeneous metal/ligand reactions. *Nanoscale* **2019,** *11* (29), 14060-14069.

104.   Liu, Y.; Wang, Q.; Deng, J.; Zhang, W., A liquid metal composite by ZIF-8 encapsulation. *Chemical communications* **2020,** *56* (12), 1851-1854.

105.   Tang, S.-Y.; Qiao, R.; Lin, Y.; Li, Y.; Zhao, Q.; Yuan, D.; Yun, G.; Guo, J.; Dickey, M. D.; Huang, T. J.; Davis, T. P.; Kalantar-Zadeh, K.; Li, W., Functional Liquid Metal Nanoparticles Produced by Liquid-Based Nebulization. *Advanced Materials Technologies* **2018**, 1800420.

106.   Centurion, F.; Saborio, M. G.; Allioux, F. M.; Cai, S.; Ghasemian, M. B.; Kalantar-Zadeh, K.; Rahim, M. A., Liquid metal dispersion by self-assembly of natural phenolics. *Chemical communications* **2019,** *55* (75), 11291-11294.

107.   Yan, J.; Zhang, X.; Liu, Y.; Ye, Y.; Yu, J.; Chen, Q.; Wang, J.; Zhang, Y.; Hu, Q.; Kang, Y.; Yang, M.; Gu, Z., Shape-controlled synthesis of liquid metal nanodroplets for photothermal therapy. *Nano Research* **2019,** *12* (6), 1313-1320.

108.   Chen, Y.; Liu, Z.; Zhu, D.; Handschuh-Wang, S.; Liang, S.; Yang, J.; Kong, T.; Zhou, X.; Liu, Y.; Zhou, X., Liquid metal droplets with high elasticity, mobility and mechanical robustness. *Materials Horizons* **2017,** *4* (4), 591-597.

109.   Zhang, W.; Naidu, B. S.; Ou, J. Z.; O'Mullane, A. P.; Chrimes, A. F.; Carey, B. J.; Wang, Y.; Tang, S. Y.; Sivan, V.; Mitchell, A.; Bhargava, S. K.; Kalantar-Zadeh, K., Liquid metal/metal oxide frameworks with incorporated Ga2O3 for photocatalysis. *ACS applied materials & interfaces* **2015,** *7* (3), 1943-8.

110.   Tang, X., Tang, S. Y., Sivan, V., Zhang, W., Mitchell, A., Kalantar-zadeh, K., Khoshmanesh, K., Photochemically induced motion of liquid metal marbles. *Applied Physics Letters* **2013,** *103(17)*, 174104.

111.   Zhao, Y.; Fang, J.; Wang, H.; Wang, X.; Lin, T., Magnetic liquid marbles: manipulation of liquid droplets using highly hydrophobic Fe3O4 nanoparticles. *Advanced materials* **2010,** *22* (6), 707-10.

112.   Kim, D.; Lee, J.-B., Magnetic-field-induced liquid metal droplet manipulation. *Journal of the Korean Physical Society* **2015,** *66* (2), 282-286.

113.   Tang, J.; Zhao, X.; Li, J.; Guo, R.; Zhou, Y.; Liu, J., Gallium-Based Liquid Metal Amalgams: Transitional-State Metallic Mixtures (TransM(2)ixes) with Enhanced and Tunable Electrical, Thermal, and Mechanical Properties. *ACS applied materials & interfaces* **2017,** *9* (41), 35977-35987.

114. Chang, H.; Guo, R.; Sun, Z.; Wang, H.; Hou, Y.; Wang, Q.; Rao, W.; Liu, J., Direct Writing and Repairable Paper Flexible Electronics Using Nickel-Liquid Metal Ink. *Advanced Materials Interfaces* **2018,** *5* (20), 1800571.

115. Guo, R.; Wang, X.; Chang, H.; Yu, W.; Liang, S.; Rao, W.; Liu, J., Ni-GaIn Amalgams Enabled Rapid and Customizable Fabrication of Wearable and Wireless Healthcare Electronics. *Advanced Engineering Materials* **2018,** *20* (10), 1800054.

116. Guo, R.; Sun, X.; Yao, S.; Duan, M.; Wang, H.; Liu, J.; Deng, Z., Semi‐Liquid‐Metal‐(Ni‐EGaIn)‐Based Ultraconformable Electronic Tattoo. *Advanced Materials Technologies* **2019,** *4* (8), 1900183.

117. I, A. d. C.; Chrimes, A. F.; Zavabeti, A.; Berean, K. J.; Carey, B. J.; Zhuang, J.; Du, Y.; Dou, S. X.; Suzuki, K.; Shanks, R. A.; Nixon-Luke, R.; Bryant, G.; Khoshmanesh, K.; Kalantar-Zadeh, K.; Daeneke, T., A Gallium-Based Magnetocaloric Liquid Metal Ferrofluid. *Nano letters* **2017,** *17* (12), 7831-7838.

118. Ren, L.; Sun, S.; Casillas-Garcia, G.; Nancarrow, M.; Peleckis, G.; Turdy, M.; Du, K.; Xu, X.; Li, W.; Jiang, L.; Dou, S. X.; Du, Y., A Liquid-Metal-Based Magnetoactive Slurry for Stimuli-Responsive Mechanically Adaptive Electrodes. *Advanced materials* **2018,** *30* (35), e1802595.

119. Zhang, J.; Yao, Y.; Sheng, L.; Liu, J., Self-fueled biomimetic liquid metal mollusk. *Advanced materials* **2015,** *27* (16), 2648-55.

120. Kong, W.; Wang, Z.; Wang, M.; Manning, K. C.; Uppal, A.; Green, M. D.; Wang, R. Y.; Rykaczewski, K., Oxide-Mediated Formation of Chemically Stable Tungsten-Liquid Metal Mixtures for Enhanced Thermal Interfaces. *Advanced materials* **2019,** *31* (44), e1904309.

121. Chen, S.; Yang, X.; Wang, H.; Wang, R.; Liu, J., Al-assisted high frequency self-powered oscillations of liquid metal droplets. *Soft matter* **2019,** *15* (44), 8971-8975.

122.   Yuan, B.; Tan, S.; Zhou, Y.; Liu, J., Self-powered macroscopic Brownian motion of spontaneously running liquid metal motors. *Science Bulletin* **2015,** *60* (13), 1203-1210.

123.   Xiong, M.; Gao, Y.; Liu, J., Fabrication of magnetic nano liquid metal fluid through loading of Ni nanoparticles into gallium or its alloy. *Journal of Magnetism and Magnetic Materials* **2014,** *354*, 279-283.

124.   Zhang, J.; Guo, R.; Liu, J., Self-propelled liquid metal motors steered by a magnetic or electrical field for drug delivery. *Journal of Materials Chemistry B* **2016,** *4* (32), 5349-5357.

125.   Gao, Y.; Liu, J., Gallium-based thermal interface material with high compliance and wettability. *Applied Physics A* **2012,** *107* (3), 701-708.

126.   Kim, M. G.; Brown, D. K.; Brand, O., Nanofabrication for all-soft and high-density electronic devices based on liquid metal. *Nature communications* **2020,** *11* (1), 1002.

127.   Tang, J.; Lambie, S.; Meftahi, N.; Christofferson, A. J.; Yang, J.; Ghasemian, M. B.; Han, J.; Allioux, F. M.; Rahim, M. A.; Mayyas, M.; Daeneke, T.; McConville, C. F.; Steenbergen, K. G.; Kaner, R. B.; Russo, S. P.; Gaston, N.; Kalantar-Zadeh, K., Unique surface patterns emerging during solidification of liquid metal alloys. *Nature nanotechnology* **2021,** *16* (4), 431-439.

128.   Esrafilzadeh, D.; Zavabeti, A.; Jalili, R.; Atkin, P.; Choi, J.; Carey, B. J.; Brkljača, R.; O'Mullane, A. P.; Dickey, M. D.; Officer, D. L.; MacFarlane, D. R.; Daeneke, T.; Kalantar-Zadeh, K., Room temperature CO2 reduction to solid carbon species on liquid metals featuring atomically thin ceria interfaces. *Nature communications* **2019,** *10* (1).

129.   Zuraiqi, K.; Zavabeti, A.; Allioux, F.-M.; Tang, J.; Nguyen, C. K.; Tafazolymotie, P.; Mayyas, M.; Ramarao, A. V.; Spencer, M.; Shah, K.; McConville, C. F.; Kalantar-Zadeh, K.; Chiang, K.; Daeneke, T., Liquid Metals in Catalysis for Energy Applications.

Joule **2020,** *4* (11), 2290-2321.

130. Krishnamurthi, V.; Khan, H.; Ahmed, T.; Zavabeti, A.; Tawfik, S. A.; Jain, S. K.; Spencer, M. J. S.; Balendhran, S.; Crozier, K. B.; Li, Z.; Fu, L.; Mohiuddin, M.; Low, M. X.; Shabbir, B.; Boes, A.; Mitchell, A.; McConville, C. F.; Li, Y.; Kalantar-Zadeh, K.; Mahmood, N.; Walia, S., Liquid-Metal Synthesized Ultrathin SnS Layers for High-Performance Broadband Photodetectors. *Advanced materials* **2020,** *32* (45), e2004247.

131. Lide, D. R., internet version 2005., *CRC handbook of chemistry and physics*. Boca Raton, FL, 2005.

132. Robie, R. A., Hemingway, B. S., Fisher, J. R. , *Geological Survey Bulletin1452*. United States Government, Printing Office, Washington., 1978.

133. Mohammad B. Ghasemian, A. Z., Roozbeh Abbasi, Priyank V. Kumar, Nitu Syed, Yin Yao, Jianbo Tang, Yifang Wang, Aaron Elbourne, Jialuo Han, Maedehsadat Mousavi, Torben Daeneke, Kourosh Kalantar-Zadeh, Ultra-thin lead oxide piezoelectric layers for reduced environmental contamination using a liquid metal-based process. *Journal of Materials Chemistry A* **2020,** *8(37)*, 19434-19443.

134. Ghasemian, M. B.; Mayyas, M.; Idrus‑Saidi, S. A.; Jamal, M. A.; Yang, J.; Mofarah, S. S.; Adabifiroozjaei, E.; Tang, J.; Syed, N.; O'Mullane, A. P.; Daeneke, T.; Kalantar‑Zadeh, K., Self‑Limiting Galvanic Growth of MnO2 Monolayers on a Liquid Metal—Applied to Photocatalysis. *Advanced Functional Materials* **2019,** *29* (36), 1901649.

135. Ren, L.; Cheng, N.; Man, X.; Qi, D.; Liu, Y.; Xu, G.; Cui, D.; Liu, N.; Zhong, J.; Peleckis, G.; Xu, X.; Dou, S. X.; Du, Y., General Programmable Growth of Hybrid Core-Shell Nanostructures with Liquid Metal Nanodroplets. *Advanced materials* **2021,** *33* (11), e2008024.

136. Wang, Y.; Mayyas, M.; Yang, J.; Tang, J.; Ghasemian, M. B.; Han, J.; Elbourne,

A.; Daeneke, T.; Kaner, R. B.; Kalantar‑Zadeh, K., Self‑Deposition of 2D Molybdenum Sulfides on Liquid Metals. *Advanced Functional Materials* **2020,** *31* (3), 2005866.

137.   Li, H.; Abbasi, R.; Wang, Y.; Allioux, F. M.; Koshy, P.; Idrus-Saidi, S. A.; Rahim, M. A.; Yang, J.; Mousavi, M.; Tang, J.; Ghasemian, M. B.; Jalili, R.; Kalantar-Zadeh, K.; Mayyas, M., Liquid metal-supported synthesis of cupric oxide. *Journal of Materials Chemistry C* **2020,** *8* (5), 1656-1665.

138.   Mousavi, M.; Ghasemian, M. B.; Han, J.; Wang, Y.; Abbasi, R.; Yang, J.; Tang, J.; Idrus-Saidi, S. A.; Guan, X.; Christoe, M. J.; Merhebi, S.; Zhang, C.; Tang, J.; Jalili, R.; Daeneke, T.; Wu, T.; Kalantar-Zadeh, K.; Mayyas, M., Bismuth telluride topological insulator synthesized using liquid metal alloys: Test of NO2 selective sensing. *Applied Materials Today* **2021,** *22*, 100954.

139.   Khan, H.; Mahmood, N.; Zavabeti, A.; Elbourne, A.; Rahman, M. A.; Zhang, B. Y.; Krishnamurthi, V.; Atkin, P.; Ghasemian, M. B.; Yang, J.; Zheng, G.; Ravindran, A. R.; Walia, S.; Wang, L.; Russo, S. P.; Daeneke, T.; Li, Y.; Kalantar-Zadeh, K., Liquid metal-based synthesis of high performance monolayer SnS piezoelectric nanogenerators. *Nature communications* **2020,** *11* (1).

140.   Alsaif, M. M. Y. A.; Pillai, N.; Kuriakose, S.; Walia, S.; Jannat, A.; Xu, K.; Alkathiri, T.; Mohiuddin, M.; Daeneke, T.; Kalantar-Zadeh, K.; Ou, J. Z.; Zavabeti, A., Atomically Thin Ga2S3 from Skin of Liquid Metals for Electrical, Optical, and Sensing Applications. *ACS Applied Nano Materials* **2019,** *2* (7), 4665-4672.

141.   Syed, N.; Zavabeti, A.; Ou, J. Z.; Mohiuddin, M.; Pillai, N.; Carey, B. J.; Zhang, B. Y.; Datta, R. S.; Jannat, A.; Haque, F.; Messalea, K. A.; Xu, C.; Russo, S. P.; McConville, C. F.; Daeneke, T.; Kalantar-Zadeh, K., Printing two-dimensional gallium phosphate out of liquid metal. *Nature communications* **2018,** *9* (1), 3618.

142.   Zavabeti, A.; Zhang, B. Y.; de Castro, I. A.; Ou, J. Z.; Carey, B. J.; Mohiuddin, M.; Datta, R.; Xu, C.; Mouritz, A. P.; McConville, C. F.; O'Mullane, A. P.; Daeneke, T.; Kalantar-Zadeh, K., Green Synthesis of Low-Dimensional Aluminum Oxide Hydroxide and Oxide Using Liquid Metal Reaction Media: Ultrahigh Flux Membranes. *Advanced Functional Materials* **2018,** *28* (44), 1804057.

143.   Cutinho, J.; Chang, B. S.; Oyola-Reynoso, S.; Chen, J.; Akhter, S. S.; Tevis, I. D.; Bello, N. J.; Martin, A.; Foster, M. C.; Thuo, M. M., Autonomous Thermal-Oxidative Composition Inversion and Texture Tuning of Liquid Metal Surfaces. *ACS nano* **2018,** *12* (5), 4744-4753.

144.   Allioux, F. M.; Merhebi, S.; Ghasemian, M. B.; Tang, J.; Merenda, A.; Abbasi, R.; Mayyas, M.; Daeneke, T.; O'Mullane, A. P.; Daiyan, R.; Amal, R.; Kalantar-Zadeh, K., Bi-Sn Catalytic Foam Governed by Nanometallurgy of Liquid Metals. *Nano letters* **2020,** *20* (6), 4403-4409.

145.   Jeon, J.; Lee, J. B.; Chung, S. K.; Kim, D., On-demand magnetic manipulation of liquid metal in microfluidic channels for electrical switching applications. *Lab on a chip* **2016,** *17* (1), 128-133.

146.   Li, F.; Kuang, S.; Li, X.; Shu, J.; Li, W.; Tang, S.-Y.; Zhang, S., Magnetically- and Electrically-Controllable Functional Liquid Metal Droplets. *Advanced Materials Technologies* **2019,** *4* (3), 1800694.

147.   Hu, L.; Wang, H.; Wang, X.; Liu, X.; Guo, J.; Liu, J., Magnetic Liquid Metals Manipulated in the Three-Dimensional Free Space. *ACS applied materials & interfaces* **2019,** *11* (8), 8685-8692.

148.   Liu, H.; Li, M.; Li, Y.; Yang, H.; Li, A.; Lu, T. J.; Li, F.; Xu, F., Magnetic steering of liquid metal mobiles. *Soft matter* **2018,** *14* (17), 3236-3245.

149.   Cao, L.; Yu, D.; Xia, Z.; Wan, H.; Liu, C.; Yin, T.; He, Z., Ferromagnetic Liquid

Metal Putty-Like Material with Transformed Shape and Reconfigurable Polarity. *Advanced materials* **2020,** *32* (17), e2000827.

150.   Merhebi, S.; Mayyas, M.; Abbasi, R.; Christoe, M. J.; Han, J.; Tang, J.; Rahim, M. A.; Yang, J.; Tan, T. T.; Chu, D.; Zhang, J.; Li, S.; Wang, C. H.; Kalantar-Zadeh, K.; Allioux, F. M., Magnetic and Conductive Liquid Metal Gels. *ACS applied materials & interfaces* **2020,** *12* (17), 20119-20128.

151.   Brown, P. L., Ekberg, C.   , *Hydrolysis of metal ions*. John Wiley & Sons: 2016.

152.   Shi-Yang Tanga, K. K., Vijay Sivan, Phred Petersen, Anthony P. O'Mullane, Derek Abbott, Arnan Mitchell, Kourosh Kalantar-zadeh, Liquid metal enabled pump. *Proceedings of the National Academy of Sciences* **2014,** *111(9)*, 3304-3309.

153.   Sheng, L.; Zhang, J.; Liu, J., Diverse transformations of liquid metals between different morphologies. *Advanced materials* **2014,** *26* (34), 6036-42.

154.   Zavabeti, A.; Daeneke, T.; Chrimes, A. F.; O'Mullane, A. P.; Zhen Ou, J.; Mitchell, A.; Khoshmanesh, K.; Kalantar-Zadeh, K., Ionic imbalance induced self-propulsion of liquid metals. *Nature communications* **2016,** *7*, 12402.

155.   Hu, L.; Li, J.; Tang, J.; Liu, J., Surface effects of liquid metal amoeba. *Science Bulletin* **2017,** *62* (10), 700-706.

156.   Wang, L.; Liu, J., Graphite induced periodical self-actuation of liquid metal. *RSC Advances* **2016,** *6* (65), 60729-60735.

157.   Yao, Y.-y.; Liu, J., A polarized liquid metal worm squeezing across a localized irregular gap. *RSC Advances* **2017,** *7* (18), 11049-11056.

158.   Wu, J.; Tang, S. Y.; Fang, T.; Li, W.; Li, X.; Zhang, S., A Wheeled Robot Driven by a Liquid-Metal Droplet. *Advanced materials* **2018**, e1805039.

159.   Sheng, L.; He, Z.; Yao, Y.; Liu, J., Transient State Machine Enabled from the Colliding and Coalescence of a Swarm of Autonomously Running Liquid Metal Motors.

Small **2015,** *11* (39), 5253-61.

160. Mohammed, M.; Sundaresan, R.; Dickey, M. D., Self-Running Liquid Metal Drops that Delaminate Metal Films at Record Velocities. *ACS applied materials & interfaces* **2015,** *7* (41), 23163-71.

161. Yuan, B.; Wang, L.; Yang, X.; Ding, Y.; Tan, S.; Yi, L.; He, Z.; Liu, J., Liquid Metal Machine Triggered Violin-Like Wire Oscillator. *Advanced science* **2016,** *3* (10), 1600212.

162. Ma, J.-L.; Dong, H.-X.; He, Z.-Z., Electrochemically enabled manipulation of gallium-based liquid metals within porous copper. *Materials Horizons* **2018,** *5* (4), 675-682.

163. Eaker, C. B.; Hight, D. C.; O'Regan, J. D.; Dickey, M. D.; Daniels, K. E., Oxidation-Mediated Fingering in Liquid Metals. *Phys Rev Lett* **2017,** *119* (17), 174502.

164. Yu, Z. W.; Chen, Y. C.; Yun, F. F.; Wang, X. L., Simultaneous Fast Deformation and Solidification in Supercooled Liquid Gallium at Room Temperature *Advanced Engineering Materials* **2017,** *19* (8), 1700190.

165. Yu, Z.; Yun, F. F.; Wang, X., A novel liquid metal patterning technique: voltage induced non-contact electrochemical lithography at room temperature. *Materials Horizons* **2018,** *5* (1), 36-40.

166. Yu, Z.; Chen, Y.; Yun, F. F.; Cortie, D.; Jiang, L.; Wang, X., Discovery of a Voltage-Stimulated Heartbeat Effect in Droplets of Liquid Gallium. *Phys Rev Lett* **2018,** *121* (2), 024302.

167. Wissman, J.; Dickey, M. D.; Majidi, C., Field-Controlled Electrical Switch with Liquid Metal. *Advanced science* **2017,** *4* (12), 1700169.

168. Lohöfer, G., High-resolution inductive measurement of electrical resistivity and density of electromagnetically levitated liquid metal droplets. *Review of Scientific*

Instruments **2018,** *89(12)*, 124709.

169.   Fisher, A. E., Kolemen, E., Hvasta, M. G., Experimental demonstration of hydraulic jump control in liquid metal channel flow using Lorentz force. *Physics of Fluids* **2018,** *30(6)*, 067104.

170.   Shu, J.; Tang, S. Y.; Feng, Z.; Li, W.; Li, X.; Zhang, S., Unconventional locomotion of liquid metal droplets driven by magnetic fields. *Soft matter* **2018,** *14* (35), 7113-7118.

171.   Zhao, X., Yang, L., Ding, Y., Zhang, P., Liu, J., Noncoalescent liquid metal droplets sustained on a magnetic field-circulated liquid metal bath surface. *Applied Physics Letters* **2019,** *115(8)*, 083702.

172.   Tan, S. C., Gui, H., Yuan, B., Liu, J., Magnetic trap effect to restrict motion of self-powered tiny liquid metal motors. *Applied Physics Letters* **2015,** *107(7)*, 071904.

173.   Wang, L.; Liu, J., Liquid metal folding patterns induced by electric capillary force. *Applied Physics Letters* **2016,** *108* (16), 161602.

174.   Moon, F. C., *Superconducting levitation: applications to bearings and magnetic transportation*. John Wiley & Sons: 2008.

175.   Wang, X., Ho, C., Tsatskis, Y., Law, J., Zhang, Z., Zhu, M., ... & Sun, Y., Intracellular manipulation and measurement with multipole magnetic tweezers. *Science robotics* **2019,** *4* (28).

176.   Tian, Z., Yang, S., Huang, P. H., Wang, Z., Zhang, P., Gu, Y., ... & Huang, T. J. , Wave number-spiral acoustic tweezers for dynamic and reconfigurable manipulation of particles and cells. *Science advances* **2019,** *5* (5).

177.   Ahmed, D.; Ozcelik, A.; Bojanala, N.; Nama, N.; Upadhyay, A.; Chen, Y.; Hanna-Rose, W.; Huang, T. J., Rotational manipulation of single cells and organisms using acoustic waves. *Nature communications* **2016,** *7*, 11085.

178.   Ashkin, A., Dziedzic, J. M., Bjorkholm, J. E., & Chu, S. (1986). Observation of a single-beam gradient force optical trap for dielectric particles. *Optics letters* **1986,** *11* (5), 288-290.

179.   Brandt, E. H., Levitation in physics. *Science* **1989,** *243* (4889), 349-355.

180.   Zhang, J.; Wang, Z.; Wang, Z.; Zhang, T.; Wei, L., In-fibre particle manipulation and device assembly via laser induced thermocapillary convection. *Nature communications* **2019,** *10* (1), 5206.

181.   Yun, F. F.; Yu, Z.; He, Y.; Jiang, L.; Wang, Z.; Gu, H.; Wang, X., Voltage-induced penetration effect in liquid metals at room temperature. *National science review* **2020,** *7* (2), 366-372.

182.   Tang, J.; Zhao, X.; Li, J.; Liu, J., Thin, Porous, and Conductive Networks of Metal Nanoparticles through Electrochemical Welding on a Liquid Metal Template. *Advanced Materials Interfaces* **2018,** *5* (19), 1800406.

183.   Yahua He, J. T., Kourosh Kalantar-Zadeh, Michael D. Dickey, and Xiaolin Wang, Noncontact rotation, levitation, and acceleration of flowing liquid metal wires. *Proceedings of the National Academy of Sciences* **2022,** *119 (6).*

184.   Johnston, L.; Yang, J.; Han, J.; Kalantar-Zadeh, K.; Tang, J., Intermetallic wetting enabled high resolution liquid metal patterning for 3D and flexible electronics. *Journal of Materials Chemistry C* **2022,** *10* (3), 921-931.

185.   Favaro, M.; Jeong, B.; Ross, P. N.; Yano, J.; Hussain, Z.; Liu, Z.; Crumlin, E. J., Unravelling the electrochemical double layer by direct probing of the solid/liquid interface. *Nature communications* **2016,** *7*, 12695.

186.   Khademi, M.; Barz, D. P. J., Structure of the Electrical Double Layer Revisited: Electrode Capacitance in Aqueous Solutions. *Langmuir : the ACS journal of surfaces and colloids* **2020,** *36* (16), 4250-4260.

187.   J.Q. Shang, K. Y. L., and R.M. Quigley, Quantitative determination of potential distribution in Stern–Gouy double-layer model. *Canadian Geotechnical Journal* **1994,** *31(5)*, 624-636.

188.   Troian, S. M.; Wu, X. L.; Safran, S. A., Fingering instability in thin wetting films. *Phys Rev Lett* **1989,** *62* (13), 1496-1499.

189.   Mayyas, M.; Li, H.; Kumar, P.; Ghasemian, M. B.; Yang, J.; Wang, Y.; Lawes, D. J.; Han, J.; Saborio, M. G.; Tang, J.; Jalili, R.; Lee, S. H.; Seong, W. K.; Russo, S. P.; Esrafilzadeh, D.; Daeneke, T.; Kaner, R. B.; Ruoff, R. S.; Kalantar-Zadeh, K., Liquid-Metal-Templated Synthesis of 2D Graphitic Materials at Room Temperature. *Advanced materials* **2020,** *32* (29), e2001997.

190.   Allagui, A.; Benaoum, H.; Olendski, O., On the Gouy–Chapman–Stern model of the electrical double-layer structure with a generalized Boltzmann factor. *Physica A: Statistical Mechanics and its Applications* **2021,** *582*, 126252.

191.   Kant, R.; Singh, M. B., Generalization of the Gouy-Chapman-Stern model of an electric double layer for a morphologically complex electrode: deterministic and stochastic morphologies. *Physical review. E, Statistical, nonlinear, and soft matter physics* **2013,** *88* (5), 052303.

192.   M. Abercrombie, a. J. E. H., Observations on the social behaviour of cells in tissue culture: II."Monolayering" of fibroblasts. *Experimental cell research* **1954,** *6(2)*, 293-306.

193.   M. Abercrombie, a. E. J. A., Interference microscope studies of cell contacts in tissue culture. *Experimental cell research* **1958,** *15(2)*, 332-345.

194.   Linke, H.; Aleman, B. J.; Melling, L. D.; Taormina, M. J.; Francis, M. J.; Dow-Hygelund, C. C.; Narayanan, V.; Taylor, R. P.; Stout, A., Self-propelled Leidenfrost droplets. *Phys Rev Lett* **2006,** *96* (15), 154502.

195.   Pan, Z.; Huang, J.; Tong, Y.; Zheng, C.; Bao, H., Interactive localized liquid motion editing. *ACM Transactions on Graphics* **2013,** *32* (6), 1-10.

196.   Lee, S. J.; Kim, M. H., The Effects of Inner-Liquid Motion on LNG Vessel Responses. *Journal of Offshore Mechanics and Arctic Engineering* **2010,** *132* (2).

197.   Li, Y.; He, L.; Zhang, X.; Zhang, N.; Tian, D., External-Field-Induced Gradient Wetting for Controllable Liquid Transport: From Movement on the Surface to Penetration into the Surface. *Advanced materials* **2017,** *29* (45).

198.   Paradisanos, I., Fotakis, C., Anastasiadis, S. H., & Stratakis, E., Gradient induced liquid motion on laser structured black Si surfaces. *Applied Physics Letters* **2015,** *107* (11).

199.   Langelier, S. M.; Chang, D. S.; Zeitoun, R. I.; Burns, M. A., Acoustically driven programmable liquid motion using resonance cavities. *Proceedings of the National Academy of Sciences of the United States of America* **2009,** *106* (31), 12617-22.

200.   Luo, M.; Gupta, R.; Frechette, J., Modulating contact angle hysteresis to direct fluid droplets along a homogenous surface. *ACS applied materials & interfaces* **2012,** *4* (2), 890-6.

201.   Tuček, J., Beránek, P., Vobecká, L., Slouka, Z., & Přibyl, M., Electric field driven addressing of oil-in-water droplets in the presence of gradients of ionic and nonionic surfactants. *IEEE Transactions on Industry Applications* **2016,** *52* (5), 4337-4344.

202.   Drotlef, D. M.; Blumler, P.; Papadopoulos, P.; Del Campo, A., Magnetically actuated micropatterns for switchable wettability. *ACS applied materials & interfaces* **2014,** *6* (11), 8702-7.

203.   Zhu, Y.; Antao, D. S.; Xiao, R.; Wang, E. N., Real-time manipulation with magnetically tunable structures. *Advanced materials* **2014,** *26* (37), 6442-6.

204.   Lee, S.; Yim, C.; Kim, W.; Jeon, S., Magnetorheological Elastomer Films with

Tunable Wetting and Adhesion Properties. *ACS applied materials & interfaces* **2015,** *7* (35), 19853-6.

205.   Oh, S.-K.; Nakagawa, M.; Ichimura, K., Photocontrol of liquid motion on an azobenzene monolayer. *Journal of Materials Chemistry* **2002,** *12* (8), 2262-2269.

206.   Yang, D., Piech, M., Bell, N. S., Gust, D., Vail, S., Garcia, A. A., ... & Picraux, S. T., Photon control of liquid motion on reversibly photoresponsive surfaces. *Langmuir : the ACS journal of surfaces and colloids* **2007,** *23* (21), 10864-10872.

207.   Lv, J. A.; Liu, Y.; Wei, J.; Chen, E.; Qin, L.; Yu, Y., Photocontrol of fluid slugs in liquid crystal polymer microactuators. *Nature* **2016,** *537* (7619), 179-84.

208.   Liu, M.; Nie, F. Q.; Wei, Z.; Song, Y.; Jiang, L., In situ electrochemical switching of wetting state of oil droplet on conducting polymer films. *Langmuir : the ACS journal of surfaces and colloids* **2010,** *26* (6), 3993-7.

209.   Sumino, Y.; Magome, N.; Hamada, T.; Yoshikawa, K., Self-running droplet: emergence of regular motion from nonequilibrium noise. *Phys Rev Lett* **2005,** *94* (6), 068301.

210.   Daniel, S., Chaudhury, M. K., & Chen, J. C. , Fast drop movements resulting from the phase change on a gradient surface. *Science* **2001,** *291* (5504), 633-636.

211.   Bartlett, M. D.; Kazem, N.; Powell-Palm, M. J.; Huang, X.; Sun, W.; Malen, J. A.; Majidi, C., High thermal conductivity in soft elastomers with elongated liquid metal inclusions. *Proceedings of the National Academy of Sciences of the United States of America* **2017,** *114* (9), 2143-2148.

212.   Xin, Y.; Peng, H.; Xu, J.; Zhang, J., Ultrauniform Embedded Liquid Metal in Sulfur Polymers for Recyclable, Conductive, and Self‑Healable Materials. *Advanced Functional Materials* **2019,** *29* (17), 1808989.

213.   Shu, J.; Ge, D. A.; Wang, E.; Ren, H.; Cole, T.; Tang, S. Y.; Li, X.; Zhou, X.; Li,

R.; Jin, H.; Li, W.; Dickey, M. D.; Zhang, S., A Liquid Metal Artificial Muscle. *Advanced materials* **2021,** *33* (43), e2103062.

214.   Lu, Y.; Hu, Q.; Lin, Y.; Pacardo, D. B.; Wang, C.; Sun, W.; Ligler, F. S.; Dickey, M. D.; Gu, Z., Transformable liquid-metal nanomedicine. *Nature communications* **2015,** *6*, 10066.

Appendices

Appendix 1

1.   Publications

First/co-first author papers

1. **He, Y.,** Tang, J, … & Wang, X. (2022). Noncontact rotation, levitation, and acceleration of flowing liquid metal wires. *Proceedings of the National Academy of Sciences*, *119*(6), e2117535119.

2. You, J., **He, Y.,** … & Wang, X. (2021). High-Electrification Performance and Mechanism of a Water–Solid Mode Triboelectric Nanogenerator. *ACS nano*, *15*(5), 8706-8714.

3. Yun, F. F., **He, Y.,** … & Wang, X. (2020). Voltage-induced penetration effect in liquid metals at room temperature. *National science review*, *7*(2), 366-372.

Other papers

4. Jiang, L., …**He, Y**., ... & Wang, J. (2021). Ultrahigh piezoelectric coefficients of Li-doped (K, Na) NbO_3 nanorod arrays with manipulated OT phase boundary: Towards energy harvesting and self-powered human movement monitoring. *Nano Energy*, *86*, 106072.

5. Afzal, W., …**He, Y.,** ... & Wang, X. (2021). Magneto-transport and electronic structures in MoSi2 bulks and thin films with different orientations. *Journal of Alloys and Compounds*, *858*, 157670.

6. Li, L., … **He, Y.,** ... & Gao, Y. (2020). Atomic scale study of the oxygen annealing effect on piezoelectricity enhancement of (K, Na) NbO_3 nanorods. *Journal of Materials Chemistry C*, *8*(44), 15830-15838.

7. Jin, W., … **He, Y.,** ... & Wang, X. (2018). Evolution of the composition, structure,

and piezoelectric performance of (K1-xNax) NbO3 nanorod arrays with hydrothermal reaction time. *Applied Physics Letters*, *112*(14), 142904.

8. Jin, W., … **He, Y**., ... & Gu, H. (2018). High-performance piezoelectric energy harvesting of vertically aligned Pb (Zr, Ti) O$_3$ nanorod arrays. *RSC advances*, *8*(14), 7422-7427.

9. Wang, Z., … **He, Y.**, ... & Gu, H. (2017). Self-powered viscosity and pressure sensing in microfluidic systems based on the piezoelectric energy harvesting of flowing droplets. *ACS applied materials & interfaces*, *9*(34), 28586-28595.